Molecule diffusion in bacteria and consequences of osmotic stress

Mika, Jacek Tadeusz

Publication date:
2012

Citation for published version (APA):
Mika, J. T. (2012). Molecule diffusion in bacteria and consequences of osmotic stress. Groningen: s.n.

MOLECULE DIFFUSION IN BACTERIA AND CONSEQUENCES OF OSMOTIC STRESS

Jacek T. Mika

Cover: An *Escherichia coli* cell experiencing osmotic shock. An image of a cell expressing GFP acquired with a conventional fluorescence microscope. The image is false-colored using ImageJ.

Lay-out by: M.F. Masman

Printed by: Ipskamp drukkers.

ISBN: 978-90-367-5293-0 (printed version)
978-90-367-5294-7 (electronic version)

The research described in this thesis was carried out in the Biochemistry Department of the Groningen Biomolecular Sciences and Biotechnology Institute (GBB) of the University of Groningen, the Netherlands and was financially supported by SysMo via the BBSRC-funded KosmoBac programme, the NWO (Top-subsidy Grant 700.56.302) and the Zernike Institute of Advanced Materials.

rijksuniversiteit
groningen

MOLECULE DIFFUSION IN BACTERIA AND CONSEQUENCES OF OSMOTIC STRESS

Proefschrift

ter verkrijging van het doctoraat in de
Wiskunde en Natuurwetenschappen
aan de Rijksuniversiteit Groningen
op gezag van de
Rector Magnificus, dr. E. Sterken,
in het openbaar te verdedigen op
vrijdag 6 januari 2012
om 12:45 uur

door

Jacek Tadeusz Mika

geboren op 16 december 1983
te Wroclaw, Polen

Promotor:	Prof. dr. B. Poolman
Copromotor:	Dr. V.V. Krasnikov
Beoordelingscommissie:	Prof. dr. I.R. Booth Prof. dr. S.J. Marrink Prof. dr. A.J.M. van Oijen

ISBN: 978-90-367-5293-0

Mojej rodzinie

Contents

CHAPTER 1

INTRODUCTION

Jacek T. Mika

Consequences of osmotic stress

Escherichia coli

Escherichia coli is a rod-shaped, Gram-negative bacterium (Fig. 1), whose natural environment is the intestine of warm-blooded organisms. In the case of humans, *E.coli* and related bacteria (Proteobacteria) can make up to 0.1 % of normal, healthy gut flora (Eckburg *et al.*, 2005), where they can benefit the host by producing vitamin K_2 and by preventing the growth of pathogenic bacteria. There are also *E.coli* pathogenic strains that cause syndromes ranging from diarrhea through infections of the gastro-intestinal and urinary tracts, and, in the most severe cases, death. Since its discovery in 1885 by Theodor Escherich, *E.coli* has received a lot of attention from the scientific community and is now a widely accepted model of a (bacterial) cell. Especially molecular biology relies strongly on this cheaply and easily cultivatable bacterium, for DNA manipulation techniques and (heterologous) protein overexpression.

E.coli has an outer membrane, a thin peptidoglycan layer (the actual cell wall) and an inner membrane (plasma membrane, Fig. 1,2). The cell interior is typical for bacterial cells, i.e. there are no bounded organelles that separate their contents from the bulk of the cytoplasm. A significant portion of the cytoplasm is occupied by the nucleoid – the cell’s chromosome (Fig. 2). Some researchers also distinguish cell poles, as a distinct region of the cell with characteristics different from the bulk of the cytoplasm (Vendeville *et al.*, 2011). *E. coli* cells inhabiting either their native (e.g. the gut) or foreign environments (e.g. soil, water) can be exposed to a number of physicochemical changes. These include such parameters as temperature, pH and osmolality. In order to thrive, bacteria have developed ways to maintain cellular homeostasis despite abrupt environmental changes (stress). In this thesis, we focus on osmotic stress. Osmolality is the osmotic pressure of a solution at a particular temperature. 1 Osm corresponds to 1 mole of osmotically active particles per kilogram of solvent. A 1 M solution of glucose or a 0.5 M solution of NaCl has an osmolality of 1 Osm.

E. coli and osmotic stress

Escherichia coli cells grown under normal osmotic conditions are in osmotic balance and have a typicial rod-like shape (Fig. 1A). When the external medium osmolality suddenly increases the cells undergo a hyperosmotic shift (Fig. 1B). Water leaves the cytoplasm and its volume decreases, which has major impact on the cell physiology (discussed below). Cells can adapt to increased medium osmolality by taking up and/or synthesizing so-called osmoprotectants (Fig. 1C) and resume growth after some time (Fig. 1D). *E. coli* cells can also experience a hypoosmotic shift, that is, when the external medium osmolality suddenly decreases (Fig. 1C). If the cells are either devoid of safety valves (mechanosensitive channels) or fail to open them, water flows into the cytoplasm and creates pressure that might lead to cell lysis (Fig. 1E). Typically, however, the cells open their mechanosensitive channels, which leads to efflux of low molecular weight solutes and helps the cell balance the difference in osmotic pressure (Fig. 1F). Finally, the cells resume growth even after sever osmotic downshifts (Fig. 1G). The focus of this thesis is on the consequences of osmotic upshift for the physiology of *E.coli* cells.

E.coli – osmotic upshift

The high amount of proteins and small molecules dissolved in a bacterial cytoplasm is separated from the cell exterior by the plasma membrane, which creates an osmotic pressure, due to difference of concentrations on both sides of the semi-permeable membrane. The cells maintain turgor to balance the osmotic pressure difference between their interior and exterior.

When cells are subjected to hyperosmotic stress (osmotic upshift) water leaves the cytoplasm and the turgor decreases. The impact of this shock for the cell physiology depends on the magnitude of the osmotic upshift (Fig. 2). We can assign two regimes to osmotic shock: a moderate osmotic upshift (turgor decreases but does not drop to zero) and a severe one (turgor drops to zero).

In cells exposed to a moderate osmotic upshift, the cytoplasm volume decreases because of the lower pressure on the cell envelope (Fig. 2E), which

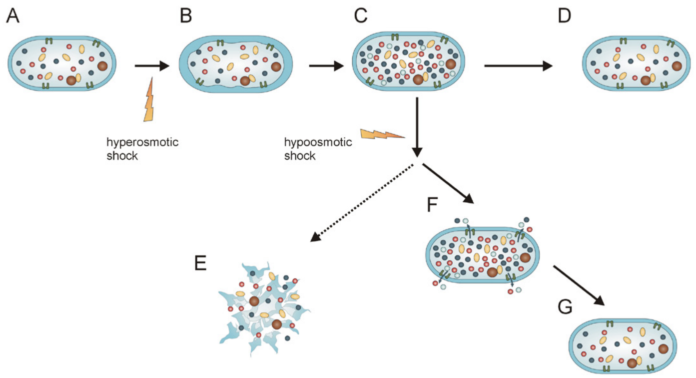

Figure 1. Osmotic stress in E. coli. A cell in osmotic balance (A). Cell just after imposing hyperosmotic stress (B). Cell that has recovered from hyperosmotic stress (C). Cell that resumes growth after hyperosmotic stress (D). Cell that lyses due to hypoosmotic stress (E). Cell that opens mechanosensitive channels as a result of hypoosmotic stress (F). Cell that resumes growth after hypoosmotic stress (G). The yellow lightning symbols indicate hyperosmotic and hypoosmotic shock. Adapted from (Booth *et al.*, 2007), with permission.

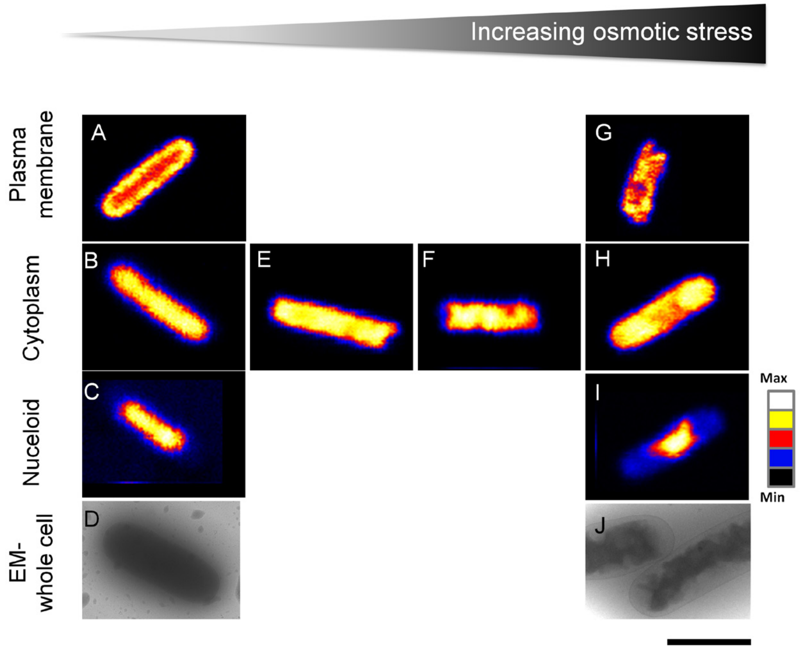

Figure 2. Consequences of osmotic stress on E.coli cell (sub-)structure. Images of cells under different regimes of osmotic upshift and visualized by fluorescence (A-C, E-I) and electron microscopy (D,J). Cell under normal osmotic conditions (A-D) and under moderate (E-F) and severe (G-J) osmotic upshift. Fluorescence intensity is shown in a rainbow setting (see scale) and is specific for cellular subcompartments: the plasma membrane (A,G), the cytoplasm (B, E-H) and the nucleoid (C,I) Electron microscopy images are of whole cells, darker areas correspond to higher electron density (D,J). In case of the severely stressed cells (J) one can distinguish the cell membrane, the periplasm and the highly perturbed, dense cytoplasm. Scale bar 2μm.

translates into an increase of macromolecule crowding. As a result protein mobility decreases, which slows down cell metabolism and growth. If cells are exposed to a severe osmotic upshift, the turgor drops to zero and the plasma membrane retracts from the cell wall and invaginations become visible. Water efflux from the cytoplasm is more pronounced and in the most extreme cases the only water left is that of the hydration of the macromolecules ((Konopka *et al.*, 2007) and references there in). The cytoplasm can shrink to 60% of its initial volume. The plasma membrane is highly invaginated and the cytoplasm loses the initial rod-like shape (Fig. 2G). Macromolecule crowding increases even further and the protein mobility drops orders of magnitude and large complexes become immobile. Under such conditions the cytoplasm does not appear homogenous (Fig. 2H) and apparent barriers for diffusion are formed. These barriers are either formed by the nucleoid or by the increased macromolecular crowding of the cytoplasm. In some severely osmotically upshifted cells, there seems to be a phase separation of the nucleoid and the bulk of the cytoplasm (Fig. 2I). Intriguingly, the severe osmotic upshifts have only moderate impact on the mobility of low molecular weight species (metabolites) in the cell.

Cellular response to osmotic upshift – osmoprotectants

Bacterial cells have developed ways to counteract the effects of hyperosmotic stress. *E.coli* has mechanisms to restore cytoplasm hydration and volume. Osmoprotectants are compounds bacteria either take up or synthesize that allow them grow in media of high osmolality. Compatible solutes are osmoprotectants that can be accumulated in the cytoplasm in high levels without disturbing cellular functions. The action of compatible solutes is dual: they help to regain the hydration of the cytoplasm of osmotically upshifted cells and they stabilize macromolecule structures protecting them from damaging effects of dehydration and desiccation. Bacteria differ in the types of osmoprotectants they use to counter the effects of osmotic stress. For *E.coli* the most important osmoprotectants include: potassium ions, glycine betaine, proline and trehalose. The first three are taken up from the medium by specific transporters, trehalose is synthesized.Immediatelly after osmotic upshift *E.coli* cells start to take up potassium ions to decrease the difference in osmolality. Potassium ions are accumulated by potassium uptake systems (e.g. Trk, Kdp) (Wood, 1999, Ferguson *et al.*, 1996) and the cytoplasmic concentration of this ion at least doubles the initial 0.2-0.3 M when the growth medium osmolality increases by 1 Osm (Wood, 2011). In parallel to potassium accumulation, *E.coli* cells start to take up glycine betaine and proline (via the ProU and ProP membrane transporters, (Wood *et al.*, 2001)). These two compatible solutes reach highest concentrations in the cytoplasm within 10-20 minutes after imposing the osmotic upshift (Wood, 2011, Wood *et al.*, 2001) and gradually replace the potassium. After 30 minutes of osmotic upshift, the cell starts producing its own osmoprotectant-trehalose (synthesized by the OtsA and OtsB proteins). The cytoplasmic concentration of trehalose increases tenfold (from 0.04 to 0.4 M, (Wood, 2011)) and after two hours the cell has replaced most of its initial osmoprotectants by this carbohydrate (Dinnbier *et al.*, 1988).

Osmotic stress as a tool to manipulate macromolecule crowding in cells

The pioneering study of Elowitz and co-workers (Elowitz *et al.*, 1999) on diffusion of GFP in living *E.coli*, using Fluorescence Recovery After Photobleaching (FRAP), was the first to probe macromolecule mobility in small prokaryotic cells. Osmotic perturbation is a powerful tool of manipulating cytoplasmic (macro)molecule concentration *in vivo*, which we have used to address questions on the structure and diffusional properties of the *E.coli* cytoplasm. We have used two different FRAP-based techniques (pulsed-FRAP, chapters 3 and 4 and “conventional FRAP” in chapter 3 and 5) to study (macro)molecule diffusion and the cell’s physiologial response to osmotic shift in the presence and absence of osmoprotectants.

Outline of the thesis

This thesis is divided in two parts. Chapters 2-6 focus on diffusion of (macro)molecules in the crowded environment of living *E.coli* cells and the consequences of osmotic stress. The second part of the thesis contains two chapters in which the action of pore-forming antimicrobial peptides in model membranes is studied, employing various fluorescence-based techniques in parallel with molecular dynamics simulations.

Chapter 2 presents an overview of recent studies on macromolecule mobility in prokaryotic cells, including methods to probe diffusion in small compartments like bacterial cells and cell organelles. We evaluate measurements of 2D diffusion in model membranes and membranes of living cells as well as 3D diffusion in aqueous media and crowded environments. Unlike for soluble proteins, where the molecular weight (dimensions) has a major impact on diffusion (D is inversely proportial to the hydrodynamic radius of the protein; $D \sim 1/R$), in membranes the D scales logarithmically with the lateral radius of the transmembrane part of the diffusing object [$D \sim \ln(1/R)$]. On the basis of experimental data from different groups, a dependence of diffusion on molecule size is derived for molecules in the crowded cytoplasm of *E. coli*. The diffusion in the cytoplasm of prokaryotes is much slower than in dilute aqueous solutions and slower than in the cytoplasm of eukaryotic cells, which we rationalize by the higher macromolecule crowding in the prokaryotes. Despite the crowdedness, even the largest molecules can traverse the entire cell volume several times within the life span of a bacterium.

Chapter 3 evaluates two FRAP methods that are most frequently used to probe the mobility of molecules in bacterial cells: pulsed-FRAP and "conventional FRAP". Several researchers have determined the translational diffusion of GFP in *E. coli*, however the reported D values range from 3-3.5 $\mu m^2/s$ (van den Bogaart *et al.*, 2007, Mika *et al.*, 2010), through 6-7 $\mu m^2/s$ (Konopka *et al.*, 2006, Elowitz *et al.*, 1999, Mullineaux *et al.*, 2006) up to 14 $\mu m^2/s$ (Konopka et al, 2009). To determine whether or not this apparent discrepancy arises from the differences in methods used, we compared pulsed-FRAP and "conventional

FRAP". We show that these methods give comparable results, implying that the reported differences are due to experimental variations in the biology (e.g. different growth media, handling of cells, etc.) rather than differences between the techniques.

Chapter 4 addresses the mobility of differently sized molecules in the cytoplasm of *E.coli*. Cells under normal osmotic conditions were compared with cells under osmotic upshift. We find that the mobility of the molecules drops with their size and that the crowded environment has a larger impact on (large) macromolecules than on metabolites. In other words, the decrease in mobility does not obey the Einstein-Stokes law. Under severe osmotic conditions, the diffusion of GFP and larger proteins is more strongly hindered and apparent barriers for mobility are observed. The barriers can be either due to the nucleoid forming an obstacle for diffusion or due to increased macromolecule crowding itself. Interestingly, even under the most severe osmotic stress (osmotic upshift by 2M NaCl), molecules of the size of metabolites and compatibles solutes are still fairly mobile and this may provide the cell with means to accumulate osmoprotectants and thereby to recover from the stress conditions.

Chapter 5 shows the kinetics of the ultrastructural changes in the cell and recovery from osmotic stress at the single cell level. By following individual cells, we observe that the physiological response is heterogeneous in the probed population. While most cells recover from osmotic shock, the values of diffusion and cytoplasmic volume of individual cells are rather divers.

Chapter 6 describes the in-house developments of super-resolution microscopy of bacterial cells. Owing to the fact that the diffraction limit of light microscopy is only an order of magnitude smaller than the size of an *E.coli* cell, only a limited detail of bacterial ultrastructure is obtained by conventional light microscopy. We have built a Photo-Activated Localization Microscopy (PALM) set up that allows us to visualize macromolecules in bacterial cells with 10 nm precision. We describe our initial work to employ different photo-switchable fluorescent proteins required for PALM imaging. We demonstrate the visualization of the *E.coli* cytoplasm and nucleoid with two, spectrally distinguishable proteins: mEos2 and eYFP, which allow us to perform dual-color PALM.

Chapter 7 describes the molecular basis of antimicrobial activity of cyclic and linear peptides, topologically different but identical in sequence. We establish that, relative to the linear peptide, the cyclic one binds stronger to negatively-charged membranes. We show that only the cyclic peptide folds at the membrane interface and adopts a b-sheet structure characterized by two turns, which allows it to penetrate deeper into the bilayer. We propose that the molecular basis for the enhanced activity of the cyclic peptide resides in the restricted number of conformations relative to the linear peptide.

Chapter 8 focusses on the poration propensity of the cyclic and linear peptides. Unlike its linear counterpart, in the molecular-dynamics simulations, the cyclic peptide caused large perturbations in the bilayer and cooperatively opened a disordered toroidal pore, 1-2 nm in diameter. Electrophysiology and Dual-Color Fluorescence Burst Analysis (DCFBA) measurements on model membranes treated with the different peptides are in agreement with the molecular dynamics simulations. We show that both peptides are able to fuse/aggregate liposomes, but only the cyclic peptide is able to porate them.

References

Booth, I. R., M. D. Edwards, S. Black, U. Schumann & S. Miller, (2007) Mechanosensitive channels in bacteria: signs of closure? *Nat Rev Microbiol* **5**: 431-440.

Dinnbier, U., E. Limpinsel, R. Schmid & E. P. Bakker, (1988) Transient accumulation of potassium glutamate and its replacement by trehalose during adaptation of growing cells of *Escherichia coli* K-12 to elevated sodium chloride concentrations. *Arch Microbiol* **150**: 348-357.

Eckburg, P. B., E. M. Bik, C. N. Bernstein, E. Purdom, L. Dethlefsen, M. Sargent, S. R. Gill, K. E. Nelson & D. A. Relman, (2005) Diversity of the human intestinal microbial flora. *Science* **308**: 1635-1638.

Elowitz, M. B., M. G. Surette, P. E. Wolf, J. B. Stock & S. Leibler, (1999) Protein mobility in the cytoplasm of *Escherichia coli*. J Bacteriol **181**: 197-203.

Ferguson, G. P., A. D. Chacko, C. H. Lee & I. R. Booth, (1996) The activity of the high-affinity K+ uptake system Kdp sensitizes cells of *Escherichia coli* to methylglyoxal. J Bacteriol **178**: 3957-3961.

Konopka, M. C., I. A. Shkel, S. Cayley, M. T. Record & J. C. Weisshaar, (2006) Crowding and confinement effects on protein diffusion *in vivo*. *J Bacteriol* **188**: 6115-6123.

Konopka, M. C., Sochacki, K. A., Bratton, B. P., Shkel, I. A., Record, M. T., Weisshaar, J. C., (2009) Cytoplasmic protein mobility in osmotically stressed *Escherichia coli*. *J Bacteriol* **191**: 231-237.

Konopka, M. C., J. C. Weisshaar & M. T. Record, Jr., (2007) Methods of changing biopolymer volume fraction and cytoplasmic solute concentrations for *in vivo* biophysical studies. *Methods Enzymol* **428**: 487-504.

Mika, J. T., G. van den Bogaart, L. Veenhoff, V. Krasnikov & B. Poolman, (2010) Molecular sieving properties of the cytoplasm of *Escherichia coli* and consequences of osmotic stress. *Mol Microbiol* **77**: 200-207.

Mullineaux, C. W., A. Nenninger, N. Ray & C. Robinson, (2006) Diffusion of green fluorescent protein in three cell environments in *Escherichia coli*. *J Bacteriol* **188**: 3442-3448.

van den Bogaart, G., N. Hermans, V. Krasnikov & B. Poolman, (2007) Protein mobility and diffusive barriers in *Escherichia coli*: consequences of osmotic stress. *Mol Microbiol* **64**: 858-871.

Vendeville, A., D. Lariviere & E. Fourmentin, (2011) An inventory of the bacterial macromolecular components and their spatial organization. *FEMS Microbiol Rev* **35**: 395-414.

Wood, J. M., (1999) Osmosensing by bacteria: signals and membrane-based sensors. *Microbiol Mol Biol Rev* **63**: 230-262.

Wood, J. M., (2011) Bacterial Osmoregulation: A Paradigm for the Study of Cellular Homeostasis. *Annu Rev Microbiol* **65**: 215-238.

Wood, J. M., E. Bremer, L. N. Csonka, R. Kraemer, B. Poolman, T. van der Heide & L. T. Smith,

(2001) Osmosensing and osmoregulatory compatible solute accumulation by bacteria. *Comp Biochem Physiol A Mol Integr Physiol* **130**: 437-460.

CHAPTER 2

MACROMOLECULE DIFFUSION AND CONFINEMENT IN PROKARYOTIC CELLS

Jacek T. Mika & Bert Poolman

Current Opionion in Biotechnology 2011, **22**:117-126

We review recent observations on the mobility of macromolecules and their spatial organization in live bacterial cells. We outline the major fluorescence microscopy-based methods to determine the mobility and thus the diffusion coefficients (D) of molecules, which is not trivial in bacterial cells, due to their small size. The extremely high macromolecule crowding of prokaryotes is used to rationalize the reported lower diffusion coefficients as compared to eukaryotes, and we speculate on the nature of the barriers for diffusion observed for proteins (and mRNAs) *in vivo*. Building on in-vitro experiments and modeling studies, we evaluate the size dependence of diffusion coefficients for macromolecules *in vivo*, both in case of water-soluble and integral-membrane proteins. We comment on the possibilities of anomalous diffusion and provide examples where the macromolecule mobility may be limiting biological processes.

Introduction

The reductionist's approach in biochemistry is essential to elucidate biological mechanisms with molecular detail. However, to understand how a protein functions in a real cell and to capture all possible regulatory mechanisms, one needs to analyze molecules in their cellular environment and be able to perturb the system for obtaining mechanistic information. A major difference between *in-vivo* and *in-vitro* conditions is the crowdedness (and associated molecular complexity) of the cytoplasm and biological membranes (Ellis, 2001). For instance, the intracellular levels of proteins, RNA plus DNA in a *Escherichia coli* cell can reach up to 400 g/l (*e.g.,* when cells are osmotically stressed), concentrations close to that in protein crystals. Figure 1 pictures the crowding of the *E. coli* cytoplasm at a protein concentration of 275 g/l (McGuffee & Elcock). The consequences of increased macromolecule crowding on the cellular constituents are most pronounced for the activity coefficients of the molecules, the oligomeric states of the proteins, reaction equilibria and molecule diffusion coefficients (see (Ellis, 2001, Verkman, 2002, Zhou *et al.*, 2008) for excellent reviews). Diffusion, albeit passive, is the main process for transport and mixing of components in prokaryotic cells. A high crowding will lower mobility and may thus slow down reactions and reduce the reorganization and dynamics of cellular components. On the other hand, a high crowding will favor (self)-association of molecules.

Although *Escherichia coli* is probably the best-characterized organism in terms of genetics and physiology, until a few years ago surprisingly little was known about the translational diffusion and dynamics of macromolecules or their complexes in this organism or any prokaryote. This is likely due to the small size of bacteria and archaea, which complicates dynamic studies by fluorescence microscopy. For instance, a typical *E. coli* cell is 3 µm long and 1 µm wide, which is only a few times more than the resolution of conventional light microscopy; *e.g.,* the diffraction-limited spot is about 0.22 µm in the lateral direction for 550-nm wavelength light (Huang *et al.*, 2009).

The effect of crowding on protein diffusion in eukaryotic cells has been comprehensively reviewed by Dix and Verkman (Dix & Verkman, 2008). Here, we

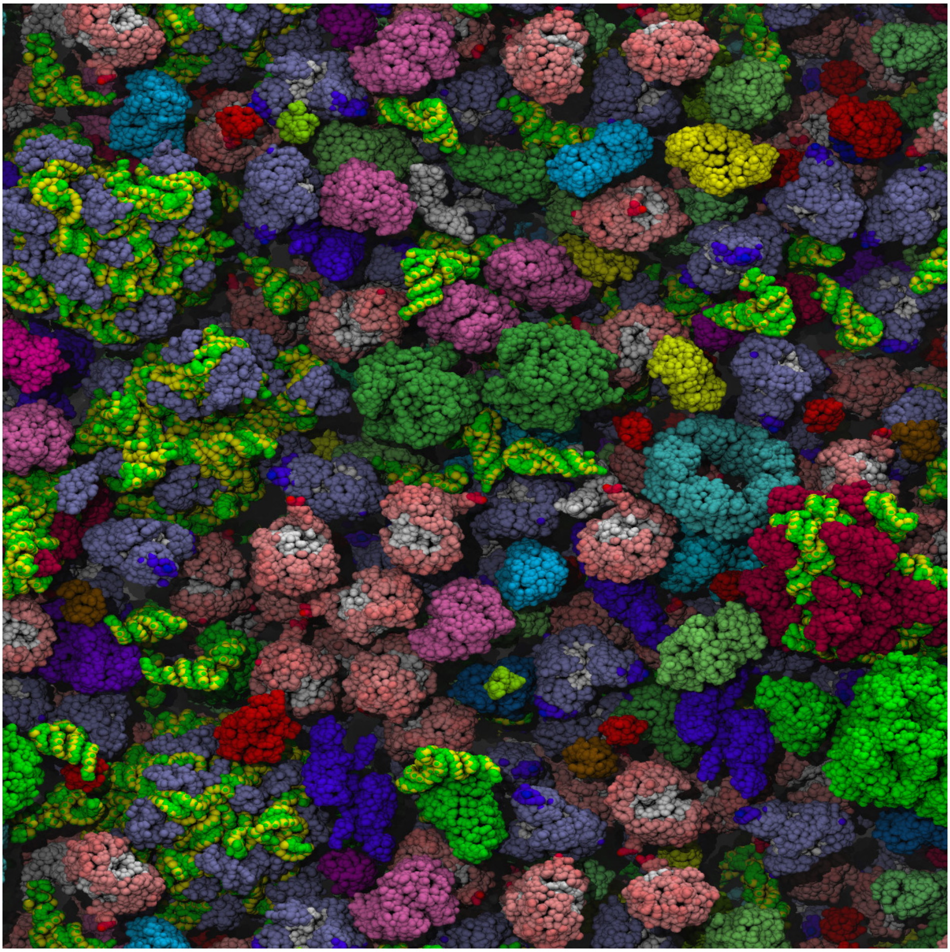

Figure 1. Crowding in the cytoplasm of bacteria. A snapshot of a simulation of the *E. coli* cytoplasm at a protein concentration (275g/L), approximating the *in vivo* conditions (McGuffee & Elcock); with permission from Adrian Elcock.

focus on the challenges of determining translational diffusion in small cells (see section below), and evaluate recent measurements on *in-vivo* diffusion coefficients in prokaryotes. We feel that this kind of data and quantization of biology is important for systems biology approaches aimed at an understanding of the workings of a cell. We discuss the current literature on macromolecule mobility and barriers for diffusion inside living cells, with a focus on prokaryotes where crowding conditions seem most extreme. Some outstanding questions include: How much is the diffusion slowed down compared to aqueous media and what is the difference in mobility in prokaryotic and eukaryotic cells? What is the diffusion coefficient in different cellular environments like the cytoplasm and the membrane? How much does the diffusion coefficient depend on the molecular weight (shape) of the macromolecules? Is the diffusion inside prokaryotes anomalous? Do proteins roam around in the cytoplasm freely and in a random fashion or is their mobility restricted to pools or sub-domains (spatial organization)? What are the cases where diffusion is limiting a biochemical process? Is there a role for variations in *D* in regulating the overall rate of biochemical reactions?

Crowding and diffusion in the cytoplasm

Bacteria are described to be more crowded than eukaryotic cells, presumably because more functions need to be concentrated in a small compartment (for instance, the volume of *E. coli* is 2 fL, which is 3-5 orders of magnitude less than that of mammalian cells). Macromolecule concentrations in *E. coli* grown under typical laboratory conditions (Luria-Bertani medium of osmolarity of ~0.44 Osm) are in the range of 300-370 g/L of protein plus RNA (Zimmerman & Trach, 1991). More specifically, Cayley and co-workers. (Cayley *et al.*, 1991) have determined concentrations of 200 g/L of protein, 75 g/L of RNA and 10-20 g/L of DNA. In comparison the slime mould *Dictyostelium discodeum* has a similar protein concentration (~220 g/L) but the levels of DNA (~1.13 g/L) and RNA (12.8 g/L) are much lower (Ashworth & Watts, 1970). Studies on human brain cells point towards protein concentrations in the range of 50-100 g/L protein

(Winick, 1968, Conlon & Raff, 2003), which is much lower than for bacteria. The high macromolecular crowding of bacteria (Fig.1) has clear impact on the mobility of molecules. For example, typical values for diffusion coefficients of GFP in the cytoplasm of *E. coli* are between 3 and 8 µm^2/s (see Fig.3A; the wide range of values may reflect differences in physiological states of the cells and methodological differences). The mobility of GFP in live *E. coli* cells is an order of magnitude slower than in diluted aqueous solutions (87 µm^2/s, (Potma *et al.*, 2001)) and also slower than in eukaryotic cytoplasm (*e.g.,* 27 µm^2/s in Swiss 3T3 fibroblasts (Swaminathan *et al.*, 1997) or 24 µm^2/s (Potma *et al.*) in *D. discoideum*). The faster diffusion coefficient in *D. discoideum* may reflect the much lower RNA concentration as the protein crowding seems similar to that of prokaryotic cells, whereas in higher eukaryotes both the protein and nucleic acid concentrations are lower than in bacteria.

When bacterial cells are subjected to osmotic upshift (increase in the osmolality of external medium) a passive loss of cytoplasmatic water occurs. As a result, the volume of the cytoplasm decreases. If the hyperosmotic shock is severe cells can lose up to 70% of the cytoplasmatic water (Konopka *et al.*, 2007), and what is left are the hydration shells of the (macro)molecules. In *E. coli* grown at osmolarities of 1.02 Osm, the macromolecule concentration reaches values as high as 320 g/l of protein and 120 g/l of RNA (Cayley *et al.*, 1991). Thus, by subjecting cells to osmotic upshift one can increase the cytoplasmatic biopolymer volume fraction. As shown by Konopka (Konopka *et al.*, 2006) and van den Bogaart (van den Bogaart *et al.*, 2007), this increased crowding is reflected by a lower molecule mobility; the drop in diffusion coefficients is proportional to the osmotic upshift applied (Mika *et al.*, 2010).

Barriers for diffusion in the cytoplasm

Konopka reports that in osmotically upshifted cells (ΔOsm = 0.7 Osm, equivalent to a medium supplement of 400 mM NaCl) cytoplasmic diffusion of GFP is reduced to 0.014 µm^2/s (Konopka *et al.*, 2006), which is two orders of magnitude slower than in cells at typical osmotic conditions of ~0.44 Osm. Un-

Text box 1:
How to measure (macro)molecule mobility in live bacteria?

SMT. In Single Molecule Tracking (SMT) the localization of a fluorescent molecule is traced over time. The trajectory of movement can be plotted and analyzed as a function of time (Fig. 2) to obtain a diffusion coefficient. If the molecule shows Brownian dynamics, the diffusion is called normal and the mean square displacement increases linearly with time. If the displacement of the molecule does not scale linearly over long(er) time scales, the diffusion is anomalous (see Fig. 2A and Text Box II). SMT is perhaps the method of choice to discriminate between normal and anomalous diffusion. While SMT is a powerful tool to study single molecule diffusion in dilute solutions, it encounters a number of experimental difficulties when performed in live cells. The main ones are background fluorescence of the cytoplasm, which renders it difficult to visualize single molecules *in vivo* (low signal from fluorescent proteins relative to autofluorescence), resulting in low signal-to-noise ratios. Although most observations on molecule diffusion in prokarya are based on *E. coli* (Golding & Cox, 2006, Biteen & Moerner, 2010, Fukuoka *et al.*, 2007, Leake *et al.*, 2008, Lenn *et al.*, 2008, Xie *et al.*, 2008), which is highly autofluorescent, it should be easier to perform SMT and other single-molecule measurements in fermentative bacteria lacking respiratory components. Moreover, progress on *in situ* single-molecule measurements is also facilitated by recent technical developments, such as total-internal reflection (TIR) microscopy, more sensitive EM-CCD cameras, stroboscopic illumination and new photoactivatable fluorescent proteins (*e.g.* Dronpa, mEos2).

FCS. Another single-molecule approach to determine diffusion coefficients is Fluorescence Correlation Spectroscopy (FCS; Fig. 2B) (Bacia *et al.*, 2006). While very powerful in determining *D* values in solution (Dauty & Verkman, 2004) and *in vitro* membrane systems like giant-unilamellar vesicles (GUVs) (Ramadurai *et al.*, 2009), FCS measurements of diffusion in small cells or cell organelles remain challenging. The reason is the small and confined volume of such structures. On the one hand there are insufficient molecules to provide enough signal to reliably determine *D* before the photobleaching of the fluorophore occurs. On the other hand, the background fluorescence of cells makes it difficult to obtain satisfactory signal-to-noise ratios. Moreover, the presence of a bacterial cell (or a similar dense structure) in the observation volume can influence its geometry, which would hamper quantitative determination of *D* values. To date the number of studies reporting diffusion coefficients measurements by FCS in live bacteria is very limited (Cluzel *et al.*, 2000).

FRAP. Despite lacking the single-molecule sensitivity characteristic of SMT and FCS, Fluorescence Recovery After Photobleaching (FRAP) has proven to be very successful in determining the mobility of macromolecules both in prokaryotic (Mika *et al.*, 2010, Konopka, 2009, Konopka *et al.*, 2006, van den Bogaart *et al.*, 2007, Elowitz *et al.*, 1999, Kumar *et al.*, 2010, Mullineaux *et al.*, 2006, Nenninger *et al.*, 2010) and eukaryotic cells (Verkman, 2002, Dix & Verkman, 2008, Seksek *et al.*, 1997, Swaminathan *et al.*, 1997). In a traditional FRAP experiment, a cell is first imaged with weak laser illumination. Subsequently a Region Of Interest (ROI) is photobleached with an intense laser pulse and the cell is then imaged over time with a low-intensity laser illumination to record the recovery of fluorescence, which results from the diffusion of the non-bleached fluorophores into the ROI. Since bacterial cells are small, FRAP protocols need to be tailored to obtain satisfactory data (*i.e.* the laser beam needs to be small and weak enough to leave a significant portion of the cytoplasm unbleached to allow recovery). Below we summarize the main features of these methods.

Conventional-FRAP. In the initial pioneering studies to quantify protein diffusion in bacteria, Elowitz (Elowitz *et al.*) used a FRAP protocol schematically depicted in Fig.2C, here referred to as “conventional FRAP”. A region at the pole of the cell is bleached and subsequently the cell is imaged during recovery. By taking cross-sections through the longer cell axis at consecutive time points, one obtains a temporal plot of the fluorescence distribution throughout the cell (Fig.2C, right), which can be fitted to a one-dimensional diffusion model and yield *D* values. This approach was also employed by Konopka and co-workers to measure the changes of diffusion of GFP in the cytoplasm of *E.coli*, following osmotic upshift (Konopka *et al.*, 2006) and osmoadaptation (Konopka, 2009). Some other groups (Kumar *et al.*, 2010, Mullineaux *et al.*, 2006, Nenninger *et al.*, 2010) have used a similar protocol since.

Pulsed–FRAP. Van den Bogaart developed a version of FRAP termed pulsed-FRAP (van den Bogaart *et al.*, 2007), schematically depicted in Figure 2D. In pulsed-FRAP a single, relatively weak laser beam is used both for bleaching and imaging. In brief, a cell is first imaged with a confocal microscope and a diffraction limited laser beam is positioned in the middle of the cell. Subsequently, a series of weak, short pulses is applied, separated by time intervals to allow the fluorescence to recover. The fluorescence recorded during the pulses is influenced by the photobleaching of the GFP in the focal spot (decrease of fluorescence intensity) and by diffusion of the non-photobleached fluorophore into the focal spot (increase of fluorescence intensity). When a sufficient number of fluorescence decays has been acquired (on average 10 to 15), the data are fitted to a suitable diffusion model. Knowing the area (volume) of the probed cell one can calculate theoretical bleaching curves and fit the experimental data to obtain a diffusion coefficient and a bleaching constant. Pulsed-FRAP was used by van den Bogaart (van den Bogaart *et al.*, 2007) to determine the diffusion of GFP in *E.coli* cells and later by Mika and colleagues (Mika *et al.*, 2010) to determine the diffusion coefficient of (macro)molecules of different molecular weight under various osmotic conditions.

CP-TIR. Slade and co-workers have combined Continous Photobleaching (CP) with Total Internal Reflection (TIR) microscopy to determine diffusion coefficients of GFP under normal conditions (Slade *et al.*, 2009b) and in cells overexpressing proteins (Slade *et al.*, 2009a). TIR illumination limits the laser light path in the axial direction and allows the photobleaching volume to be restricted to only a small subvolume of the cytoplasm, leaving enough non-photobleached GFP outside of the excitation region to observe fluorescence recovery with good signal-to-noise ratios (Fig.2E). In CP-TIR varying laser intensities are used to discriminate between the two competing processes, that are: (i) photobleaching in the illuminated region and (ii) fluorescence recovery (resulting from diffusion of the non-photobleached fluorophore outside of that region). By comparing CP-TIR curves at different laser intensities, rate constants of diffusion and bleaching can be calculated.

der similar osmotic stress conditions van den Bogaart also reports a dramatic loss of GFP mobility, which coincides with the formation of cytoplasmic diffusion barriers (van den Bogaart *et al.*, 2007). The distribution of GFP is no longer equal throughout the cell, instead the cell appears compartmentalized with pools of GFP that do not exchange their contents. It was subsequently shown that the barriers for the mobility of GFP and bigger macromolecules are likely to be formed by the nucleoid (a kind of physical obstacle for diffusion) and the high macromolecular crowding of the cytoplasm (Mika *et al.*, 2010). Interestingly, no such barriers were observed for low molecular weight compounds (Fig. 3B).

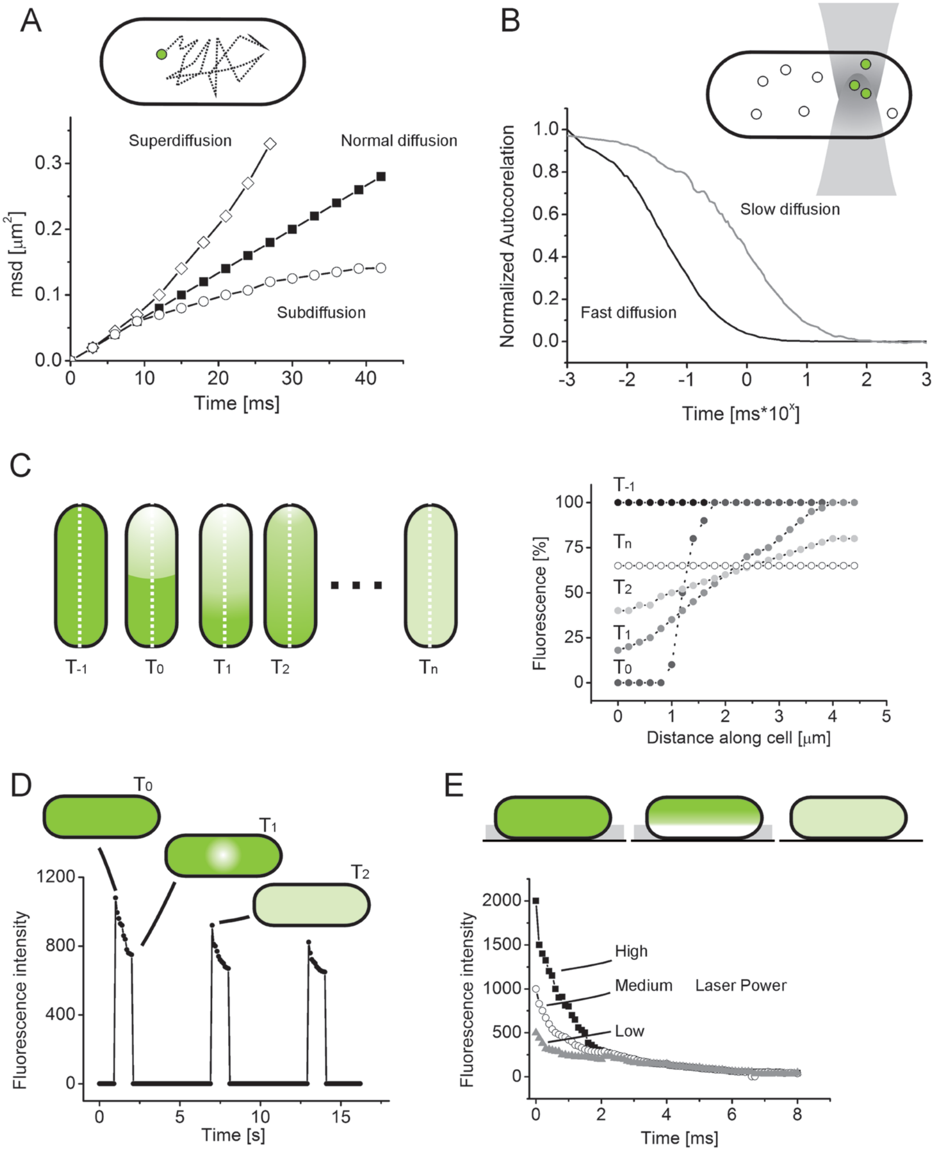

Figure 2. Fluorescence microscopy methods for determining the translational diffusion of (macro)molecules. A) Single Molecule Tracking; B) Fluorescence Correlation Spectroscopy; C) Conventional FRAP; D) pulsed-FRAP; and E) Continous Photobleaching with Total Internal Reflection microscopy.

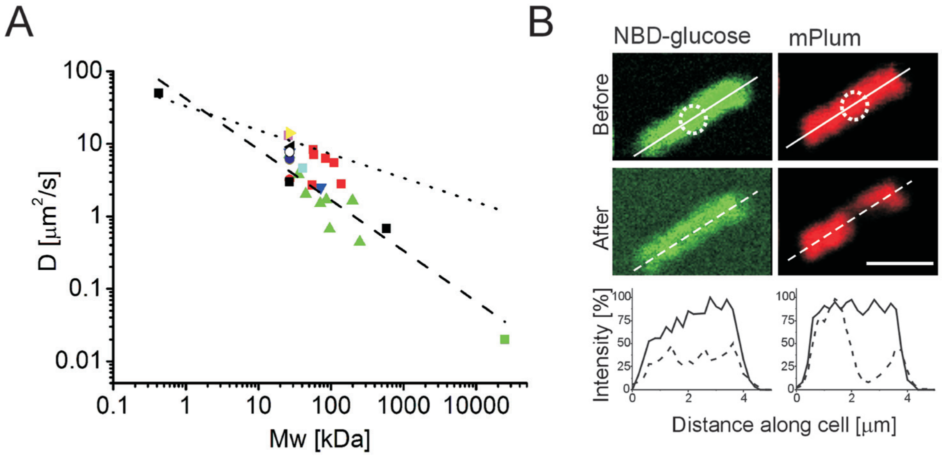

Figure 3. Molecule diffusion in live cells. Panel A: Molecule diffusion *in vivo* as a function of molecular weight (Mw). The data was fitted with a power-law dependence: $D = aMw^x$ (see Text Box I for details). Dashed and dotted lines represent the fits; dashed: $x = -0.7$ (best fit) and dotted: $x = -0.33$ (Einstein-Stokes dependence). Symbols: (■) NBD-glucose, GFP and (β-galactosidase-GFP)$_4$ (Mika *et al.*, 2010); (●) GFP (van den Bogaart *et al.*, 2007); (▲) YFP, PtsH-YFP, Crr-YFP, CFP-CheR-YFP, DnaK-YFP, HtpG-YFP and CFP-CheA-YFP (Kumar *et al.*, 2010); (▼) GFP and MBP-GFP (Elowitz *et al.*, 1999);(■) CheY-GFP (Cluzel *et al.*, 2000), (■) mEos2 (English, 2010) ; (●)GFP (Konopka *et al.*, 2006); (▶) GFP (Konopka, 2009); (●) GFP (Slade *et al.*, 2009b); (◀) TorA-GFP (Mullineaux *et al.*, 2006); (○) GFP (Slade *et al.*, 2009a); (■) NlpA$_{(\text{No LB})}$-GFP, TorA-GFP2, AmiA$_{(\text{no SP})}$-GFP, TorA-GFP3, TorA-GFP4 and TorA-GFP5 (Nenninger *et al.*, 2010); (■) plasmid-protein complex (Derman *et al.*, 2008). Panel B: The cytoplasm of osmotically-upshifted cells forms mobility barriers for proteins (mPlum) but not for small molecules (NBD-glucose). Pseudo-colored images of a mPlum expressing *E. coli* single cell loaded with NBD-glucose and treated with 0.5 M NaCl (ΔLB = 0.85 Osm). Left panels, NBD-glucose (Leake *et al.*) and right panels, mPlum (red). The dotted circle indicates the photo-bleached spot. Upper panels show cells before, and lower panels 2 min after, photo-bleaching. The graphs indicate the normalized fluorescence intensities of the cell along the longer cell axis (indicated by the white lines). Scale bar 2 μm. From Mika *et al.* (Mika *et al.*).

Even in cells subjected to 2 M NaCl (ΔOsm = 4.5), a fluorescent-labeled sugar molecule remained fairly mobile and distributed evenly over the cytoplasmic space. This result has two important consequences. First of all, it implies that the cytoplasm acts as a molecular sieve. Under conditions of increased biopolymer volume fraction, when little 'free' cytoplasmatic water is left and crowding is increased to an extent that proteins are on average less than 1nm apart, proteins of only a few nm in diameter (*e.g*. 2 nm for the ~27 kDa GFP) are trapped by the constrictions or density of the macromolecular meshwork. Secondly, the relatively fast diffusion of small molecules (like ions, sugars, signaling molecules and metabolites) will keep the cell biochemically active. The view of the cytoplasm as a molecular sieve is further supported by the recent work of Kumar (Kumar *et al.*, 2010), who observed a steep drop in diffusion coefficients with increasing molecular weight of the diffusing molecule.

Relationship between diffusion coefficient and macromolecule molecular weight

Over the last 10 years, diffusion coefficients have been determined for quite a number of (macro)molecules in live bacteria, in most cases using *E. coli* as a model organism. We have plotted the collected data and used the power law dependence as a fit (Fig. 3A, see Text box 2). We find a value for *x* of -0.7, which differs significantly from the Einstein-Stokes exponent of -0.33. We note that most diffusion coefficients hold for a limited range and that extrapolations to low molecular weight molecules and supramolecular complexes should be taken with care. There are a number of reasons to be cautious: Firstly, the spread in the actual data is large, which may have a biological origin (population heterogeneity, medium differences) and in part be technical (different types of measurement and data analysis).

Secondly, by introducing a fluorescent tag, one not only renders the molecule amenable for fluorescence microscopy, but also influences its size, shape and stability. Kumar *et al.* (Kumar *et al.*, 2010) report that their YFP fusions were subject to degradation and it cannot be excluded that heterogeneous populations of macromolecules have been probed in some studies, rather than

Text box 2:
Mean square displacement (MSD) and diffusion in 2D and 3D

The MSD (d^2) depends on the diffusion coefficient (D) and time (t), according to equation 1:

$$< d^2 >= bDt^{\alpha} \quad , \qquad (1)$$

in which b is a dimension constant equal to 4 for 2D diffusion (*e.g.* in membranes) and b = 6 for 3D diffusion (in the cytoplasm); α is the anomalous diffusion coefficient. If α = 1, we are dealing with normal (Brownian) diffusion, and MSD scales linearly with time. When α < 1 the molecule's mobility decreases with time, which is referred to as sub-diffusion. If α > 1, we are dealing with super-diffusion. See also Fig 2A.

The Einstein-Stokes relationship (3D diffusion):
Diffusion in dilute aqueous media is described by:

$$D = \frac{k_B T}{6\pi\eta R_S} \quad , \qquad (2)$$

where D is the diffusion constant, k_B, the Boltzman constant, T, temperature, η the viscosity of the medium and R_s, the Stokes radius of the particle. For globular proteins, R_s is related to the cubic root of the molecular weight:

$$R_S = \sqrt[3]{\frac{3Mw}{4\pi N_A \rho}} \quad , \qquad (3)$$

where, Mw is the molecular weight, N_A the Avogadro constant and ρ the density of a protein. This can be further simplified to a power law dependence:

$$D = aMw^{x} \quad , \qquad (4)$$

where a is a scaling factor and x the exponent that describes the drop of D with increasing Mw. For proteins in infinitely dilute solutions (e.g. protein in buffer), the D(Mw) dependence follows the Einstein-Stokes relationship and the exponent x = -0.33.

The Saffman-Delbrück relationship (2D diffusion)
Saffman-Delbrück's continuum hydrodynamic model describes lateral and rotational diffusion of objects moving in a 2D fluid, *e.g.* a lipid membrane (Saffman & Delbruck, 1975). The protein is considered a cylindrical entity moving in a continuous viscous fluid of defined height (h), which is separated by fluids of lower viscosity (aqueous environment). The lateral diffusion coefficient (D) can be expressed as:

$$D = \frac{k_B T}{4\pi\mu h}\left(\ln\left(\frac{\mu h}{\mu' R}\right) - \gamma\right) \quad , \qquad (5)$$

where k_B is the Boltzmann constant, T is absolute temperature, h is the thickness of the bilayer, µ is viscosity of the membrane, µ´ is viscosity of the outer liquid, R is the radius of the diffusing object, and γ is Euler's constant.

one type of species with a well defined Mw. Similarly, upon overexpression part of the protein may be present in aggregates, *e.g.* inclusion bodies, which may explain the discrepancy in diffusion coefficient for the same large complex as reported by Elowitz *et al* (Elowitz *et al.*, 1999) and Mika *et al* (Mika *et al.*, 2010). Thirdly, molecules may non-specifically (electrostatically) interact, which would lead to an underestimation of diffusion coefficients. Indeed, in a comprehensive Brownian dynamics simulation of the bacterial cytoplasm (McGuffee & Elcock, 2010), where some 50 most abundant *E. coli* proteins were studied at a concentration that resembles the *in vivo* situation (275 g/L), proteins of similar mass (Mw) yielded different (up to an order of magnitude) diffusion coefficients (*D*). The simulations are supported by recent experimental data (Kumar *et al.*, 2010, Nenninger *et al.*, 2010). Nonetheless, a general decrease of mobility with increasing macromolecule size is consistently observed (McGuffee & Elcock, 2010, Kumar *et al.*, 2010, Mika *et al.*, 2010) and the decay of *D* with Mw in bacterial cells is steeper than what is predicted by the Einstein-Stokes relationship (see Text box 2).

Diffusion in bacterial membranes

Diffusion of membrane proteins and peptides has been well characterized in artificial membrane systems like Giant Unilamellar Vesicles (GUVs) (Ramadurai *et al.*, 2009). In contrast to soluble (cytosolic) proteins the overall Mw of membrane proteins seems to have little influence on their diffusion coefficients. What matters is their mass (radius or number of transmembrane segments (TMS)) in the membrane (Saffman & Delbruck, 1975, Ramadurai *et al.*, 2009, Kumar *et al.*, 2010), which can be explained by the much higher viscosity of the lipid bilayer than that of the aqueous media in which the soluble domains reside. In recent years, different models have been proposed to describe the lateral diffusion of membrane proteins in lipid bilayers. In the Saffman-Delbrück (SD) model (Text Box II), *D* is logarithmically dependent on the radius (*R*) of the diffusing object [$D \sim \ln(1/R)$] and inversely proportional to the thickness of the bilayer and viscosity of the lipid membrane. An alternative heuristic model proposes the diffusion of membrane proteins to be more strongly dependent on their radii than suggested by Saffman-Delbrück, that is, D scales with $1/R$. However, a recent experimental study, using peptides and proteins with lateral radii ranging from 0.5 nm to 4 nm, is most consistent with the SD model. In agreement with these observations, coarse-grained simulations by Guigas and Weiss suggest that the SD model holds for diffusion of membrane proteins with radii smaller than 7 nm, but fails for objects with larger dimensions (Guigas & Weiss, 2006). Thus, different diffusional regimes may have to be considered when comparing relatively small proteins (*e.g.* channels, transporters, redox enzymes) and supramolecular systems (respiratory complexes, flagellar motor). The D values measured *in vivo* are at least an order of magnitude lower than those measured *in vitro*, which can be rationalized by the higher crowding of biological membranes as compared to the artificial membrane systems. In fact, similar to the cytoplasm, biological membranes are highly crowded and lipid-to-protein ratios on weight basis range from ~0.35 (inner mitochondrial membrane) to ~1 (plasma membrane) to >1 secretory vesicles (Zinser *et al.*, 1991). The membrane area fraction occupied by these proteins ranges from 15-35% (Dupuy & Engelman, 2008). This implies that a typical membrane protein with a perimeter of 15 nm is surrounded on average by a shell of lipids of only a few layers thick. Consequently, diffusing objects will be hindered in their mobility. Ramadurai *et al.* (Ramadurai *et al.*, 2009) has shown that in GUVs the membrane protein diffusion coefficients drop linearly with increasing protein-to-lipid ratio in the range of 3 to 3000 proteins per μm^2. However, the highest protein density exploited is still 8-fold lower than that of a typical biological membrane, which has ~25,000 proteins per μm^2 (*i.e.,* an area occupancy of 30%; (Dupuy & Engelman, 2008)).

Provided proteins are not linked to the cytoskeleton or other cellular structure, diffusion rates obtained in bacterial membranes (Kumar *et al.*, 2010, Leake *et al.*, 2008, Mullineaux *et al.*, 2006) are similar to rates obtained for eukaryotic membranes (Crane & Verkman, 2008, Harms *et al.*, 2001). What matters is the membrane crowdedness, however, we emphasize that to date relatively few systematic studies are available and specific lipids effects (degree of saturation, presence of sterols) have not been investigated *in situ* (see Ramadurai *et al* (Ramadurai, 2010b, Ramadurai, 2010a) for the effects on lateral diffusion in membranes of protein crowding, hydrophobic thickness of the lipids and lipid headgroup composition). In general, the diffusion of proteins in membranes of live bacterial cells is slower than that of proteins in the cytosol (Fig. 3A); typical *D* values for a 30 kDa soluble protein are 3-6 $\mu m^2/s$, while for a 30 kDa membrane protein with a radius in the membrane of 2 nm *D* is in the range of 0.1-0.2 $\mu m^2/s$. Even though diffusion is slow, very large complexes are still mobile (Fukuoka *et al.*, 2007, Leake *et al.*, 2006) with *D* values of 0.005 $\mu m^2/s$ for the 3,2 MDa *E. coli* flagellar motor FliG-GFP (Fukuoka *et al.*, 2007).

Is the diffusion normal or anomalous?

The question of whether diffusion in crowded cells is normal or anomalous is still under debate, and depending on the experimental system researchers have come to opposing views. The high excluded volume fraction of the bacterial cytoplasm and membrane is expected to lead to anomalous diffusion (see Text Box I), that is, the effective mean square displacement (msd) of a diffusing species would not scale linearly with time (Fig.2A) (Dix & Verkman, 2008). Moreover, the heterogeneity of the environment (microdomains in cytoplasm and in membranes) would result in the formation of zones of different apparent viscosity and crowding and thus different mobility. While the diffusion within these microdomains might be normal (Brownian), the overall mobility for a molecule traveling a long distance would be affected by hopping between these domains and result in anomalous diffusion. Also the presence of obstacles such as the cell membrane, the nucleoid or the cytoskeleton will introduce boundary conditions to diffusion (Dix & Verkman, 2008). On the basis of measurements of macromolecule mobility *in vitro* crowded solutions and in eukaryotic cells, Dix and Verkman indicate that the notion of anomalous diffusion as a consequence of crowding alone is not correct. They argue that molecules display anomalous diffusion behavior as a result of specific macromolecular interactions (protein-protein or protein-lipid) or in the presence of a barrier (Dix & Verkman, 2008).

Below we summarize the major experimental observations.

By tracking single molecules of mRNA coated with on average 96 bacteriophage MS2-GFP fusion proteins (~3kb long, Mw > 12 MDa), Golding and Cox (Golding & Cox, 2006) report that the diffusion of this ~ 100 nm long molecule inside the *E. coli* cytoplasm is anomalous on the scale of seconds to minutes with α = 0.7. The observed anomalous diffusion (see Fig 2A and Text Box I) is ascribed to the high macromolecular crowding of the cytoplasm and is not affected by the bacterial cytoskeleton. In a computational study of protein diffusion at concentrations reminiscent of those *in vivo*, McGuffe and Elcock (McGuffee & Elcock, 2010) report for proteins of 72-84 kDa a deviation on short timescales from normal diffusion with α as low as 0.7-0.8. The diffusion of the molecules, however, returned to normal with α values between 0.8 and 1 on longer time scales. Anomalous diffusion has been also reported in a study of the *E. coli* chemotaxis pathway proteins (Schulmeister *et al.*, 2008), but here it is questionable whether all the molecules are freely diffusing., The cytoskeletal protein FtsZ, fused to the photoswitchable Denra2, showed two populations, one being stationary and forming cell division rings and the other one mobile but diffusing anomalously (with α = 0.74) (Niu & Yu, 2008). The anomalous diffusion of FtsZ was rationalized by the transient binding of a fraction of free protein to the cytoskeletal rings. Surprisingly, single-molecule tracking of another bacterial cytoskeleton protein MreB (and fused to YFP) in *Caulobacter crescentus* showed normal, Brownian diffusion (Kim *et al.*, 2006). Normal diffusion was also reported for the membrane proteins PleC-YFP (a histidine kinase involved in cell division in *C. crescentus;* (Deich *et al.*, 2004)) and for the TatA-YFP (a component of the twin-arginine protein translocation system of *E.coli;* (Leake *et al.*, 2008)). Similarly, a recent study of mEos2, a GFP variant, in the cytoplasm of *E.coli* points towards normal diffusion in the bacterial cytoplasm (English, 2010). The information on the diffusion of membrane proteins is scarce. CydB-GFP (Lenn *et al.*) (from the respiratory cytochrome *bd*-I complex) and FliG–GFP (Fukuoka *et al.*) (part of the bacterial flagellar motor) have been described to obey both Brownian and anomalous diffusion. Thus, despite convincing theoretical considerations in favor of anomalous diffusion, the translational mobility in the cytoplasm and biological membranes is not generally observed as non-Brownian.

Relevance of diffusion for biological processes

Although diffusion in the crowded cytoplasm of prokaryotes is slow compared to aqueous media, it is still fast on the timescale of most cellular processes. One can calculate how long it would take for a molecule to travel from one end of the cell to another, using equation 1 (see section Text box 2). If we assume an *E.coli* cell to be 3 μm long, we obtain diffusion times of 30 ms for NBD-glucose (M_w = 0.5 kDa; D = 50 μm^2/s), 0.5 s for GFP (27kDa; $D = 3$ μm^2/s), 2 s for β-galactosidase-GFP$_4$ (Mw=580 kDa; D = 0.8 μm^2/s) and 75 s for 25-50 MDa ribosome-loaded mRNAs (D = 0.02 μm^2/s). Assuming a typical doubling time of *E.coli* of 30 minutes even very large complexes can travel forward and backwards several times during the life-span of the cell. The situation, however, becomes very different in osmotically-stressed cells and here the diffusion of macromolecules most likely limits various biochemical processes. A similar estimation can be made for membrane proteins and D values of ~ 0.2 μm^2/s, *e.g.* as observed for the Tar aspartate chemoreceptor (Kumar *et al.*, 2010), translate to a diffusion time of about 11 s to travel between the poles of the cell. On the other hand, for the flagellar rotor (FilG; D = 0.005 μm^2/s) it would take 7.5 min and here the traveling time gets close to the cells' doubling time.

Although the majority of protein(s) and protein complexes will be able to traverse the cytoplasmic and membrane space multiple times during the life-span of a cell, machineries like those involved in transcription and translation are localized in the cell. In a recent paper, Jacobs-Wagner and coworkers even propose that bacteria spatially organize translation by using the chromosome layout as a template (Llopis *et al.*, 2010). At these places, newly synthesized proteins may thus be concentrated as well. We speculate that the slow diffusion in crowded environments contributes to the formation of functional compartments, for instance by promoting rapid interactions and formation of supramolecular complexes. Moreover, the crowding and composition of a cell is not homogenous and proteins can be excluded or enriched at positions like the nucleoid (Mika *et al.*, 2010) or cell pole (Romantsov *et al.*, 2010), which creates different regimes for molecular interactions. In fact, as previously emphasized the "structure" of the cytoplasm is transient (Spitzer & Poolman, 2005); it changes over time and is unlikely to persist throughout the volume of the whole cell.

What are other documented cases of how macromolecule diffusion relates to function? One example comes from studies of the interaction of the Lac repressor with the nucleoid DNA (Elf *et al.*, 2007). This DNA-binding protein displays 1D diffusion (D_{1D} = 0.046 µm^2/s) as it diffuses along the DNA in search of its sequence of recognition. This movement would be too slow for the protein to scan the entire chromosome. If the molecule does not find its target sequence soon enough, it dissociates from the DNA and exhibits fast 3D diffusion throughout the cytoplasm (D_{3D} ~ 3 µm^2/s). It can then bind non-specifically to another DNA segment where it can start the slow search again. Overall, the molecule is estimated to spend 90% of its time nonspecifically-bound to and diffusing along the DNA, and this translates to an apparent diffusion coefficient D_{eff} of 0.4 µm^2/s (Elf *et al.*, 2007).

Another example comes from a FRAP study of the mobility of lipid probes in the membrane of *Bacillus* spores (Cowan *et al.*, 2004). In dormant spores only part of the phospholipids is mobile with D values of 0.11-0.13 µm^2/s, which can be rationalized by the tight packing of lipids to keep the membrane impermeable and to protect the spore. As soon as the spores germinate, yielding vegetative cells, the lateral mobility increases to 1.7 -1.8 µm^2/s with most of the phospholipids being mobile. The increase in lipid mobility coincides with increased membrane fluidity (and permeability) to allow full biochemical activity of the cell. Other cases where a limitation in free diffusion may be a determining factor are in signal transduction (*e.g*. chemotaxis (Sourjik & Armitage, 2010)) and cell division (Kleckner, 2010)).

Conclusion

Prokaryotes are generally devoid of cellular organelles and as such they are less compartmentalized than eukaryotic cells. However, the bacterial cytoplasm is not a randomly-organized soup of macromolecules, and proteins and nucleic acids seem spatially organized. Despite the high crowding of the cytoplasm and the membrane(s), the mobility of molecules is relatively high provided they are not interacting with other cell components. But, even for freely diffusing species, their mobility can limit physiological processes. There is increasing evidence that the (high) macromolecular crowding is used as a means of confining molecules (proteins) to a given location, where they need to perform their function. Also, there is a wealth of theoretical and *in vitro* data to show that at high concentrations macromolecules non-specifically enhance protein association rates or binding to surfaces. As a consequence, slow processes ('transition-state limited') are sped up, whereas fast one ('diffusion-limited') are slowed down. To precisely measure such phenomena *in vivo* remains a challenge but we expect more experimental data of protein diffusion, molecular association and enzyme activity in live cells, owing to fantastic developments in *in situ* labeling and optical microscopy.

Acknowledgements

We acknowledge financial support from SysMo via the BBSRC-funded KosmoBac programme coordinated by Ian R Booth (Aberdeen) and the Netherlands Science Foundation, NWO (Top-subsidy grant 700.56.302). We thank Adrian H. Elcock from the University of Iowa for providing us with Fig. 1.

References

Ashworth, J. M. & D. J. Watts, (1970) Metabolism of the cellular slime mould Dictyostelium discoideum grown in axenic culture. *Biochem J* **119**: 175-182.

Bacia, K., S. A. Kim & P. Schwille, (2006) Fluorescence cross-correlation spectroscopy in living cells. *Nat Methods* **3**: 83-89.

Biteen, J. S. & W. E. Moerner, (2010) Single-molecule and superresolution imaging in live bacteria cells. *Cold Spring Harb Perspect Biol* **2**: a000448.

Booth, I. R., M. D. Edwards, S. Black, U. Schumann & S. Miller, (2007) Mechanosensitive channels in bacteria: signs of closure? *Nat Rev Microbiol* **5**: 431-440.

Cayley, S., B. A. Lewis, H. J. Guttman & M. T. Record, Jr., (1991) Characterization of the cytoplasm of Escherichia coli K-12 as a function of external osmolarity. Implications for protein-DNA interactions *in vivo*. *J Mol Biol* **222**: 281-300.

Cluzel, P., M. Surette & S. Leibler, (2000) An ultrasensitive bacterial motor revealed by monitoring signaling proteins in single cells. *Science* **287**: 1652-1655.

Conlon, I. & M. Raff, (2003) Differences in the way a mammalian cell and yeast cells coordinate cell growth and cell-cycle progression. *J Biol* **2**: 7.

Cowan, A. E., E. M. Olivastro, D. E. Koppel, C. A. Loshon, B. Setlow & P. Setlow, (2004) Lipids in the inner membrane of dormant spores of Bacillus species are largely immobile. *Proc Natl Acad Sci U S A* **101**: 7733-7738.

Crane, J. M. & A. S. Verkman, (2008) Long-range nonanomalous diffusion of quantum dot-labeled aquaporin-1 water channels in the cell plasma membrane. *Biophys J* **94**: 702-713.

Dauty, E. & A. S. Verkman, (2004) Molecular crowding reduces to a similar extent the diffusion of small solutes and macromolecules: measurement by fluorescence correlation spectroscopy. *J Mol Recognit* **17**: 441-447.

Deich, J., E. M. Judd, H. H. McAdams & W. E. Moerner, (2004) Visualization of the movement of single histidine kinase molecules in live Caulobacter cells. *Proc Natl Acad Sci U S A* **101**: 15921-15926.

Derman, A. I., G. Lim-Fong & J. Pogliano, (2008) Intracellular mobility of plasmid DNA is limited by the ParA family of partitioning systems. *Mol Microbiol* **67**: 935-946.

Dinnbier, U., E. Limpinsel, R. Schmid & E. P. Bakker, (1988) Transient accumulation of potassium glutamate and its replacement by trehalose during adaptation of growing cells of Escherichia coli K-12 to elevated sodium chloride concentrations. *Arch Microbiol* **150**: 348-357.

Dix, J. A. & A. S. Verkman, (2008) Crowding effects on diffusion in solutions and cells. *Annu Rev Biophys* **37**: 247-263.

Dupuy, A. D. & D. M. Engelman, (2008) Protein area occupancy at the center of the red blood cell membrane. *Proc Natl Acad Sci U S A* **105**: 2848-2852.

Eckburg, P. B., E. M. Bik, C. N. Bernstein, E. Purdom, L. Dethlefsen, M. Sargent, S. R. Gill, K.

E. Nelson & D. A. Relman, (2005) Diversity of the human intestinal microbial flora. *Science* **308**: 1635-1638.

Elf, J., G. W. Li & X. S. Xie, (2007) Probing transcription factor dynamics at the single-molecule level in a living cell. *Science* **316**: 1191-1194.

Ellis, R. J., (2001) Macromolecular crowding: obvious but underappreciated. *Trends Biochem Sci* **26**: 597-604.

Elowitz, M. B., M. G. Surette, P. E. Wolf, J. B. Stock & S. Leibler, (1999) Protein mobility in the cytoplasm of Escherichia coli. *J Bacteriol* **181**: 197-203.

English, B. P., Sanamrad A.,Tankov S., Hauryliuk V. and Elf J, (2010) Tracking of individual freely diffusing fluorescent protein molecules in the bacterial cytoplasm. http://arxiv.org/ftp/arxiv/papers/1003/1003.2110.pdf

Ferguson, G. P., A. D. Chacko, C. H. Lee & I. R. Booth, (1996) The activity of the high-affinity K+ uptake system Kdp sensitizes cells of Escherichia coli to methylglyoxal. *J Bacteriol* **178**: 3957-3961.

Fukuoka, H., Y. Sowa, S. Kojima, A. Ishijima & M. Homma, (2007) Visualization of functional rotor proteins of the bacterial flagellar motor in the cell membrane. *J Mol Biol* **367**: 692-701.

Golding, I. & E. C. Cox, (2006) Physical nature of bacterial cytoplasm. *Phys Rev Lett* **96**: 098102.

Guigas, G. & M. Weiss, (2006) Size-dependent diffusion of membrane inclusions. *Biophys J* **91**: 2393-2398.

Harms, G. S., L. Cognet, P. H. Lommerse, G. A. Blab, H. Kahr, R. Gamsjager, H. P. Spaink, N. M. Soldatov, C. Romanin & T. Schmidt, (2001) Single-molecule imaging of l-type Ca(2+) channels in live cells. *Biophys J* **81**: 2639-2646.

Huang, B., M. Bates & X. Zhuang, (2009) Super-resolution fluorescence microscopy. *Annu Rev Biochem* **78**: 993-1016.

Kim, S. Y., Z. Gitai, A. Kinkhabwala, L. Shapiro & W. E. Moerner, (2006) Single molecules of the bacterial actin MreB undergo directed treadmilling motion in Caulobacter crescentus. *Proc Natl Acad Sci U S A* **103**: 10929-10934.

Kleckner, N., (2010) Mesoscale spatial patterning in the Escherichia coli Min system: reaction-diffusion versus mechanical communication. *Proc Natl Acad Sci U S A* **107**: 8053-8054.

Konopka, M. C., I. A. Shkel, S. Cayley, M. T. Record & J. C. Weisshaar, (2006) Crowding and confinement effects on protein diffusion *in vivo*. *J Bacteriol* **188**: 6115-6123.

Konopka, M. C., Sochacki, K. A., Bratton, B. P., Shkel, I. A., Record, M. T., Weisshaar, J. C., (2009) Cytoplasmic protein mobility in osmotically stressed Escherichia coli. *J Bacteriol* **191**: 231-237.

Konopka, M. C., J. C. Weisshaar & M. T. Record, Jr., (2007) Methods of changing biopolymer volume fraction and cytoplasmic solute concentrations for *in vivo* biophysical studies. *Methods Enzymol* **428**: 487-504.

Kumar, M., M. S. Mommer & V. Sourjik, (2010) Mobility of cytoplasmic, membrane, and DNA-binding proteins in Escherichia coli. *Biophys J* **98**: 552-559.

Leake, M. C., J. H. Chandler, G. H. Wadhams, F. Bai, R. M. Berry & J. P. Armitage, (2006) Stoichiometry and turnover in single, functioning membrane protein complexes. *Nature* **443**: 355-358.

Leake, M. C., N. P. Greene, R. M. Godun, T. Granjon, G. Buchanan, S. Chen, R. M. Berry, T. Palmer & B. C. Berks, (2008) Variable stoichiometry of the TatA component of the twin-arginine protein transport system observed by *in vivo* single-molecule imaging. *Proc Natl Acad Sci U S A* **105**: 15376-15381.

Lenn, T., M. C. Leake & C. W. Mullineaux, (2008) Clustering and dynamics of cytochrome bd-I complexes in the Escherichia coli plasma membrane *in vivo*. *Mol Microbiol* **70**: 1397-1407.

Llopis, P. M., A. F. Jackson, O. Sliusarenko, I. Surovtsev, J. Heinritz, T. Emonet & C. Jacobs-Wagner, (2010) Spatial organization of the flow of genetic information in bacteria. *Nature* **466**: 77-81.

McGuffee, S. R. & A. H. Elcock, (2010) Diffusion, crowding & protein stability in a dynamic molecular model of the bacterial cytoplasm. *PLoS Comput Biol* **6**: e1000694.

Mika, J. T., G. van den Bogaart, L. Veenhoff, V. Krasnikov & B. Poolman, (2010) Molecular sieving properties of the cytoplasm of Escherichia coli and consequences of osmotic stress. *Mol Microbiol* **77**: 200-207.

Mullineaux, C. W., A. Nenninger, N. Ray & C. Robinson, (2006) Diffusion of green fluorescent protein in three cell environments in Escherichia coli. *J Bacteriol* **188**: 3442-3448.

Nenninger, A., G. Mastroianni & C. W. Mullineaux, (2010) Size-dependence of protein diffusion in the cytoplasm of Escherichia coli. *J Bacteriol* **192**: 4535-4540.

Niu, L. & J. Yu, (2008) Investigating intracellular dynamics of FtsZ cytoskeleton with photoactivation single-molecule tracking. *Biophys J* **95**: 2009-2016.

Potma, E. O., W. P. de Boeij, L. Bosgraaf, J. Roelofs, P. J. van Haastert & D. A. Wiersma, (2001) Reduced protein diffusion rate by cytoskeleton in vegetative and polarized dictyostelium cells. *Biophys J* **81**: 2010-2019.

Ramadurai, S., A. Holt, V. Krasnikov, G. van den Bogaart, J. A. Killian & B. Poolman, (2009) Lateral diffusion of membrane proteins. J Am Chem Soc **131**: 12650-12656.

Ramadurai, S., Duurkens R., Krasnikov VV, and Poolman B. , (2010a) Lateral diffusion of membrane proteins: consequences of hydrophobic mismatch and lipid composition. *Biophysical J* **99**: 1482-1489.

Ramadurai, S., Holt A, Schäfer LV, Krasnikov VV,Rijkers DTS,Marrink SJ, Killian AJ and Poolman B, (2010b) Influence of Hydrophobic Mismatch and Amino Acid Composition on the Lateral Diffusion of Transmembrane Peptide.*Biophysical J* **99**: 1447-1457.

Romantsov, T., A. R. Battle, J. L. Hendel, B. Martinac & J. M. Wood, (2010) Protein localization in Escherichia coli cells: comparison of the cytoplasmic membrane proteins ProP, LacY, ProW, AqpZ, MscS, and MscL. *J Bacteriol* **192**: 912-924.

Saffman, P. G. & M. Delbruck, (1975) Brownian motion in biological membranes. *Proc Natl Acad Sci U S A* **72**: 3111-3113.

Schulmeister, S., M. Ruttorf, S. Thiem, D. Kentner, D. Lebiedz & V. Sourjik, (2008) Protein exchange dynamics at chemoreceptor clusters in Escherichia coli. *Proc Natl Acad Sci U S A* **105**: 6403-6408.

Seksek, O., J. Biwersi & A. S. Verkman, (1997) Translational diffusion of macromolecule-sized solutes in cytoplasm and nucleus. *J Cell Biol* **138**: 131-142.

Slade, K. M., R. Baker, M. Chua, N. L. Thompson & G. J. Pielak, (2009a) Effects of recombinant protein expression on green fluorescent protein diffusion in Escherichia coli. *Biochemistry* **48**: 5083-5089.

Slade, K. M., B. L. Steele, G. J. Pielak & N. L. Thompson, (2009b) Quantifying green fluorescent protein diffusion in Escherichia coli by using continuous photobleaching with evanescent illumination. *J Phys Chem B* **113**: 4837-4845.

Sourjik, V. & J. P. Armitage, (2010) Spatial organization in bacterial chemotaxis. *EMBO J* **29**: 2724-2733.

Spitzer, J. J. & B. Poolman, (2005) Electrochemical structure of the crowded cytoplasm. *Trends Biochem Sci* **30**: 536-541.

Swaminathan, R., C. P. Hoang & A. S. Verkman, (1997) Photobleaching recovery and anisotropy decay of green fluorescent protein GFP-S65T in solution and cells: cytoplasmic viscosity probed by green fluorescent protein translational and rotational diffusion. *Biophys J* **72**: 1900-1907.

van den Bogaart, G., N. Hermans, V. Krasnikov & B. Poolman, (2007) Protein mobility and diffusive barriers in Escherichia coli: consequences of osmotic stress. *Mol Microbiol* **64**: 858-871.

Vendeville, A., D. Lariviere & E. Fourmentin, (2011) An inventory of the bacterial macromolecular components and their spatial organization. *FEMS Microbiol Rev* **35**: 395-414.

Verkman, A. S., (2002) Solute and macromolecule diffusion in cellular aqueous compartments. *Trends Biochem Sci* **27**: 27-33.

Winick, M., (1968) Changes in nucleic acid and protein content of the human brain during growth. *Pediatr Res* **2**: 352-355.

Wood, J. M., (1999) Osmosensing by bacteria: signals and membrane-based sensors. *Microbiol Mol Biol Rev* **63**: 230-262.

Wood, J. M., (2011) Bacterial Osmoregulation: A Paradigm for the Study of Cellular Homeostasis. *Annu Rev Microbiol*.

Wood, J. M., E. Bremer, L. N. Csonka, R. Kraemer, B. Poolman, T. van der Heide & L. T. Smith, (2001) Osmosensing and osmoregulatory compatible solute accumulation by bacteria. *Comp Biochem Physiol A Mol Integr Physiol* **130**: 437-460.

Xie, X. S., P. J. Choi, G. W. Li, N. K. Lee & G. Lia, (2008) Single-molecule approach to molecular biology in living bacterial cells. *Annu Rev Biophys* **37**: 417-444.

Zhou, H. X., G. Rivas & A. P. Minton, (2008) Macromolecular crowding and confinement: biochemical, biophysical, and potential physiological consequences. *Annu Rev Biophys* **37**: 375-397.

Zimmerman, S. B. & S. O. Trach, (1991) Estimation of macromolecule concentrations and excluded volume effects for the cytoplasm of Escherichia coli. *J Mol Biol* **222**: 599-620.

Zinser, E., C. D. Sperka-Gottlieb, E. V. Fasch, S. D. Kohlwein, F. Paltauf & G. Daum, (1991) Phospholipid synthesis and lipid composition of subcellular membranes in the unicellular eukaryote Saccharomyces cerevisiae. *J Bacteriol* **173**: 2026-2034.

CHAPTER 3

EVALUATION OF PULSED-FRAP AND CONVENTIONAL-FRAP FOR DETERMINATION OF PROTEIN MOBILITY IN PROKARYOTIC CELLS

Jacek T. Mika, Victor Krasnikov, Geert van den Bogaart, Foppe de Haan & Bert Poolman

PloS One 2011, **6**: e25664

Macromolecule mobility is often quantified with Fluorescence Recovery After Photobleaching (FRAP). Throughout literature a wide range of diffusion coefficients for GFP in the cytoplasm of *Escherichia coli* (3 to 14 μm^2/s) is reported using FRAP-based approaches. In this study, we have evaluated two of these methods: pulsed-FRAP and "conventional"-FRAP. To address the question whether the apparent discrepancy in the diffusion data stems from methodological differences or biological variation, we have implemented and compared the two techniques on bacteria grown and handled in the same way. The GFP diffusion coefficients obtained under normal osmotic conditions and upon osmotic upshift were very similar for the different techniques. Our analyses indicate that the wide range of values reported for the diffusion coefficient of GFP in live cells are due to experimental conditions and/or biological variation rather than methodological differences.

Introduction

In 1999 Elowitz and co workers (Elowitz *et al.*, 1999) published a pioneering study on the mobility of proteins inside live *E. coli* cells, using Fluorescence Recovery After Photobleaching (FRAP). Although FRAP has been a well established tool for studying macromolecule mobility inside living cells since the 1970's (Axelrod *et al.*, 1976), the attempts to use FRAP in bacteria have proven to be difficult mainly due to their small size. For example an *E.coli* cell is typically 1 x 3 µm, while human fibroblasts can easily reach dimensions over 100 µm. This property renders bacterial cells difficult to study as their dimension are only a few times larger than the diffraction limit of optical microscopy. Moreover, traditional FRAP protocols include a relatively large photo-bleaching spot and high laser intensity, both of which are not amenable for the small volume of bacteria.

Elowitz *et al.* (Elowitz *et al.*, 1999) have modified the FRAP protocol by using a smaller bleaching spot and weaker laser power, so that sufficient non-photobleached GFP is left to measure fluorescence recovery. This approach has been successful implemented by others (Nenninger *et al.*, 2010, Kumar *et al.*, 2010, Konopka *et al.*, 2009, Konopka *et al.*, 2006). Subsequently, other methods have been tailored to probe macromolecule diffusion in bacteria, including FRAP related techniques like pulsed–FRAP (van den Bogaart *et al.*, 2007) and continuous photobleaching, using total internal reflection microscopy (Slade *et al.*, 2009a, Slade *et al.*, 2009b), single-molecule tracking (English *et al.*, 2010) and fluorescence correlation spectroscopy (Cluzel *et al.*, 2000). For an overview of those techniques, we refer to Mika and Poolman (Mika & Poolman, 2011).

There are now several studies that report the mobility of GFP and related proteins like YFP and mEos2, yielding diffusion coefficients for these proteins in the *E.coli* cytoplasm that range from 3 $\mu m^2/s$ (Mika *et al.*, 2010, van den Bogaart *et al.*, 2007) through 6-7 $\mu m^2/s$ (Konopka *et al.*, 2006, Elowitz *et al.*, 1999) up to 14 $\mu m^2/s$ (Konopka, 2009, English, 2010). The question arises whether this relatively wide range of values reflects differences in the methods used or biological and/or experimental variations?

We have now compared 'conventional FRAP' as initially used by Elowitz

(Elowitz *et al.*, 1999) and pulsed-FRAP, developed in our laboratory (van den Bogaart *et al.*, 2007), to determine the diffusion of GFP in *E. coli* under well-defined conditions. We demonstrate that both techniques yield very similar distributions of diffusion coefficients of GFP in the cytoplasm under normal and osmotic stress conditions. We conclude that the different *D* values reported for GFP(-like) proteins in the literature (Elowitz *et al.*, 1999, Mika *et al.*, 2010, van den Bogaart *et al.*, 2007, Konopka, 2009, Konopka *et al.*, 2006, Mullineaux *et al.*, 2006, English *et al.*, 2010) are a result of different handling of the cells and true biological variations rather than differences in the FRAP methods used.

Materials and Methods

Strains, growth and preparation of bacterial cells for microscopy

Escherichia coli K-12 strain MG1655 harboring pGFPCR, that encodes the GFP cycle 3 variant which is derived from GFPuv (Clonetech), (van den Bogaart *et al.*, 2007) was grown as described previously (Mika *et al.*, 2010). Briefly, the cells were grown from single colonies in Luria Broth (10 g/L Bacto Tryptone (Becton Dickinson), 5 g/L Yeast extract (Becton Dickinson) plus 10 g/L NaCl (Merck)) supplemented with 100 µg/mL ampicillin (Sigma) at 37 ^{O}C with vigorous shaking until the culture had reached an OD_{600} of 0.3–0.4. Leaky expression of GFP from the pGFPCR plasmid was sufficiently high to allow measurements and thus no inducer was added to the medium. Prior to the microscopy, the cells were washed twice with the NaPGCl medium (NaPGCl = 95 mM sodium phosphate, pH 7.0, 50 mM glucose plus 125 mM sodium chloride), which has an osmolality equal to that of LB (ΔLBOsm = 0) and very low fluorescence. For measurements the cells were either kept in NaPGCl or osmotically upshifted by supplementing the medium with additional NaCl. The osmolality of all solutions was measured by determination of their freezing point (Osmomat 030, Gonotec). For microscopy, 2 µl of cells was placed on poly-L-lysine (1% w/v) coated cover slips and measurements were carried out immediately. Each sample was imaged for periods no longer than 25 min. For each osmotic condition, a minimum of 20 single cells was analyzed. All measurements were performed at 20 +/- 1°C.

Measurements of diffusion coefficients

Pulsed-FRAP measurements were carried out on a confocal microscope as described by van den Bogaart *et al.* (van den Bogaart *et al.*, 2007). Briefly, cells were first imaged with a confocal microscope and a low-intensity, diffraction-limited laser beam was positioned in the middle of the cell. Subsequently, this laser beam was modulated using a shutter to apply short pulses, separated by time intervals without illumination to allow the fluorescence to recover. The fluorescent signal recorded during the pulses is influenced by the photobleaching of the GFP in the focal spot (decrease of fluorescence intensity) and by diffusion of the non-photobleached fluorophore into the focal spot (increase of fluorescence intensity). The fluorescence is linearly proportional to the concentration of GFP. The measured traces can be analysed using the Fick's second law where the GFP concentration fluctuations inside the cell *C(r, t):*

$$\frac{\partial C(r,t)}{\partial t} = D\Delta C(r,t) \ ,$$

where *C* is the concentration of GFP, Δ is the Laplace operator. and *r* and *t* define the position and time point, respectively. We assume that the photo-bleaching rate is proportional to the intensity of the focused laser beam *I(r)* and thus obtain a bleaching constant *B*:

$$\frac{\partial C(r,t)}{\partial t} = BI(r)C(r,t)\cdot$$

Finally, to obtain a diffusion coefficient (*D*), the traces are fitted numerically to a 2D diffusion model as described in detail by van den Bogaart *et al.* (van den Bogaart *et al.*, 2007).

"Conventional FRAP" measurements were performed using an inverted microscope Observer D1 (Carl Zeiss, Jena, Germany) equipped with a Zeiss C-Apochromat infinity-corrected 1.2 NA 63× water immersion objective and a motorized X-Y translating stage for fine positioning of the cells. The optical part of the set-up is depicted in Fig. 1 and is very similar to the one reported by Konopka and co-workers (Konopka *et al.*, 2006). The laser beam (488 nm, argon ion laser, Melles Griot, Carlsbad, CA, USA) was split into two beams. The first beam was focused to a diameter of around 1 µm and was used for photobleaching. The second beam (‘wide’) had a diameter of around 100 mm in the image plane and was employed to monitor the fluorescence recovery.

The fluorescence emission was collected through the same objective and separated from the excitation beam by a dichroic mirror (Chroma Technology, Rockingham, VT, USA) and further directed through a 488 nm notch filter (CVI, Melles Griot, Carlsbad, CA, USA). The fluorescence signal was collected by a Cool-Snap HQ2 CCD camera (Photometrics, Tucson, AZ, USA).

The cells were measured as described by Elowitz (Elowitz *et al.*, 1999) and Konopka (Konopka *et al.*, 2006). To position the desired bacterium in the focal plane of the microscope and in the bleaching area, bright-field transmittance microscopy mode was used. A fluorescence microscopy image of the cell before photobleaching was recorded (Fig. 2A). Subsequently, an area at the pole of the bacterium was photobleached (Fig. 2B) with a short (100 ms) focused light pulse. Immediately afterwards, typically 40 images of the recovery of fluorescence were collected, using fluorescence illumination with the ‘wide’ beam. The frame rate to monitor the fluorescence recovery was adjusted to the speed of diffusion, i.e. every 25-50 ms for fast diffusion (normal osmotic conditions) and every 250 ms for severe osmotic upshift conditions. The analysis is described by Kumar *et al.* (Kumar *et al.*, 2010). The images, recorded during the recovery phase, were analyzed numerically, using home written software as schematically depicted in Fig. 2G-J. A line was drawn through the longest axis of the bacterium and fluorescence intensity distributions along this cross-section (X-axis) were extracted from the image (Fig. 2B-J). To take into account intrinsic inhomogeneity of the fluorescence intensity along the X-axis, the ‘pre-photobleached’ distribution (Fig. 2F) was used to normalize all measured distributions. To obtain a diffusion coefficient, the software simulated the normalized fluorescence intensity distributions along the given cross-section during recovery (Fig. 2G-J). Following Elowitz (Elowitz *et al.*, 1999), the one–dimensional diffusion approximation was assumed:

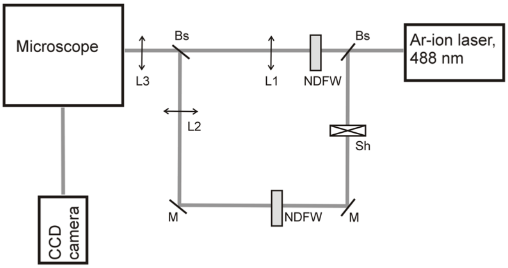

Figure 1. Optical scheme of the set-up used to perform conventional FRAP. Bs, beam splitter; M, mirror; NDFW, neutral density filter wheel; L1, L2, L3 lenses; Sh,shutter.

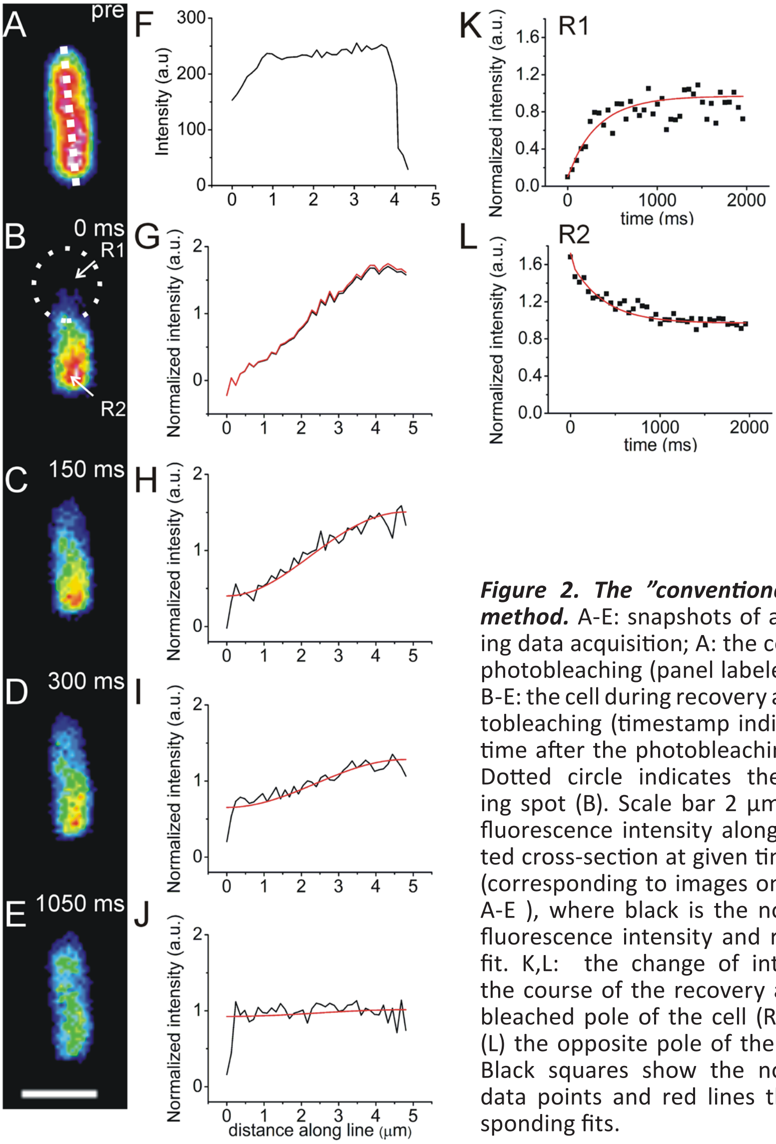

Figure 2. The "conventional FRAP" method. A-E: snapshots of a cell during data acquisition; A: the cell before photobleaching (panel labeled "pre"); B-E: the cell during recovery after photobleaching (timestamp indicates the time after the photobleaching pulse). Dotted circle indicates the bleaching spot (B). Scale bar 2 µm. F-J: the fluorescence intensity along the dotted cross-section at given time points (corresponding to images on the left: A-E), where black is the normalized fluorescence intensity and red is the fit. K,L: the change of intensity in the course of the recovery at (K) the bleached pole of the cell (R1) and at (L) the opposite pole of the cell (R2). Black squares show the normalized data points and red lines the corresponding fits.

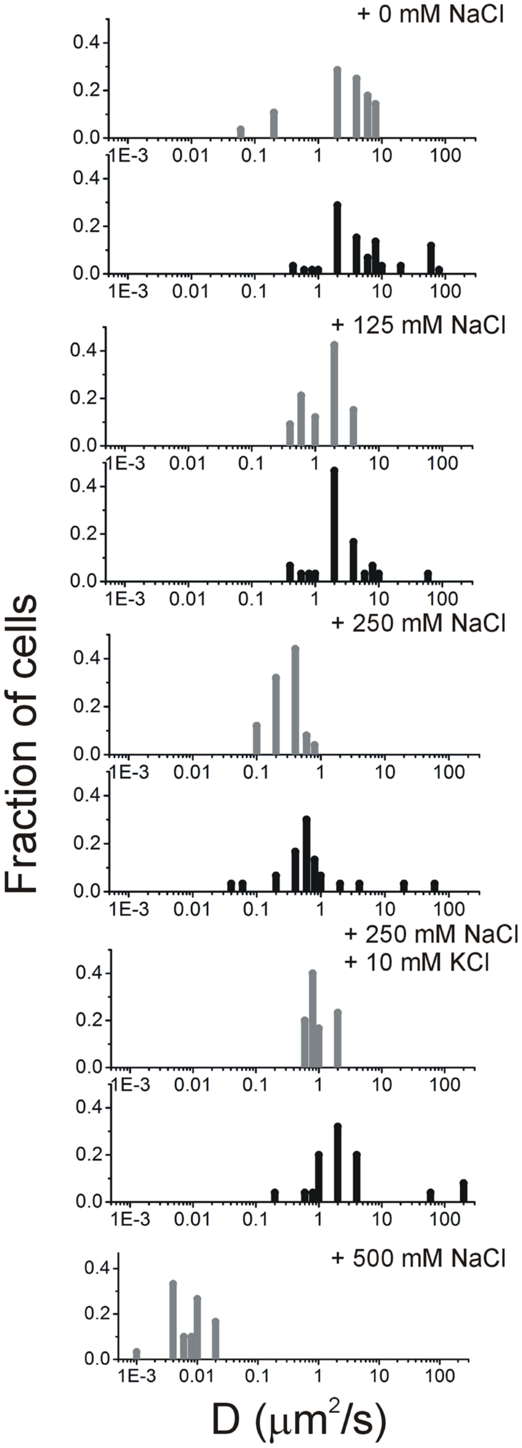

Figure 3. Comparison of pulsed-FRAP with "conventional FRAP". Diffusion coefficients of GFP in the cytoplasm of *E. coli* measured with "conventional FRAP" (gray bars) and pulsed-FRAP (black bars) under normal osmotic conditions (top panel, "+ 0mM NaCl") and under conditions of osmotic upshift (lower panels, the extent of osmotic shock is indicated in the upper right corner of each panel). For the highest osmotic stress (lowest panel, "+ 500 mM NaCl") only "conventional FRAP" data are presented. The number of cells measured in each experiment was at least 20.

$$\frac{\partial I(x,t)}{\partial t} = D\frac{\partial^2 I(x,t)}{\partial x^2} \ ,$$

where I is fluorescence intensity and D is the diffusion coefficient; with boundary conditions:

$$\frac{\partial I(x,t)}{\partial x} = 0$$

at the bacterial poles, corresponding to zero flux of GFP through the cell membrane. For final renormalization the distribution of GFP prior to photobleaching (Fig. 2F) was used. For the cell shown in Fig. 2, we obtained a diffusion coefficient of 6 µm^2/s.

To illustrate the evolution of the fluorescence recovery, 'single-spot' fluorescence traces at positions R1 and R2 are depicted in Fig. 2K-L. using the classical approach introduced by Axelrod (Axelrod *et al.*, 1976):, these fluorescent traces (Fig. 2K-L), yielded a diffusion coefficient D of 1.5 µm^2/s, assuming a beam diameter of 1 µm.

For each experimental condition, at least 20 individual cells were analyzed. The obtained diffusion coefficient values were plotted as histograms.

Results and discussion

Pulsed FRAP and "conventional FRAP" yield similar diffusion coefficients

Figure 3 presents histograms of distributions of diffusion coefficients of cytoplasmic GFP at different osmotic regimes. To ease the visual comparison of the two methods, the corresponding data from pulsed-FRAP (black) and "conventional FRAP" (gray) have been plotted below each other. We note that for pulsed-FRAP measurements of very low molecule mobility are difficult to probe. Pulsed-FRAP requires that the time between photobleach light-pulses is long enough for complete recovery of the GFP in the cell. In severely stressed cells (500 mM NaCl or more) diffusion is very slow and the recovery is not homogenous. In fact, as reported previously above 500 mM of NaCl (van den Bogaart *et al.*, 2007) one observes apparent barriers for diffusion. For these so-called plasmolyzing cells, pulsed-FRAP is not suitable to obtain quantitative information on protein mobility.

In general both pulsed- and "conventional-FRAP" give quite broad distributions of diffusion coefficients, which has been also observed by others (van den Bogaart *et al.*, 2007, Konopka *et al.*, 2006, Elowitz *et al.*, 1999), not only for GFP but also for other macromolecules (Mika *et al.*, 2010). The wide range of distributions is in part due to errors in the measurements and data analysis, but a large part is due to population heterogeneity. Pulsed-FRAP yields somewhat broader distributions of diffusion coefficients, which might be a result of the changes of the cell position in respect to the focal volume during the measurement.

Despite the difference in the methodologies, both techniques yield similar maxima in the distributions of values and the decrease in diffusion of GFP is proportional to the strength of the osmotic shock applied. Moreover, the diffusion coefficients of osmotically stressed cells increase in the presence of osmoprotectants (Fig.3 panel "+250 mMNaCl+10 mM KCl").

Differences between methods

From a practical point of view "conventional FRAP" may be more suited to probe protein mobility in live cells than pulsed-FRAP. With "conventional FRAP" snapshots of the whole cell are recorded, which gives information about the distribution of the GFP inside the cytoplasm (i.e., whether it is homo- or heterogenous) and it can be easily observed if the cell moves during the measurement. In case of pulsed-FRAP the movement of cell cannot be observed until the end of the series of bleaching pulses, which could hamper data acquisition. Moreover, the data analysis on average takes only a few minutes with "conventional FRAP", while it can take up to hours to calculate a diffusion coefficient with pulsed-FRAP.

On the other hand pulsed–FRAP maybe better suited for smaller cells or organelles. Pulsed-FRAP also proved suitable for measuring the mobility of very fast diffusing NBD-glucose, which has a poor photostability (Mika *et al.*, 2010).

This measurement would be technically challenging to perform with "conventional FRAP". The cell length of *E.coli* is typically 3 µm. The average diffusion coefficient of NBD-glucose in the cytoplasm of *E.coli* under normal osmotic condition is close to 50 µm^2/s, which means that after photobleaching the fluorescence can fully recover within less than 30 ms. Since this dye is not very bright and quite photolabile, fast CCD imaging is insufficient to capture good quality FRAP data.

Why are the reported diffusion constants different?

In the recent literature, the diffusion coefficients for GFP in the *E.coli* cytoplasm, grown and analyzed under normal osmotic conditions, ranged from 3 to 14 µm^2/s. This variation may be partly due to the methods of extracting the representative average values. Some authors take the arithmetic average (van den Bogaart *et al.*, 2007, Konopka *et al.*, 2006, Slade *et al.*, 2009a). Upon visual inspection of the data obtained for *E.coli* (Fig. 3), it is apparent that the median value may actually be a better approximation of the 'average' diffusion coefficient. This approach has been implemented in later studies (Konopka, 2009, Mika *et al.*, 2010).

Another possible reason for the differences in the diffusion coefficients is the composition of the growth media. It can be observed that cells grown in rich media like LB show lower mobility of proteins (Mika *et al.*, 2010, van den Bogaart *et al.*, 2007, Konopka *et al.*, 2006) than cells grown in minimal media (Konopka, 2009). Particularly striking are the values reported by the group of Weisshaar (Konopka, 2009, Konopka *et al.*, 2006). Using "conventional FRAP", they report diffusion coefficient for GFP (Konopka *et al.*, 2006) of 6 - 7 µm^2/s for LB grown cells, whereas cells grown in a minimal MOPS-based medium showed values of 14 µm^2/s (Konopka, 2009). Moreover, they reported that the culture's history has a major impact on the mobility of GFP diffusion (Konopka, 2009). Cells adapted to high osmolality of growth tend to display a lower decrease in diffusion coefficients upon exposure to osmotic upshift than cells grown in media of normal osmolality.

The observation that in bacteria grown in rich media the diffusion of macromolecules is slower than in bacteria grown in minimal medium may have a plausible biological rationale. Bacteria grown in rich media divide more often and synthesize more mRNA (Vogel & Jensen, 1994) and have a higher number of ribosomes (Dennis & Bremer, 1974) as compared to bacteria growing and dividing more slowly in minimal medium. In this context the overall macromolecular crowding (often thought to be the main cause for slower diffusion in the cytoplasm as compared to dilute aqueous solutions) may be rather constant, however, the nature of the crowding agent would change. It is tempting to speculate that in the cytoplasm of bacteria grown on rich media the diffusion is slower due to a higher abundance of ribosomes that are bulkier crowders (11.4 nm radius, (Konopka, 2009)) than average cytoplasmatic proteins (2-3nm diameter). Moreover, the increased content of mRNA, which forms long unfolded chains, may additionally hinder macromolecule diffusion. The hypothesis that not only the cytoplasm crowding itself, but also the nature of the crowders contributes to slowed diffusion remains yet to be proven experimentally.

Conclusions

We have shown that, under a variety of osmotic conditions, pulsed-FRAP and “conventional-FRAP” yield very similar diffusion coefficients of GFP in the cytoplasm of *E.coli*. We speculate that the different values reported in the literature are due to variations in the constitution of the cells, *i.e.*, as determined by their growth media and history.

References

Axelrod, D., D. E. Koppel, J. Schlessinger, E. Elson & W. W. Webb, (1976) Mobility measurement by analysis of fluorescence photobleaching recovery kinetics. *Biophys J* **16**: 1055-1069.

Cluzel, P., M. Surette & S. Leibler, (2000) An ultrasensitive bacterial motor revealed by monitoring signaling proteins in single cells. *Science* **287**: 1652-1655.

Dennis, P. P. & H. Bremer, (1974) Macromolecular composition during steady-state growth of Escherichia coli B-r. *J Bacteriol* **119**: 270-281.

Elowitz, M. B., M. G. Surette, P. E. Wolf, J. B. Stock & S. Leibler, (1999) Protein mobility in the cytoplasm of Escherichia coli. *J Bacteriol* **181**: 197-203.

English, B. P., Sanamrad A.,Tankov S., Hauryliuk V. and Elf J, (2010) Tracking of individual freely diffusing fluorescent protein molecules in the bacterial cytoplasm. http://arxiv.org/ftp/arxiv/papers/1003/1003.2110.pdf

Konopka, M. C., I. A. Shkel, S. Cayley, M. T. Record & J. C. Weisshaar, (2006) Crowding and confinement effects on protein diffusion *in vivo*. *J Bacteriol* **188**: 6115-6123.

Konopka, M. C., Sochacki, K. A., Bratton, B. P., Shkel, I. A., Record, M. T., Weisshaar, J. C., (2009) Cytoplasmic protein mobility in osmotically stressed Escherichia coli. *J Bacteriol* **191**: 231-237.

Kumar, M., M. S. Mommer & V. Sourjik, (2010) Mobility of cytoplasmic, membrane, and DNA-binding proteins in Escherichia coli. *Biophys J* **98**: 552-559.

Mika, J. T. & B. Poolman, (2011) Macromolecule diffusion and confinement in prokaryotic cells. *Curr Opin Biotechnol* **22**: 117-126.

Mika, J. T., G. van den Bogaart, L. Veenhoff, V. Krasnikov & B. Poolman, (2010) Molecular sieving properties of the cytoplasm of Escherichia coli and consequences of osmotic stress. *Mol Microbiol* **77**: 200-207.

Mullineaux, C. W., A. Nenninger, N. Ray & C. Robinson, (2006) Diffusion of green fluorescent protein in three cell environments in Escherichia coli. *J Bacteriol* **188**: 3442-3448.

Nenninger, A., G. Mastroianni & C. W. Mullineaux, (2010) Size-dependence of protein diffusion in the cytoplasm of Escherichia coli. *J Bacteriol* **192**: 4535-4540.

Slade, K. M., R. Baker, M. Chua, N. L. Thompson & G. J. Pielak, (2009a) Effects of recombinant protein expression on green fluorescent protein diffusion in Escherichia coli. *Biochemistry* **48**: 5083-5089.

Slade, K. M., B. L. Steele, G. J. Pielak & N. L. Thompson, (2009b) Quantifying green fluorescent protein diffusion in Escherichia coli by using continuous photobleaching with evanescent illumination. *J Phys Chem B* **113**: 4837-4845.

van den Bogaart, G., N. Hermans, V. Krasnikov & B. Poolman, (2007) Protein mobility and diffusive barriers in Escherichia coli: consequences of osmotic stress. *Mol Microbiol*

64: 858-871.

Vogel, U. & K. F. Jensen, (1994) The RNA chain elongation rate in Escherichia coli depends on the growth rate. *J Bacteriol* **176**: 2807-2813.

CHAPTER 4

MOLECULAR SIEVING PROPERTIES OF THE CYTOPLASM OF *E.COLI* AND CONSEQUENCES OF OSMOTIC STRESS

Jacek T. Mika, Geert van den Bogaart, Liesbeth Veenhoff, Victor Krasnikov
& Bert Poolman

Molecular Microbiology 2010, **77**: 200-2007

We determined the diffusion coefficients (*D*) of (macro)molecules of different sizes (from ~0.5 to 600 kDa) in the cytoplasm of live *Escherichia coli* cells under normal osmotic conditions and osmotic upshift. *D* values decreased with increasing molecular weight of the molecules. Upon osmotic upshift, the decrease in *D* of NBD-glucose was much smaller than that of macromolecules. Barriers for diffusion were found in osmotically-challenged cells only for GFP and larger proteins. These barriers are likely formed by the nucleoid and crowding of the cytoplasm. The cytoplasm of *E. coli* appears as a meshwork allowing the free passage of small molecules while restricting the diffusion of bigger ones.

Introduction

The cytoplasm of both eukaryotic and prokaryotic cells is a crowded environment with macromolecule concentrations as high as 200-300 g/l for *E. coli* (Ellis, 2001, Cayley & Record, 2004). In such an environment the diffusion of particles is slower than in water. Increased crowding favors the association of (macro)molecules inside living cells and thus increases reaction rates (Batra *et al.*, 2009, Ellis, 2001). The crowding also slows diffusion of molecules which will decrease reaction rates that are limited by diffusion. Because many biological reactions are often characterized *in vitro* at very low concentrations (hardly ever exceeding 10 g/l and typically three orders of magnitude lower), this may not reveal the reaction conditions present inside living cells (Ellis, 2001). It is thus important to have quantitative information on the equilibria of molecule associations, as well as the diffusion of low and high molecular weight molecules in the cytoplasm of live cells.

The measurements of diffusion in live bacteria by Fluorescence Recovery After Photobleaching (FRAP)-based approaches are technically challenging due to the small size of the cells, which is only a few times bigger than the resolution of conventional light microscopy. Up to now there are few studies that address the mobility of macromolecules in bacterial cells (Elowitz *et al.*, 1999, Konopka *et al.*, 2006, Konopka *et al.*, 2009, Kumar *et al.*, 2010, van den Bogaart *et al.*, 2007, Mullineaux *et al.*, 2006, Slade *et al.*, 2009a, Slade *et al.*, 2009b). For GFP in the cytoplasm of *E. coli*, the diffusion coefficients are reported to be in the range of 3 to 10 $\mu m^2/s$, which compares to a value of about 90 $\mu m^2/s$ in non-crowded, aqueous solution (Potma *et al.*, 2001).

Upon osmotic upshift *E. coli* cells instantaneously lose cytoplasmic water and eventually plasmolyze (Booth *et al.*, 2007, Wood, 1999). The loss of water results in a decrease of volume of the cytoplasm and an increase of (macro)molecule crowding, which may increase from 200-300 g/l to 400 g/l (Cayley *et al.*, 1991). This increased crowding translates to slowed diffusion in the cytoplasm (Konopka *et al.*, 2006, Konopka *et al.*, 2009, van den Bogaart *et al.*, 2007).

To the best of our knowledge the mobility of small molecules (less than 1 kDa) in the cytoplasm of live microbial cells has not been determined before. Also, it is not known to what extent an increased crowding as a result of osmotic stress influences the mobility of small versus big molecules. In this study, we investigate the consequences of osmotic stress by measuring the diffusion of (macro) molecules of different size. We observe that in osmotically-stressed cells, both the nucleoid as well as the high crowding cause barriers for mobility. Most striking is that even at the highest osmotic upshifts (media supplemented with 2 M NaCl) small molecules of the size of metabolites remain fairly mobile and there are no apparent barriers limiting their diffusion. We discuss these findings in the light of our understanding of how bacteria recover from osmotic stress.

Materials and methods

Strains, growth and expression of fluorescent proteins

Escherichia coli K-12 strain MG1655 (Genotype: F$^-$ lambda$^-$ *ilvG*$^-$ *rfb*-50 *rph*-1 Serotype: OR:H48:K-) was grown at 37° C with vigorous shaking in Luria Broth (LB) medium [LB is 10 g/L Bacto Tryptone (Becton Dickinson), 5 g/L Yeast extract (Becton Dickinson) plus 10 g/L NaCl (Merck)]. Where necessary the medium was supplemented with 100 µg/ml ampicillin (Sigma). For the expression of fluorescent proteins, the cells were transformed with the following plasmids: pGFPCR (GFP, (van den Bogaart *et al.*, 2007), pBADmPlum (Wang *et al.*, 2004), pBAD-β-Gal-GFP (this work; yielding the β-galactosidase-gfp fusion protein) and LacY-GFP (Geertsma *et al.*, 2008). Before the measurement a single colony was picked from a LB agar plate and a 4 ml culture was inoculated and grown to log phase (OD_{600} = 0.3-0.4). The cultures were maintained in the exponential phase of growth by re-inoculation with fresh LB. Leaky expression of GFP from the pGFPCR plasmid was sufficiently high to allow measurements without inducing the cells. All other proteins were expressed from the arabinose promoter by supplementing the medium with 0.02% (w/v), 0.002% and 0.0002% L-arabinose (Sigma) for mPlum, LacY-GFP and (β-gal-gfp)$_4$, respectively. The expression of (β-gal-gfp)$_4$ and LacY-GFP was carried out at 30°C. The proteins were expressed and folded prior to the osmotic upshifts and microscopy measurements; as

GFP is extremely stable the observed cellular fluorescence is due to the distribution of the protein rather than changes in its integrity.

Preparation of the samples for microscopy

Once the *E. coli* culture had reached an OD_{600} = 0.3 - 0.4, 1 ml of cells was taken and washed 2 times with NaPGCl medium (NaPGCl = 95 mM sodium phosphate, pH 7.0, 50 mM glucose plus 125 mM sodium chloride) which has an osmolality equal to that of LB ($\Delta LB_{Osm} = 0$). For loading of the cells with NBD-glucose (Invitrogen), the glucose present in the medium was replaced with NaCl. The cells were then pelleted and resuspended in 50 µl of the same buffer. 2 µl of 10 mM NBD-glucose or 2.5 µl of 50 µM Draq-5 (Biostatus Limited) were added and the cells were labeled at 37^{o}C with vigorous shaking for 20 minutes. After the labeling the cells were prepared for microscopy immediately. For measurements the cells were either kept in NaPGCl or osmotically-upshifted by supplementing the media with NaCl. The osmolality of all solutions was measured by determination of the freezing point (Osmomat 030, Gonotec). For microscopy, 2 µl of cells were plated on poly-L-lysine (Sigma) coated cover slips (as described by (van den Bogaart *et al.*, 2007) and measurements were carried out immediately. Each sample was imaged for periods no longer than 25 min.

Microscopy setup, pulsed-FRAP measurements and data analysis

The confocal microscope, diffusion measurements and data analysis were performed as described (van den Bogaart *et al.*, 2007), with the exception that diffusion constant medians were taken as the most representative mobility values instead of arithmetic means. For each osmotic condition, a minimum of 20 single cells was probed to determine the median diffusion constant. All measurements were performed at 20^{o} +/-1^{o} C.

Imaging of cells

For imaging of cells expressing GFP or derivatives, or cells loaded with NBD-glucose, a 488 nm laser line was used with an emission filter of 500-600 nm. Draq-5 was excited with a 633 nm laser line and emission was detected between 650 and 700 nm. mPlum was excited with a 543 nm laser and emission was collected between 600 and 700 nm. The laser intensity did not exceed 100 µW at the back aperture of the objective. Cells were imaged within 25 min as described previously (Elowitz *et al.*, 1999, Konopka *et al.*, 2006, van den Bogaart *et al.*, 2007).

Results

Diffusion of macromolecules drops in osmotically upshifted cells

In this work, we refer to medium osmolalities as ΔLB_{Osm}, that is, the osmolality relative to that of Luria Broth (LB), which has an osmolality of 0.44 Osm/kg. For microscopy measurements, the cells were placed in potassium-free NaPGCl (specified in the ”Materials and methods” section), which hindered cell recovery from osmotic upshifts. Inside cells, growing under normal osmotic conditions, proteins like GFP are evenly distributed throughout the cytoplasm (van den Bogaart *et al.*, 2007, Konopka *et al.*, 2006). When cells are transferred to a medium of higher osmolality than in which they were grown, the mobility of GFP decreases (Cayley *et al.*, 1991, Konopka *et al.*, 2006, van den Bogaart *et al.*, 2007). Figure 1 shows the time evolution of this phenomenon for an individual cell. For this purpose a microfluidic device *(*Rowat *et al.*, 2009) was used, which allows washing of the cells without affecting their position on the microscope slide. The cell was initially exposed to a medium isotonic with the growth medium (ΔLB_{Osm} = 0) and GFP fluorescence remained equally intensive in the entire cell. Upon photobleaching (Fig. 1, 1st purple arrow), the recovery of fluorescence was very fast (Fig. 1, after 1 min) and resulted in a uniform drop of fluorescence throughout the cytoplasm. When the cell was osmotically-upshifted by exposing it to a medium supplemented with 1 M NaCl (Fig. 1, 3 min., white arrow) an instantaneous shrinking of the cytoplasm was observed. When the cell was now photobleached at the same position as before (Fig. 1, 2nd purple arrow), the recovery of fluorescence was relatively slow; even 2 minutes after bleaching, the fluorescence intensity at the bleaching spot was of lower intensity than that of the surrounding cytoplasm (Fig. 1, 5 min). However, diffusion was only slowed

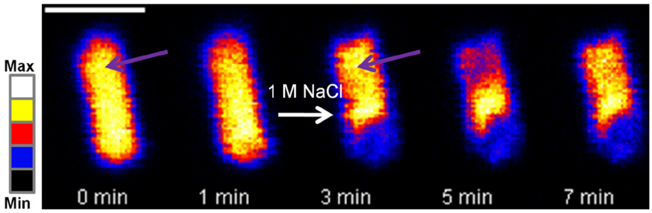

Figure 1. Loss of macromolecule mobility in osmotically upshifted cells. *E. coli* cell in a microfluidic device and expressing GFP was imaged before and after osmotic upshift. Scale bar 2µm. Intensity is presented in rain-bow setting (see scale). At t = 0 min, the cell was under normal osmotic conditions (ΔLBOsm = 0) and had a rod-like shape. Photobleaching (first purple arrow, at 0 min) resulted in uniform loss of fluorescence (1 min) owing to relatively fast GFP diffusion. When the cell was exposed to 1 M NaCl (ΔLBOsm = 1.65, white arrow), the cytoplasmic volume shrunk. Photobleaching at the same spot (3 min, second purple arrow) resulted in an initially non-uniform loss of fluorescence (5 min) and eventually a slow recovery of fluorescence (7 min). Microfluidic devices were handled as described (Rowat *et al.*, 2009).

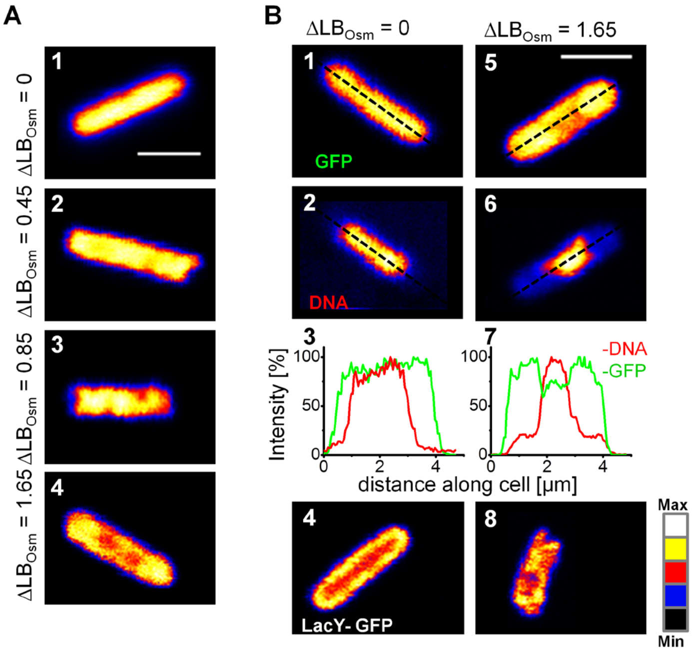

Figure 2. Consequences of osmotic stress for the cell structure. A) Cells expressing GFP: loss of the rod-like shape and uneven GFP distribution became more pronounced with increasing osmotic upshift (subpanels 1 to 4). B) Comparison of cell structure under normal osmotic conditions (subpanels 1-4) and osmotic upshift (subpanels 5-8). Subpanels 1 and 5: cells expressing GFP. Subpanels 2 and 6: staining of DNA with Draq-5. Subpanels 3 and 7: fluorescence intensity distributions of the cross-sections indicated in panels 1 and 5 (green; GFP) and 2 and 6 (red; DNA). Subpanels 4 and 8: images of cells expressing GFP-tagged LacY under normal osmotic conditions (4, ΔLBOsm = 0) and osmotic upshift (8, ΔLBOsm = 1.65). Scale bar 2 µm. Intensity is presented in rain-bow setting (see scale).

down and had not stopped completely, because after some time the bleached spot eventually recovered fluorescence (Fig. 1, 7 min).

Consequences of osmotic upshift on cell structure

Under normal osmotic conditions ($\Delta LB_{Osm} = 0$; Fig. 2), *E. coli* cells had a typical rod-like shape and GFP was evenly distributed throughout the cytoplasm (Fig. 2A, subpanel 1). Shifting cells to media of higher osmolality yielded more irregular and often rectangular-shaped structures. The extent of these changes was proportional to the severity of the osmotic upshift applied (Fig. 2A, subpanels 1 to 4). Significant structural perturbations (invaginations) could be observed in cells at $\Delta LB_{Osm}= 0.85$ (Fig. 2A, subpanel 3), which have been referred to as visual plasmolysis spaces (VPS) (Konopka *et al.*, 2006, Konopka *et al.*, 2009) and are considered as a hallmark of plasmolysis.

Severe osmotic upshifts caused heterogeneities in the cytoplasmatic distribution of GFP. In a fraction of cells imaged (~25%, *n* > 50), the uneven distribution of GFP was so great that one could assign the areas to the nucleoid (Fig. 2B). These areas of cytoplasm had a lower concentration of GFP, which co-localized with a region stained with the DNA binding fluorophore Draq-5. In contrast to the non-stressed cells, GFP seemed partially excluded from the regions stained by Draq-5 (Fig. 2B, compare subpanels 1 - 3 *vs*. 5 - 7). Plotting the signal intensities originating from the GFP and Draq-5 (Fig. 2B, subpanels 3 and 7) reveals that in the osmotically-stressed cells the nucleoid appears separated from the cytoplasm, which is not the case for cells in osmotic balance. Such a change in cellular substructure might imply a kind of phase separation of the nucleoid and the bulk of the cytoplasm, leading to a differential partitioning of macromolecules.

Subsequently, we investigated the effect of osmotic stress on the ultrastructure of the *E.coli* inner membrane, using LacY-GFP fusion as a reporter of the inner membrane. Under normal osmotic conditions, the inner membrane of *E. coli* formed a regular, ellipsoidal ring that borders the cytoplasm (Fig. 2B, panel 4). In osmotically-upshifted cells, the inner membrane invaginated and formed irregular structures (Fig. 2B, panel 8).

Barriers for mobility in osmotically-shocked cells

Previously, it was observed that the cytoplasm undergoes compartmentalization when the medium osmolality is increased by 0.5 M of salt or more (van den Bogaart *et al.*, 2007). Pools of GFP were formed that did not exchange (or exchanged very slowly) their contents, indicating that the cytoplasm had lost continuity or developed a barrier for diffusion. The question is what is the molecular basis for the apparent compartmentalization? To address this point, *E. coli* cells expressing GFP were stained with Draq-5 and imaged. Subsequently, an area of cytoplasm adjacent to the nucleoid (but not the position of the nucleoid itself) was photobleached and a second image was recorded after 120 sec (Fig. 3A). In control experiments, where cells were not exposed to osmotic stress, the photobleaching resulted in a uniform drop of fluorescence, irrespective of the position of the photobleaching laser beam. On the contrary, in cells exposed to osmotic stress, different overlapping ultrastructural phenotypes were observed. The three most extreme cases are depicted schematically in panel A of Fig. 3: (i) cells that did not form barriers for mobility; (ii) cells in which the nucleoid seemed to act as a barrier; and (iii) cells in which the macromolecular crowding seemed to result in much slower diffusion.

The acquired data were visually inspected and the cells were classified according to the three most distinct phenotypes. It was not always possible to unambiguously assign the cells as mixed phenotypes were observed (about 30% of the cells). An example of a cell that does not show visible diffusion barriers is shown in Fig. 3B. This phenotype was observed in 20% of the cells (*n* = 40). These osmotically-upshifted cells could not be discriminated from non-stressed cells. The phenotype in which the nucleoid seems to form a barrier for diffusion (Fig. 3C) was observed in another 20% of the cells. In these cells, the photobleaching of GFP resulted in a homogenous loss of fluorescence in only a part of the cytoplasm, that is, the area where the laser beam was positioned but not the part on the opposite side of the nucleoid. This implies that the DNA forms a physical barrier for diffusion and the photobleached GFP cannot pass this barrier and mix with the non-photobleached GFP on the other side of the nucleoid. In the majority (60%) of the cells, the macromolecular crowding itself seemed to cause a significant decrease in mobility (Fig. 3D). Photobleaching of GFP in those cells did not result in uniformly distributed loss of fluorescence, nor did it cause the entire part of the cytoplasm delimited by the nucleoid to lose fluorescence. In these cells, the photobleached area was not larger than the size of the focused laser beam, indicating that the mobility of GFP was very restricted and hardly any diffusion was observed.

Diffusion as a function of molecular weight in the E. coli cytoplasm

We used pulsed-FRAP (van den Bogaart *et al.*, 2007) to determine the diffusion constants of a fluorescently labeled glucose (NBD-glucose, M_r = 423 Da), a medium sized protein (GFP, M_w = 26.9 kDa) and a large oligomeric protein consisting of four subunits of GFP-tagged β-galactosidase ((β-gal-GFP)$_4$, M_r ~ 582 kDa). Diffusion measurements were performed under non-stress and osmotic stress conditions and the data incl. spread of the measured values are summarized Table 1.. The diffusion constant of GFP in the cytoplasm of *E. coli* dropped with increasing osmotic stress as reported previously (van den Bogaart *et al.*, 2007, Konopka *et al.*, 2006, Konopka *et al.*, 2009). Moreover, the rates of diffusion could be restored by introducing osmo-protectants into the medium. D_{median} for GFP dropped from 3 µm^2/s to 0.5 µm^2/s when cells were exposed to 0.25 M NaCl (ΔLB_{Osm} = 0.45) and the D_{median} returned to 1.5 µm^2/s when the medium was supplemented with 10 mM KCl (Table 1). We were able to measure diffusion constants of GFP with pulsed–FRAP up to osmotic upshifts of 0.25 M NaCl. When the cells were subjected to larger osmotic stresses (0.5 M NaCl or more, ΔLB_{Osm} = 0.85), the photobleaching was not followed by instantaneous recovery and the diffusion coefficient could not be determined accurately. These cells underwent compartmentalization and GFP was essentially immobile with a D value estimated to be lower than 0.001 µm^2/s.

The decrease of diffusion as a function of molecular weight was determined (Fig. 4A); the diffusion median of NBD-glucose, GFP and (β-gal-GFP)$_4$ for cells under normal osmotic conditions was 50, 3 and 0.8 µm^2/s, respectively

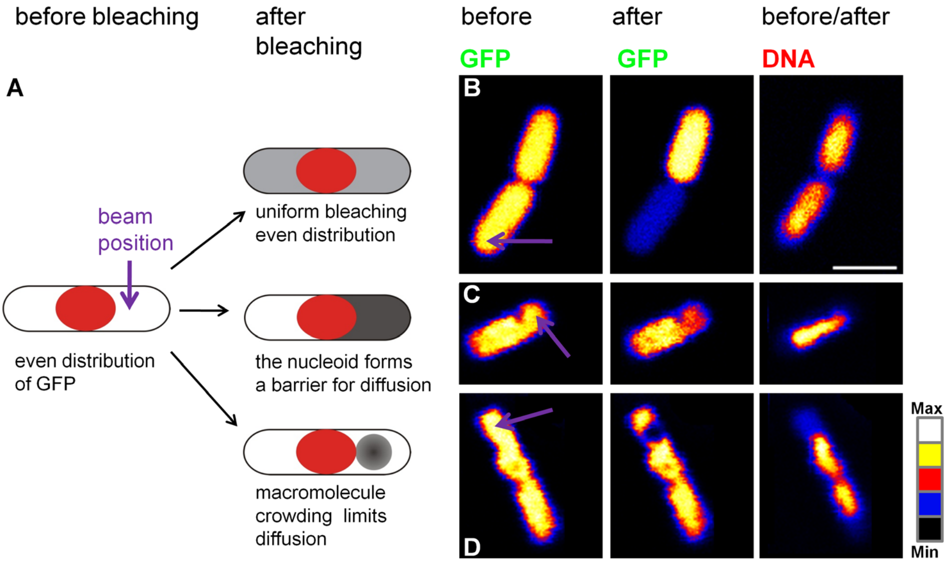

Figure 3. Barriers for mobility in the cytoplasm of osmotically stressed E. coli. A) Schematic representation of the phenotypes observed before and after osmotic upshift. The nucleoid is shown in red, GFP fluorescence intensity is shown in different shades of gray (from white, highest intensity, to dark grey, lowest intensity). B-D) Cells expressing GFP (left images) and co-stained for DNA with Draq-5 (right images). The purple arrow indicates the location of the photobleached spot. Images: B) A cell that does not seem to form barriers for mobility; C) A cell where the nucleoid forms the barrier for mobility; D) A cell in which crowding forms the barrier for mobility. Scale bar 2 µm. Intensity is presented in rain-bow setting (see scale).

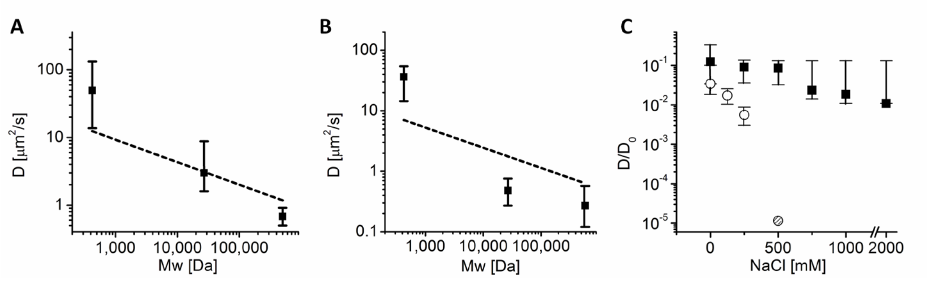

Figure 4. Diffusion decreases with molecule size. Median D values under normal osmotic conditions (A), ΔLBOsm = 0, and moderate osmotic upshift (B), ΔLBOsm = 0.45, as a function of molecular weight (Mw). The broken line represents the Einstein – Stokes relationship (see Results section). C) Diffusion coefficients *in vivo* normalized to those in water (D/ D0) for NBD-glucose (squares) and GFP (circles). The filled data point for GFP at 0.5 M NaCl indicates that the value is an estimate. The error bars indicate the data spread. Interquartile range (IQR) values were taken (Table 1) and divided by D0 (Fig. 3C). Table 1. Diffusion constants of macromolecules in the cytoplasm of *E. coli*.

(Table 1). The decrease in diffusion with increasing molecular weight was even more pronounced for osmotically stressed cells (Fig. 4B). The obtained decay of D as a function of molecular weight was fitted with the simple power dependence:

$$D_{median} = aM^{\exp},$$

where M is the molecular weight of the diffusing molecule and a, a scaling constant. For cells under normal osmotic conditions the exponent was -0.7 and for upshifted cells -0.8 The obtained fits clearly deviate from the Einstein-Stokes equation ($D = aM^{-0.33}$; dashed line in Fig. 4A,B).

It should be stressed that for the data analysis, the shape and density of the molecules was assumed to be similar; see Table 2 for details on the hydrodynamic radii of the molecules.

The dependencies of the diffusion coefficients of NBD-glucose and GFP as a function of salt stress are shown in Fig. 4C. D_{median} values for each osmotic upshift condition were divided by the corresponding values in aqueous media (D_0). Clearly, the slope of diffusion decrease is steeper for GFP than for NBD-glucose as the medium osmolality increases. It is striking that even in cells up-shifted with 2 M NaCl (ΔOsm ~4.5), NBD-glucose still remained mobile (Fig. 4C, Table 1) with a D_{median} of 4.3 µm²/s, whereas GFP became essentially immobile with D values not exceeding 0.001 µm²/s (Table 1). This implies that in plasmolyzing cells low molecular weight compounds (e.g. metabolites) still diffuse whereas macromolecules (e.g. enzymes) are confined to a fixed position.

No barriers for diffusion of small molecules

To unambiguously show that above threshold values of osmotic stress macromolecules like GFP lose mobility and are trapped in compartments, while small molecules can still probe the entire cytoplasmic space, we performed a dual-color FRAP experiment. For simultaneous probing of the mobility of high (fluorescent proteins) and low molecular weight species (NBD-glucose) in the same cell, we substituted GFP with the red-shifted fluorescent protein mPlum (Wang *et al.*, 2004).

Macro-molecule	Mw [kDa]	NaCl added [M]	Δ LB_{Osm} [Osm/kg] (1)	Median *D* [$\mu m^2/s$]	*D* range [$\mu m^2/s$]	*D* IQR (2)	*N* (3)
NBD-glucose	0.423	0	0	**49.5**	2.35-240	13.7 -133.4	63
		0.25	0.45	**36.5**	2.83-240	14.4-54.5	65
		0.5	0.85	**34.0**	0.42-64	12.9-52.8	25
		0.75	1.28	**9.4**	4.4 -65.6	5.7-52.8	25
		1	1.8	**7.5**	0.9-232	4.4-52.8	64
		2	~4.5	**4.3**	0.64-199	3.2-14	34
GFP	26.796	0	0	**3.0**	0.25-240	1.6 -8.8	60
		0.125	0.18	**1.8**	0.25-232	0.9 -2.25	30
		0.25	0.45	**0.48**	0.027-240	0.27-0.76	30
		0.25 + 10mM KCl	0.45	**1.5**	0.13-232	0.9-3.4	25
		0.500	0.85	* (4)	-	-	-
(β-Gal-GFP)$_4$	582.222	0	0	**0.68**	0.086-11.62	0.5-0.9	36
		0.250	0.45	**0.27**	0.0072-4.52	0.12-0.57	39

Table 1. Diffusion constants of macromolecules in the cytoplasm of *E.coli.*
1) Difference in osmolality relative to LB.
2) The interquartile range (IQR) of *D* values, i.e. the range where the middle half of all measured *D* values lie.
3) Number of single cell measurements.
4) No recovery of GFP fluorescence after photobleaching was observed, i.e. $D < 0.001\ \mu m^2/s$.

Molecule	M_w [Da]	Calculated radius(1)	*D* in water(2)	Radius determined on the basis of *D*(3)
NBD-glucose	423	0.49 nm	400 +/- 60 $\mu m^2/s$(4)	0.53 +/- 0.08nm
GFP	26,796	2.00 and 2.55 nm(6)	87 +/- 12 $\mu m^2/s$(5)	2.46 +/- 0.4 nm
(β-gal-GFP)$_4$	582,222	5.55 nm	n.d.[7]	n.d.

Table 2. Hydrodynamic radii of GFP and NBD-glucose
1) Radius calculated on the basis of molecular weight, using the following equation:

$$R_S = \sqrt[3]{\frac{3Mw}{4\pi N_A \rho}}\ ,$$

where R_s is the Stokes radius of the molecule, Mw is the molecular weight, N_A the Avogadro constant and ρ the density of the particle (calculated from composition, using the program sednterp (http://jphilo.mailway.com/download.htm).
2) The diffusion coefficient was determined in water at 20°C by fluorescence correlation spectroscopy (FCS), as described previously (Veldhuis *et al*, 2006).
3) The Stokes radius was calculated from the *D* values, using the Einstein-Stokes relationship:

$$D = \frac{k_B T}{6\pi\eta R_S}\ ,$$

where, k_B is the Boltzman constant, T the temperature and η the viscosity of the medium.
4) *D* value determined in this work at 20°C.
5) *D* as measured previously (Potma *et al.*, 2001).
6) Values for monomeric and dimeric GFP, respectively.
7) n.d., not determined

E. coli cells expressing mPlum were loaded with NBD-glucose and exposed to different degrees of osmotic upshift. In the vast majority (92%, n = 24) of osmotically stressed cells (addition of 0.5 M NaCl, $\Delta LB_{Osm} = 0.85$) mPlum fluorescence did not recover after photobleaching, while NBD-glucose was distributed homogenously along the cell (Fig. 5). Severe osmotic stress does not influence the continuity of the cytoplasm for low molecular weight species. The cytoplasm appears to act as a meshwork allowing small molecules to diffuse freely whereas macromolecules get trapped, possibly due to the porosity, constriction or density of the macromolecular meshwork or because they cannot transit the barriers of different compartments.

The experimentally determined radii of GFP and NBD-glucose (using FCS) do not differ significantly from those calculated on the basis of the molecular weight.

Discussion

In this study, we have used pulsed-FRAP and confocal imaging to probe the mobility of molecules of different sizes in the cytoplasm of *E. coli* under normal osmotic conditions and hyperosmotic stress. We show that low molecular compounds can diffuse freely even in severely osmotically-stressed cells, whereas proteins get trapped in subcompartments or become virtually immobile because of extreme crowding. Thus, owing to their high crowding, prokarya are readily impacted in their physiology upon osmotic challenge. Threshold values for mobility of macromolecules are reached even at moderate levels of osmotic stress.

Mobility of small molecules

The diffusion coefficient of NBD-glucose in the cytoplasm of live *E. coli* was 50 µm^2/s, which reflects a seven to eightfold reduction in mobility compared to aqueous solutions. The diffusion coefficient for NBD-glucose in water was around 400 ± 60 µm^2/s (Table 2), which is similar to what has been reported for molecules of this size (e.g. Alexa fluor 488 is 380 µm^2/s at 20^{o}C (Petrasek &

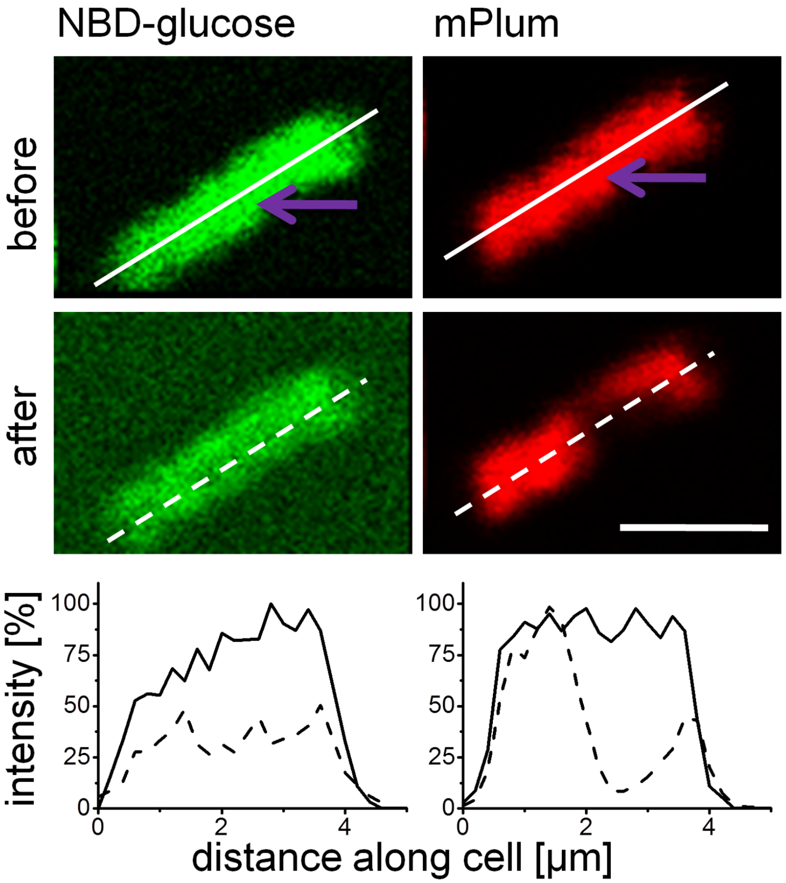

Figure 5. The cytoplasm of osmotically upshifted cells forms mobility barriers for proteins (mPlum) but not for small molecules (NBD-glucose). Pseudo colored images of an *E. coli* cell treated with 0.5 M NaCl (ΔLBOsm = 0.85). Left panels, NBD-glucose (green) and right panels, mPlum (red). The purple arrow indicates the photo-bleaching spot. Upper panels show cells before, and lower panels 2 min after, photo-bleaching. The graphs indicate the normalized fluorescence intensities of the cell along the longer cell axis (white line through the cell) before (solid line) and after bleaching (dashed line). Scale bar 2µm.

Schwille, 2008)**.** Kao and coworkers (Kao *et al.*, 1993) have probed the mobility of a small molecular weight dye BCECF in the cytoplasm of Swiss 3T3 fibroblasts. They reported a 4-fold slower diffusion in the fibroblast cytoplasm than in diluted aqueous environments, which is consistent with our data as prokarya are more highly crowded than these eukaryotic cells (Ellis, 2001). We have tried to perform pulsed-FRAP measurements with this probe and observed that BCECF was not a suitable reporter of small molecule mobility in the cytoplasm of *E. coli* as the cells were not uniformly stained. Moreover, and consistent with our findings, BCECF has been reported to bind to other molecules in the matrix of mitochondria (Partikian *et al.*, 1998), resulting in very slow diffusion (Scalettar *et al.*, 1991).

Mobility of GFP

As reported previously (van den Bogaart *et al.*, 2007, Konopka *et al.*, 2006, Elowitz *et al.*, 1999, Mullineaux *et al.*, 2006) and confirmed here, translational diffusion of GFP in the cytoplasm of *E.coli* is an order of magnitude slower than in aqueous media. The D_{median} determined in this work is 3 µm^2/s, which is the same as reported previously reported (van den Bogaart *et al.*, 2007) and in reasonable agreement with values presented by others: 6, 7, 10 and 12 µm^2/s in (Konopka *et al.*, 2006, Elowitz *et al.*, 1999, Mullineaux *et al.*, 2006, Konopka *et al.*, 2009). The diffusion of GFP in the cytoplasm of eukaryotic cells, e.g. Swiss 3T3 fibroblasts and *Dictyostelium* cells, seems significantly higher with values of 27 and 24 µm^2/s, respectively (Swaminathan *et al.*, 1997, Potma *et al.*, 2001).

Mobility of very large macromolecules

The D_{median} of the ~582 kDa fusion protein (β-gal-gfp)$_{4,}$ in the cytoplasm of *E. coli* was 0.8 µm^2/s, which is relatively slow but is still significant because the molecules will traverse the cell several times each minute. About a decade ago, Elowitz *et al.*, (1999) examined the mobility of this molecular species in *E. coli* cells and concluded that (β-gal-gfp)$_4$ was immobile. However, under their experimental conditions the fusion protein was not uniformly distributed throughout the cell. We believe that this indicates that the β-galactosidase moiety was not correctly folded, leading to large aggregates (inclusion bodies), which are immobile. We deliberately used a low inducer concentration (0.0002% w/v L-arabinose) and low temperature (30^{o}C) to allow the multidomain fusion protein to fold correctly. Indeed, we observed uniform distribution of the protein throughout the cytoplasm in the vast majority of the cells (~95%). Cells that showed signs of inclusion bodies were not used for the pulsed-FRAP measurements. We could reproduce the observations of Elowitz by expressing the protein at 37^{o}C and using higher L-arabinose concentrations (0.02 w/v %).

The cytoplasm as a crowded meshwork

We observed different regimes in osmotic stress: (i) a moderate upshift ($\Delta LB_{Osm} < 0.45$) resulted in a general decrease of mobility; (ii) a more severe osmotic upshift ($\Delta LB_{Osm} \geq 0.85$) resulted in heterogeneities in the cytoplasm and introduced barriers for diffusion. Under these conditions, proteins of the size of GFP or bigger are no longer able to travel the entire cytoplasmic space. Dauty & Verkman, (2004) studied the role of macromolecule crowding on the diffusion of differently sized macromolecules *in vitro* by elevating ficoll-70 concentration. The reduction in translational diffusion as a function of crowding was similar for molecules of different size. We observe that in live *E. coli* cells small molecules are slowed less than bigger ones, when the apparent crowding is increased by osmotic upshifts. In the cytoplasm of *E. coli* macromolecular structures of different size are present and the mobility is influenced by immobile obstacles (such as the nucleoid) or transient binding to cytoplasmic elements, which manifests itself in particular under conditions of hyperosmotic stress. In addition, translational diffusion of macromolecules seems to show a power-dependent drop with macromolecule-size increase, but the observed decays substantially deviate from the Einstein-Stokes relationship, where the dependence of *D* on molecular weight (for globular-shaped molecules) has a cubic root dependence (Table 2). A similar finding was recently reported by others (Kumar *et al.*, 2010). The dependence of *D* on molecular weight obtained in this study can be used as a coarse approximation of the mobility of macromolecules in the cytoplasm of *E. coli,* for which no such data is available. The bacterial cytoplasm appears as a crowded meshwork in which intrinsic molecular species might get confined. As water leaves the cytoplasm the crowding of the cytoplasm increases and the meshwork becomes tighter, allowing NBD-glucose to diffuse through whereas macromolecules get trapped.

Does the nucleoid form a barrier for mobility?

The idea that the nucleoid would form the mobility barrier in highly stressed cells was introduced previously (van den Bogaart *et al.*, 2007, Konopka *et al.*, 2009). It was proposed that the inner membrane would come in physical contact with the bacterial nucleoid (van den Bogaart *et al.*, 2007). Konopka *et al.*, (2009) suggested that the porosity of the nucleoid towards molecules of different size might vary with the extent of osmotic shock. In the light of our new measurements, we conclude that in osmotically-stressed cells not only the nucleoid forms a barrier but that macromolecular crowding itself can contribute even more significantly to the slowing down of macromolecule diffusion, which might appear as formation of diffusion barriers. Importantly, formation of these apparent barriers is reversible.

Consequences of retained mobility of NBD-glucose

Under conditions of high osmotic stress ($\Delta LB_{Osm} \geq 0.85$) the low molecular weight fluorophore (NBD-glucose) was still mobile and able to probe the entire cytoplasmic space. Although the diffusion of enzymes may have almost halted under these conditions, biochemical activity may continue as long as metabolites are still mobile. This implies that small, important metabolites such as pathway intermediates, ATP, signaling molecules and inorganic ions are available in the entire cytoplasm regardless of the strength of the osmotic stress. Most likely, osmoprotectants also diffuse rapidly and their omnipresence and fast redistribution from spots of uptake or synthesis helps the restoration of osmotic balance.

Acknowledgements

We thank Amy Rowat at Harvard Medical School for supplying us with the microfluidic devices. We acknowledge financial support from SysMo via the BBSRC-funded KosmoBac programme coordinated by Ian R Booth (Aberdeen) and the NWO (Top-subsidy grant 700.56.302).

References

Batra, J., Xu, K., Qin, S. and Zhou, H.Z. (2009) Effect of macromolecular crowding on protein binding stability: modest stabilization and significant biological consequences. *Biophys J* **97**: 906-911.

Booth, I. R., Edwards, M.D., Black, S., Schumann, U. and Miller, S. (2007) Mechanosensitive channels in bacteria: signs of closure? *Nat Rev Microbiol* **5**: 431-440.

Cayley, S., Lewis, B.A., Guttman, H.J. and Record, M.T (1991) Characterization of the cytoplasm of Escherichia coli K-12 as a function of external osmolarity. Implications for protein-DNA interactions *in vivo*. *J Mol Biol* **222**: 281-300.

Cayley, S. and Record, M.T., (2004) Large changes in cytoplasmic biopolymer concentration with osmolality indicate that macromolecular crowding may regulate protein-DNA interactions and growth rate in osmotically stressed Escherichia coli K-12. *J Mol Recognit* **17**: 488-496.

Dauty, E. and Verkman, A.S. (2004) Molecular crowding reduces to a similar extent the diffusion of small solutes and macromolecules: measurement by fluorescence correlation spectroscopy. *J Mol Recognit* **17**: 441-447.

Ellis, R. J., (2001) Macromolecular crowding: obvious but underappreciated. *Trends Biochem Sci* **26**: 597-604.

Elowitz, M. B., Surette, M.G., Wolf, P.E., Stock, J.B. and Leibler, S. (1999) Protein mobility in the cytoplasm of Escherichia coli. *J Bacteriol* **181**: 197-203.

Geertsma, E. R., Groeneveld, M., Slotboom, D.J. and Poolman, B. (2008) Quality control of overexpressed membrane proteins. *Proc Natl Acad Sci U S A* **105**: 5722-5727.

Kao, H. P., Abney, J.R. and Verkman, A.S. (1993) Determinants of the translational mobility of a small solute in cell cytoplasm. *J Cell Biol* **120**: 175-184.

Konopka, M. C., Shkel, I.A., Cayley, S., Record, M.T. and Weisshaar, J.C. (2006) Crowding and confinement effects on protein diffusion *in vivo*. *J Bacteriol* **188**: 6115-6123.

Konopka, M. C., Sochacki, K.A., Bratton, B.P., Shkel, I.A., Record M.T. and Weisshaar, J.C. (2009) Cytoplasmic protein mobility in osmotically stressed Escherichia coli. *J Bacteriol* **191**: 231-237.

Kumar, M., Mommer, M. S. and Sourjik, V. (2010) Mobility of cytoplasmic, membrane and DNA-binding proteins in *Escherichia coli*. *Biophys. J* **98**: 552-559.

Mullineaux, C. W., Nenninger, A., Ray, N. and Robinson, C. (2006) Diffusion of green fluorescent protein in three cell environments in Escherichia coli. *J Bacteriol* **188**: 3442-3448.

Petrasek, Z. and Schwille, P. (2008) Precise measurement of diffusion coefficients using scanning fluorescence correlation spectroscopy. *Biophys J* **94**: 1437-1448.

Potma, E. O., de Boeij, W.P., Bosgraaf, L., Roelofs, J., van Haastert, P.J. and Wiersma, D.A. (2001) Reduced protein diffusion rate by cytoskeleton in vegetative and polarized dictyostelium cells. *Biophys J* **81**: 2010-2019.

Rowat, A. C., Bird, J.C., Agresti, J.J., Rando, O.J. and Weitz, D.A. (2009) Tracking lineages of single cells in lines using a microfluidic device. *Proc Natl Acad Sci U S A* **106**: 18149-18154.

Scalettar, B. A., Abney J.R. and Hackenbrock, C.R. (1991) Dynamics, structure, and function are coupled in the mitochondrial matrix. *Proc Natl Acad Sci U S A* **88**: 8057-8061.

Slade, K. M., Baker, R., Chua, M., Thompson, N.L. and Pielak, G.J. (2009a) Effects of recombinant protein expression on green fluorescent protein diffusion in Escherichia coli. *Biochemistry* **48**: 5083-5089.

Slade, K. M., Steele, B.L., Pielak, G.J. and Thompson, N.L. (2009b) Quantifying green fluorescent protein diffusion in Escherichia coli by using continuous photobleaching with evanescent illumination. *J Phys Chem B* **113**: 4837-4845.

Swaminathan, R., Hoang, C.P and Verkman, A.S. (1997) Photobleaching recovery and anisotropy decay of green fluorescent protein GFP-S65T in solution and cells: cytoplasmic viscosity probed by green fluorescent protein translational and rotational diffusion. *Biophys J* **72**: 1900-1907.

van den Bogaart, G., Hermans, N., Krasnikov, V. and Poolman, B. (2007) Protein mobility and diffusive barriers in Escherichia coli: consequences of osmotic stress. *Mol Microbiol* **64**: 858-871.

Wang, L., Jackson, W.C., Steinbach, P.A. and Tsien, R.Y. (2004) Evolution of new nonantibody proteins via iterative somatic hypermutation. *Proc Natl Acad Sci U S A* **101**: 16745-16749.

Wood, J. M. (1999) Osmosensing by bacteria: signals and membrane-based sensors. *Microbiol Mol Biol Rev* **63**: 230-262.

CHAPTER 5

OSMOTIC STRESS AND PHYSIOLOGICAL RESPONSE OF *ESCHERICHIA COLI* AT THE SINGLE-CELL LEVEL

Jacek T. Mika, Victor Krasnikov, Liesbeth M. Veenhoff & Bert Poolman

Manuscript in preparation

By employing flow chambers, we have analyzed the response and adaptation of *E. coli* cells to osmotic stress. We have used the fluorescence of cytosolically-expressed GFP to probe the volume of the cytoplasm and the mobility of the protein in individual cells before, during and up to one hour after imposing an osmotic upshift. We find that the volume of the cytoplasm and the mobility of GFP drop instantaneously upon osmotic upshift and both parameters recover in parallel over periods of tens of minutes. The response of cells is heterogeneous in the probed population.

Introduction

The cytoplasm of *E.coli* is a crowded environment with macromolecule concentrations in the range of 200-300 g/l under normal osmotic conditions (Zimmerman & Trach, 1991, Cayley *et al.*, 1991). The crowding of bacteria is higher than that of eukaryotic cells (Mika & Poolman, 2011). In such an environment the diffusion of macromolecules is relatively slow. For instance, the diffusion of GFP in the cytoplasm of *E.coli* is in the range of 3 to 14 µm^2/s (Mika & Poolman, 2011), which compares to a value of 27 µm^2/s for Chinese hamster ovary cells (Swaminathan *et al.*, 1997) and 24 µm^2/s for *Dictyostelyum* cells and is about 10 times slower than in dilute aqueous solutions (87 µm^2/s (Potma *et al.*, 2001)). The diffusion of metabolite analogues (e.g. NBD-glucose, Mw = 324 Da, D = ~50 µm^2/s) and large protein complexes [e.g. (β-galactosidase-GFP)$_4$), Mw = 588 kDa, D = 0.8 µm^2/s) is also significantly slower than in water (Mika *et al.*, 2010).

When *E. coli* cells are washed with solutions of higher osmolality than that of the growth medium, they experience an osmotic upshift (for a comprehensive review see (Wood, 1999)). As a result of the osmotic upshift, water leaves the cytoplasm (Booth *et al.*, 2007) and the volume of the cell decreases. Under extreme hyperosmotic stress, the only water left is that of the hydration of macromolecules ((Konopka *et al.*, 2007) and references therein). The cytoplasm can shrink down to 60% of its initial volume (Koch, 1984, Wood, 1999). Consequently macromolecule crowding can increase up to 400 g/l (Cayley *et al.*, 1991). The diffusion of macromolecules in this even more crowded environment is reduced to 0.01 µm^2/s for GFP ((Konopka *et al.*, 2006) and this work Fig. 3).

Bacteria have developed mechanisms to adapt to increases in medium osmolality (Wood *et al.*, 2001, Wood, 2011, Sleator & Hill, 2002, Wood, 1999). These mechanisms involve uptake of potassium ions and compatible solutes such as glycine betaine and proline. Moreover, the *E.coli* response to osmotic challenges also involves the synthesis of osmoprotectants, e.g. trehalose. Other (micro)organisms employ similar strategies although the compatible solutes accumulated may vary. Most often however, quaternary ammonium compounds like glycine betaine, carnitine and trimethylamine *N*-oxide are among the preferred compatible solutes (Sleator & Hill, 2002). Accumulation of compatible solute, be it via transport or synthesis, eventually leads to the restoration of cytoplasmic volume (Wood, 1999) and macromolecule mobility (Konopka, 2009).

With the development of flow chambers, we can now probe the consequences of osmotic stress and the physiological response of an individual cell. This allows one to analyze population heterogeneity and obtain a more quantitative understanding of the response of cells to osmotic stress. We have been able to measure the kinetics of shrinkage and recovery of the cytoplasm and mobility of macromolecules and show that the two processes are correlated. We demonstrate that a cell, when challenged with osmotic shock for the second time, responds differently. We discuss the physiological processes involved in cell adaptation to increased medium osmolality.

Materials and methods

Strains and Cell growth

Escherichia coli K-12 strain MG1655 harboring the pGFPCR plasmid (van den Bogaart *et al.*, 2007) was grown as described previously (Mika *et al.*, 2010). Briefly, the cells were grown from single colonies in Luria Broth [10 g/L Bacto Tryptone (Becton Dickinson), 5 g/L Yeast extract (Becton Dickinson) plus 10 g /L NaCl (Merck)] supplemented with 100 µg/L ampicillin (Sigma) at 37^{O} C with vigorous shaking until the culture reached an OD_{600} = 0.3–0.4. Leaky expression of GFP from the pGFPCR plasmid was sufficiently high to allow measurements without inducing the cells.

Experimental set up

To enable washing with media of different osmolality, while performing microscopy, the cells were inserted into µ-Slide VI ibiTreat flow chambers (IBIDI, Martinsried, Germany). The flow chambers were coated with poly-L-lysine to restrict cell motion. A constant flow was obtained by using a syringe pump (Harvard Apparatus, Holliston, MA, USA, model 55-1144). After loading the cells into the flow chambers, LB was flushed through, to remove the cells that had not attached to the chamber surface. The flow was then stopped and the first measurements were carried out (condition ”before” or time point 0 min). Subsequently, a solution of LB plus 0.5 M NaCl was pumped through the system for 2 minutes to ensure complete medium exchange. Images of cells were acquired as the cells were washed with the medium of higher osmolality (Fig. 2). The cells were left in LB plus 0.5 M NaCl for one hour during which cytoplasmic volume was measured by acquiring images and GFP diffusion coefficients were determined by performing FRAP. All measurements were performed at 20 +/- 1°C.

Microscope set up

The microscope used is described in detail in Chapter 3 and is very similar to the microscope set-up described by Konopka (Konopka *et al.*, 2006). Briefly, a home-built set up was used based on a on a wide-field microscope: Observer D1 (Carl Zeiss, Jena, Germany). The laser beam (488 nm, argon ion laser, Melles Griot, Carlsbad, CA, USA) was focused by a Zeiss C-Apochromat infinity-corrected 1.2 NA 63× water-immersion objective and directed to the sample. The fluorescence emission was collected through the same objective and separated from the excitation beam by a dichroic mirror (Chroma Technology, Rockingham, VT, USA) and further directed through a 488 nm cut off filter (Notch filter, CVI, Melles Griot, Carlsbad, CA, USA). The fluorescence signal was collected by a Cool-Snap HQ2 CCD camera (Photometrics, Tucson, AZ, USA).

FRAP and Cytoplasm volume analysis

For details of the FRAP measurement and analysis see chapter 3. FRAP was performed as reported by Elowitz (Elowitz *et al.*, 1999) and Konopka (Konopka *et al.*, 2006). For the averaged data (Fig. 3C, squares), the values were grouped as follows: before upshift (0 min), just after upshift (1-5 min) and subsequently during the recovery phase (6-10, 11-20, 21-30, 31-40, 41-50 and 51-60 min). In each time period, the median of the diffusion coefficients was taken as representative. To indicate the data spread, the interquartile range (where 50%

of the data lie) is shown as error bars (Fig. 3C). This approach has been used before by (Konopka *et al.*, 2009, Mika *et al.*, 2010).

Cytoplasmic volumes were calculated from the fluorescence images of *E. coli* cells expressing GFP in the cytoplasm. An arbitrary threshold was applied to the images to distinguish between background fluorescence and GFP. The area of the image occupied by the cell was quantified using either Metamorph (Molecular Devices Inc., Sunnyvale CA, USA), for data presented in Fig. 3, 4 and 5 or ImageJ (NIH, USA), for data in Fig. 2. The obtained cytoplasmic areas were normalized taking the area of cells before upshift as 100%. These areas are transverse sections of the cell, in the middle of the cell, where the cytoplasmic area is widest, see also studies by the Altendorf group (Hamann *et al.*, 2008). The widefield images are two-dimensional and there is no information about the depth of the cell (no Z-axis profile).

An alternative method was proposed by Baldwin and Bankston (Baldwin & Bankston, 1988). They calculate *E.*coli cell volumes from transversonal section images (cell areas), assuming the *E.coli* cell to be well approximated by a cylinder with two, symmetrical spheres at cell poles. This assumption, however, does not hold true for the upshifted cells as these no longer have rod-shaped morphologies of the cytoplasm and it cannot be assumed that the cell width and depth are identical. Therefore this method is not amenable for our study.

The cytoplasmic volume data were divided in the same time periods as the diffusion coefficients to calculate the arithmetic averages and standard deviations as shown in Fig. 3C (circles).

Results

Observations in individual cells

The IBIDI flow chamber was used to probe individual cells before, upon and after omostic upshift. This device enabled us to measure the cells' volume and the mobility of GFP over prolonged periods of time without affecting their position. The set-up of the experiment is outlined in Figure 1. During the exposure of the cell to the hyperosmotic solution a snapshot is taken every second

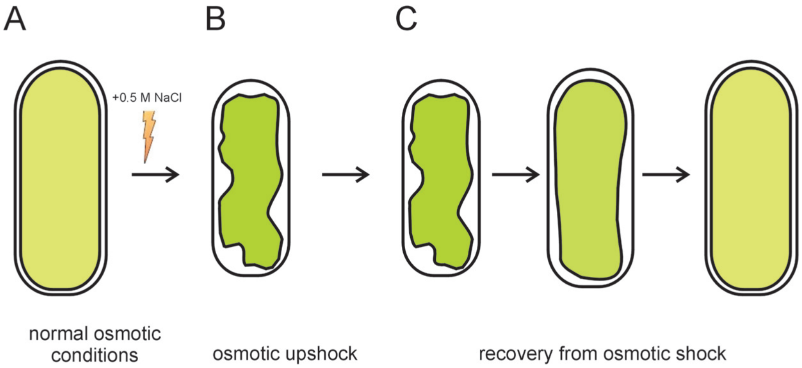

Figure 1. Outline of osmotic stress experiments. A: the cell is initially in osmotic balance. B: the cell is exposed to LB medium plus 0.5 M NaCl. C: the cells is kept in the high-osmolarity medium and allowed to recover for 1 hour; the cytoplasmic volume and GFP diffusion is determined at various time-points (C). the cytoplasmic volume is calculated from the GFP intensity of the images (A-C) and GFP diffusion is measured by FRAP (A and C), see text for details.

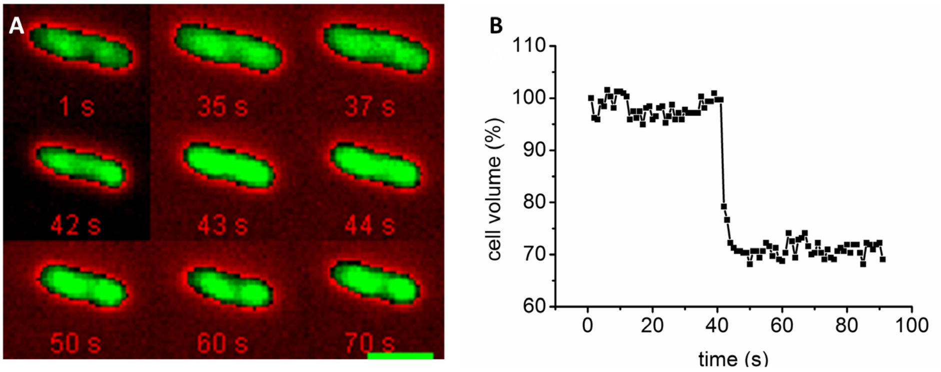

Figure 2. Snapshots of E.coli upon exposure to osmotic upshift. A: false colored snapshots of an *E. coli* cell expressing GFP. Scale bar 2µm. Timestamp of each panel indicates the time elapsed since the start of the experiment. The osmotic upshift was imposed at time 40s B: Quantification of the cytoplasmic volume.

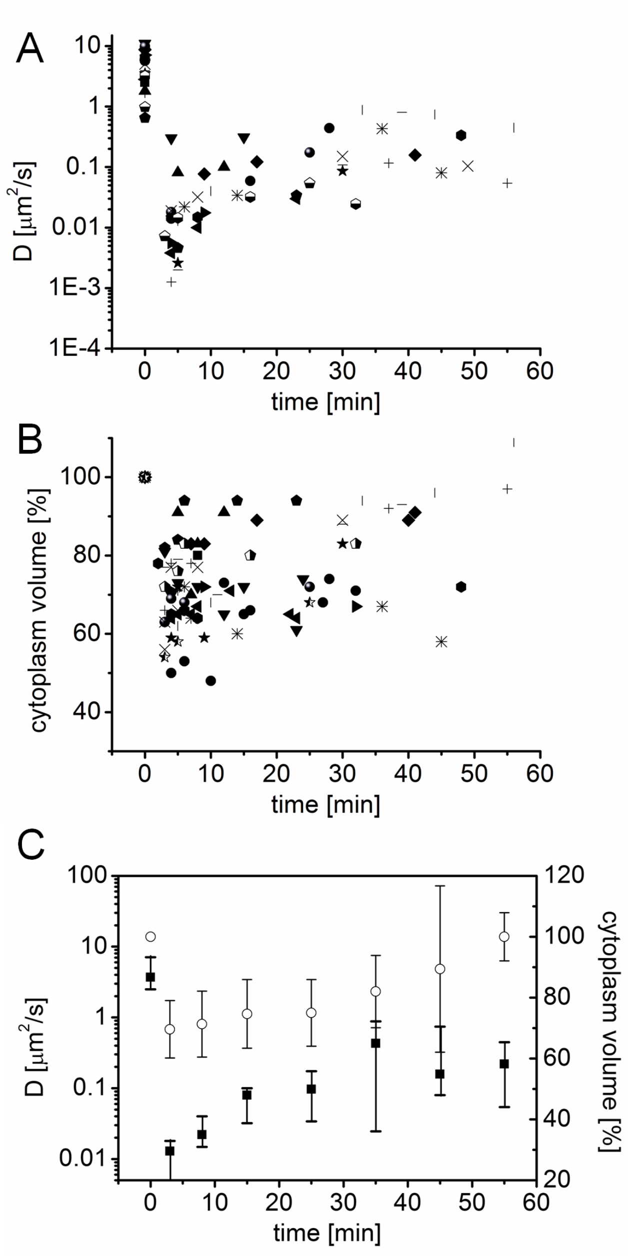

Figure 3. Recovery of GFP mobility and cell volume are correlated. A: mobility of GFP, indicated as D values and B: normalized cytoplasmic volumes measured for individual cells (each cell represented by a unique symbol; symbols between graphs match). Osmotic upshift was imposed just after acquisition of values at time zero. C: squares: median diffusion coefficients of GFP; circles: arithmetic average of cytoplasmic volume; data were averaged for individual cells (n=16). Error bars of diffusion coefficients are inter-quartile ranges, whereas the error bars for cytoplasmic volumes represent standard deviations.

to record the loss of the cytoplasmic volume during and after changing of the outside medium.

Subsequently, the cells were kept in the hyperosmotic solution and, at given time intervals, the diffusion coefficient (*D*) of GFP was determined by conventional FRAP and the cytoplasmic volume was measured. Within the timeframe of the experiment (up to one hour after osmotic upshift), the cells, osmotically challenged in the LB medium, recovered substantially.

The consequences for the cell of an osmotic upshift are immediate

The shrinkage of the cytoplasm upon osmotic upshift occurred within seconds (Fig 2). A typical trace of the cytoplasmic volume change is shown in Figure 2B. When individual cells were analyzed (*n*=10) the consequences of an osmotic upshift were quite heterogeneous. On average, the decrease in cytoplasmic volume was 20%-30% and complete within 5 seconds when the medium was shifted from 0.44 to 1.44 Osm. Most likely, the water leaves the cytoplasm passively, however, contributions from aquaporin AqpZ are possible (Kumar *et al.*, 2007)). A 20% decrease in cytoplasmic volume will lead to a significant increase in crowding, ionic strength and cytoplasmic osmolality. On average, the mobility of GFP dropped from 4 $\mu m^2/s$ to 0.013 $\mu m^2/s$ under these conditions. The impact of the decrease in volume on the intracellular traffic is thus enormous.

Recovery of cytoplasmic volume parallels changes in GFP mobility

Cells can adapt to growing in media of high osmolarity (Konopka *et al.*, 2007). It has been shown that the diffusion coefficient of GFP in the cytoplasm of adapted *E. coli* cells is similar to that of untreated cells (Konopka, 2009). We now analyzed cell recovery from osmotic shock as a function of time, at the single cell level. Figure 3 shows the values of the GFP diffusion coefficients (Fig. 3A) and cytoplasmic volumes (Fig. 3B) of individual cells before, just after the osmotic upshift and during the recovery phase (see Fig.1 for the outline of the experiment). The immediate consequence of the osmotic upshift and the recovery over a period of about 30 min is clearly visible in all cells. To obtain representative averages of the values for *D* and volume (*V*), the data were binned in the following categories: before upshift (0 min), just after the upshift (1-5 min and 6-10 min) and at later times (11-20 min, 21-30 min, 31-40 min, 41-50 min, 51 -60 min). We calculated average cytoplasmic volumes together with their standard deviations, as well as medians of the GFP diffusion coefficients and the corresponding interquartile ranges (see Materials and Methods section) for all the measurements (Fig. 3C). Despite significant variation, the average values show even more clearly the trends already seen in the individual cells (Fig. 3 and Fig.4): *D* and *V* drop within seconds upon exposure to osmotic upshift and recovery takes place over minutes to hours. The recovery from hyperosmotic stress can be divided into a rapid phase (first 5-10 min) and a slower one (10-60 min). The latter may involve the synthesis of new proteins (e.g. proteins involved in the synthesis of osmoprotectants such as trehalose).

Heterogeneous response of cells to osmotic upshock

The 16 cells probed for heterogeneity responded differently to the osmotic stress, at least quantitatively (Fig. 4). While in general the *D* values and cytoplasmic volumes recovered over time as the cells were adapting to increased osmolality, the GFP diffusion coefficients never returned to the values they had in the cells prior to the osmotic upshift (Fig. 4). By the end of the experiment, 5 out of 16 cells had their cytoplasmic volume recovered to at least 90% of the initial value (Fig. 4 B, D, I, K, L). 3/16 cells did not display an increase in GFP diffusion coefficient after the initial drop (Fig. 4 B,C,D) and 6/16 cells did not show restoration of the cytoplasmic volume (Fig. 4 C,E,F,G,J). One cell did not seem to recover from osmotic upshift as both the *D* values for GFP and the cytoplasmic volume did not change over a period of 30 min (Fig. 4 C).

Cells adapt to osmotic stress

We have now shown that within one hour after imposing an osmotic upshift of 1 Osm, using Luria Broth as the basal medium, the cytoplasmic volume

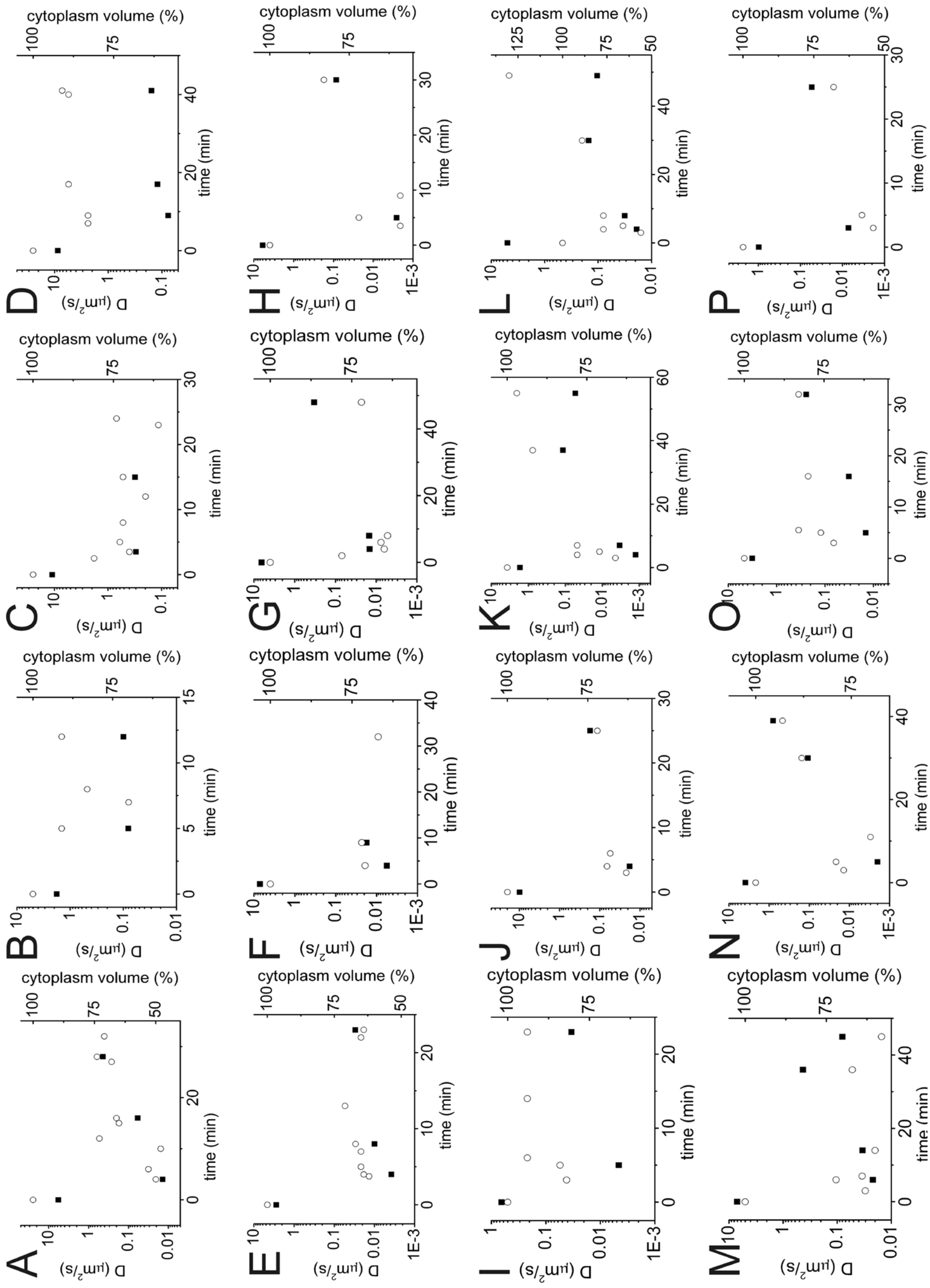

Figure 4. ***Population heterogeneity in the response of cells to osmotic upshift.*** The diffusion coefficient for GFP (squares) and cytoplasmic volumes (circles) of individual cells are indicated. Panels A to P display the datasets obtained for individual cells.

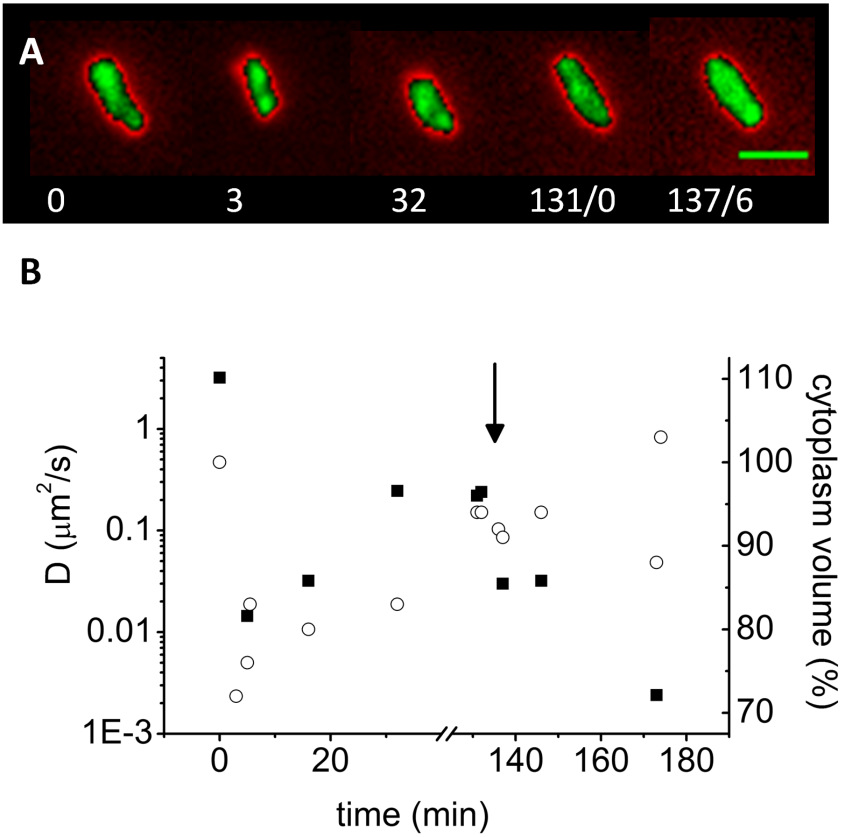

Figure 5. Response of osmotically-adapted E. coli cells to a second osmotic upshift. An *E. coli* cell was exposed to osmotic upshifts twice. Initially the cell was in LB (0 min) and exposed to LB plus 0.5 M NaCl at time zero. The cell was kept at the increased osmolality medium for 131 min and subsequently exposed to LB plus 1.0 M NaCl. A: False colored images of *E. coli* cells expressing GFP. Cell before second osmotic upshift (t=0) and just after the addition of 0.5 M NaCl (t=3 min). At 131 min (panel 131/0 min), the cell was exposed to a second osmotic upshift. Last panel (137/6 min) – the cell 6 min after the second upshift. Scale bar 2 μm. B: Quantification of mobility of GFP (squares) and normalized cytoplasmic volume (circles) for the cell shown in panel A. The second osmotic upshift is indicated by an arrow.

and macromolecule mobility are largely restored in the majority of cells (Fig. 3). A question remaining is whether non-adapted and adapted cells respond differently to osmotic stress. We thus exposed cells to an osmotic upshift twice (Fig. 5). First, the cell was shocked with 0.5 M NaCl (LB plus 0.5 M NaCl) and allowed to recover for two hours. During this time period the cell displayed the typical response to osmotic stress. After slightly more than 2 h of recovery, another 0.5 M NaCl was added to the medium (LB plus 1 M NaCl), but this time the volume of the cytoplasm did not drop significantly whereas the *D* of GFP decreased. As anticipated the drop was not as pronounced as during the first osmotic upshift (Fig. 5, during the first upshift the D_{GFP} dropped from 3.2 $\mu m^2/s$ to 0.014 $\mu m^2/s$, while upon second exposure the drop was from 0.24 $\mu m^2/s$ to 0.03 $\mu m^2/s$).

Discussion

Observations on single-cell level

We have quantified the changes in cytoplasmic volume and GFP diffusion in osmotically-stressed at the single cell level. As noted by Wood (Wood, 1999), most of the traditional assays of cellular water content (such as determination of conductance of cell suspensions with a Coulter counter, comparison of water distribution within cell suspensions or examinations of light scattering by cells), provide population estimates and miss out cell to cell variations. Moreover, some of the measurements of cellular compositions are often performed on cell slurries or pellets, in which the cell physiology (limiting O_2 and nutrient availability) is far from optimal. Our experimental set up is free of such potential artifacts, allowing the probing of cells in a liquid, nutrient-rich medium at low cell density. Furthermore, we are able to probe the fate of single cells temporally.

Changes in cell physiology upon osmotic upshift

Upon exposure to osmotic upshift the *E.coli* cell exhibits instantaneous dehydration as the cytoplasm volume decreases (Fig. 2). While it was known previously, that such a challenge results in increase of macromolecule crowding

(Konopka *et al.*, 2007, Cayley *et al.*, 1991) and a slowing of protein mobility (van den Bogaart *et al.*, 2007, Konopka *et al.*, 2006), we now demonstrate that the decrease in diffusion coefficient occurs in parallel with the decrease in cell volume (Fig. 3).

Bacteria recovery from osmotic shock

The response of *E. coli* to increased medium osmolality is well studied. A model that divides in three phases the structural and physiological changes upon osmotic upshift has been proposed (Wood, 1999). In the first phase, that lasts up to 2 minutes after the osmotic challenge, the cell dehydrates and starts to take up K^+ ions to counter the loss of water. The time required for the cell to shrink is below 5 seconds (Koch, 1984, Wood, 1999); in fact, the cytoplasmic shrinkage may be even faster and happen within a second (which is the time resolution of our assay).

In the second phase, that extends up to 20-60 minutes after the osmotic upshock, the cell takes up glutamate (starting one minute after the onset of osmotic challenge (McLaggan *et al.*, 1994)), glycine-betaine and proline, and after 30 minutes the cell starts to synthesize trehalose (Dinnbier *et al.*, 1988). According to Dinniber and co-workers (Dinnbier *et al.*, 1988) already after 10 minutes from the start of osmotic challenge (in that case 1 Osm, which compares to our LB plus 0.5 M NaCl), the cells are partially recovered from the osmotic stress. This corroborates very well with data presented here as we observe that the most dramatic changes in cytoplasmic volume and GFP mobility take place within the first 10 minutes after upshift (Fig. 3). Indeed after this time the cells must have accumulated sufficient amounts of osmoprotectants as the subsequent recovery of cytoplasmic volume and protein mobility is much smaller in the time window from 10 to 60 minutes.

Following the model proposed by Wood (Wood, 1999), after 1 hour of osmotic stress the cellular physiology and structure are largely restored (cells resume growth), yet the cytoplasmic ion composition is altered. We note that just before the imposition of the second osmotic upshift (Fig. 5A min 131/0), the cell shape appears normal. Upon second exposure to osmotic stress, macromolecule diffusion and cytoplasm volume drop less than during the first osmotic challenge. This demonstrates that the cell is now primed to deal with increased osmolality, presumably by having accumulated large amounts of osmoprotectants.

Further experiments – physiology behind adaptation

We osmotically stress *E.coli* cells grown in LB medium, in which osmoprotectants are freely available. It would be of great interest to extend these studies to cells growing in media without osmoprotectants, *i.e.,* under conditions that obstruct the cellular response to osmotic upshift (van den Bogaart *et al.*, 2007, Mika *et al.*, 2010) and then determine temporally to which extent potassium ions, glycine betaine, proline, glutamate and others contribute to the restoration of cytoplasmic volume and macromolecule mobility. To further limit *E.coli* capabilities to adapt to osmotic stress one could use cells with impaired protein synthesis (e.g. by adding chloramphenicol) or devoid of the trehalose synthesis genes (Δ*otsA* and Δ*otsB* mutants).

At the single cell level the response of cells to increased osmolality is quite heterogenous within the probed population (*i.e.,* some cells exhibit a more dramatic drop in cytoplasmic volume or GFP diffusion coefficients than others). We believe that the observed spread in measured values reflect true differences in physiology (different levels of pre-accumulated trehalose or other compatible solutes) and/or stages of the cell cycle.

Correlation of cytoplasm volume and macromolecule diffusion

Macromolecule diffusion in the cytoplasm of bacteria is slower than in dilute aqueous solutions or than in eukaryotic cells (Mika & Poolman, 2011), which is rationalized by the high macromolecule crowding of prokaryotes. As the cells experience osmotic upshift and the cytoplasmic volume decreases, the crowding increases and it is not surprising that GFP mobility decreases. Consequently, as cells adapt to an increased osmolality of the external medium and the cytoplasmic volume is increased, the mobility increases. Our data suggest that the two parameters are highly correlated, at least when non-adapted cells are compared. In adapted cells, the macromolecular mobility can be relatively high despite a high crowding (Konopka et al 2009), which suggests that cells can adapt to a high crowding, possibly by exploiting the favorable properties of some co-solvents or other commodities in the cell. By inspecting the extents of decrease in cytoplasmic volume and GFP mobility, it seems that the initial drop in diffusion (within 10 min after osmotic upshift) is steeper than that of the decrease in cytoplasmic volumes. It is tempting to speculate that the decrease of diffusion is not solely caused by an increased macromolecule crowding, but also by the sudden dehydration. The abrupt efflux of water and increase of crowding may result in disturbance of the cytoplasmic structure, causing macromolecules to aggregate and possibly to (temporarily) unfold. This initial change in the cytoplasm structure might be short-lived, as macromolecule diffusion gradually restores (Fig. 3C).

Conclusions

Upon osmotic upshift water leaves the cytoplasm of *E.coli* instantaneously. This increases the macromolecule crowding and slows down (by two orders of magnitude) protein mobility. The cell has active mechanisms to adapt to high osmolality. Initially (within 10 minutes after the osmotic upshift), the cytoplasmic volume and GFP diffusion are largely restored. In the next hour, a slower phase of cytoplasmic rehydration and further restoration of protein mobility is observed. At the end of this phase, the cells have largely recovered and are primed with osmoportectants that render them less susceptible to a next osmotic challenge.

References

Baldwin, W. W. & P. W. Bankston, (1988) Measurement of live bacteria by Nomarski interference microscopy and stereologic methods as tested with macroscopic rod-shaped models. *Appl Environ Microbiol* **54**: 105-109.

Booth, I. R., M. D. Edwards, S. Black, U. Schumann & S. Miller, (2007) Mechanosensitive channels in bacteria: signs of closure? *Nat Rev Microbiol* **5**: 431-440.

Cayley, S., B. A. Lewis, H. J. Guttman & M. T. Record, Jr., (1991) Characterization of the cytoplasm of Escherichia coli K-12 as a function of external osmolarity. Implications for protein-DNA interactions *in vivo*. *J Mol Biol* **222**: 281-300.

Dinnbier, U., E. Limpinsel, R. Schmid & E. P. Bakker, (1988) Transient accumulation of potassium glutamate and its replacement by trehalose during adaptation of growing cells of Escherichia coli K-12 to elevated sodium chloride concentrations. *Arch Microbiol* **150**: 348-357.

Elowitz, M. B., M. G. Surette, P. E. Wolf, J. B. Stock & S. Leibler, (1999) Protein mobility in the cytoplasm of Escherichia coli. *J Bacteriol* **181**: 197-203.

Hamann, K., P. Zimmann & K. Altendorf, (2008) Reduction of turgor is not the stimulus for the sensor kinase KdpD of Escherichia coli. *J Bacteriol* **190**: 2360-2367.

Koch, A. L., (1984) Shrinkage of growing Escherichia coli cells by osmotic challenge. *J Bacteriol* **159**: 919-924.

Konopka, M. C., I. A. Shkel, S. Cayley, M. T. Record & J. C. Weisshaar, (2006) Crowding and confinement effects on protein diffusion *in vivo*. *J Bacteriol* **188**: 6115-6123.

Konopka, M. C., K. A. Sochacki, B. P. Bratton, I. A. Shkel, M. T. Record & J. C. Weisshaar, (2009) Cytoplasmic protein mobility in osmotically stressed Escherichia coli. *J Bacteriol* **191**: 231-237.

Konopka, M. C., Sochacki, K. A., Bratton, B. P., Shkel, I. A., Record, M. T., Weisshaar, J. C., (2009) Cytoplasmic protein mobility in osmotically stressed Escherichia coli. *J Bacteriol* **191**: 231-237.

Konopka, M. C., J. C. Weisshaar & M. T. Record, Jr., (2007) Methods of changing biopolymer volume fraction and cytoplasmic solute concentrations for *in vivo* biophysical studies. *Methods Enzymol* **428**: 487-504.

Kumar, M., M. Grzelakowski, J. Zilles, M. Clark & W. Meier, (2007) Highly permeable polymeric membranes based on the incorporation of the functional water channel protein Aquaporin Z. *Proc Natl Acad Sci U S A* **104**: 20719-20724.

McLaggan, D., J. Naprstek, E. T. Buurman & W. Epstein, (1994) Interdependence of K+ and glutamate accumulation during osmotic adaptation of Escherichia coli. *J Biol Chem* **269**: 1911-1917.

Mika, J. T. & B. Poolman, (2011) Macromolecule diffusion and confinement in prokaryotic cells. *Curr Opin Biotechnol* **22**: 117-126.

Mika, J. T., G. van den Bogaart, L. Veenhoff, V. Krasnikov & B. Poolman, (2010) Molecular sieving properties of the cytoplasm of Escherichia coli and consequences of osmotic stress. *Mol Microbiol* **77**: 200-207.

Potma, E. O., W. P. de Boeij, L. Bosgraaf, J. Roelofs, P. J. van Haastert & D. A. Wiersma, (2001) Reduced protein diffusion rate by cytoskeleton in vegetative and polarized dictyostelium cells. *Biophys J* **81**: 2010-2019.

Sleator, R. D. & C. Hill, (2002) Bacterial osmoadaptation: the role of osmolytes in bacterial stress and virulence. *FEMS Microbiol Rev* **26**: 49-71.

Swaminathan, R., C. P. Hoang & A. S. Verkman, (1997) Photobleaching recovery and anisotropy decay of green fluorescent protein GFP-S65T in solution and cells: cytoplasmic viscosity probed by green fluorescent protein translational and rotational diffusion. *Biophys J* **72**: 1900-1907.

van den Bogaart, G., N. Hermans, V. Krasnikov & B. Poolman, (2007) Protein mobility and diffusive barriers in Escherichia coli: consequences of osmotic stress. *Mol Microbiol* **64**: 858-871.

Wood, J. M., (1999) Osmosensing by bacteria: signals and membrane-based sensors. *Microbiol Mol Biol Rev* **63**: 230-262.

Wood, J. M., (2011) Bacterial Osmoregulation: A Paradigm for the Study of Cellular Homeostasis. *Annu Rev Microbiol* **65**: 215-238.

Wood, J. M., E. Bremer, L. N. Csonka, R. Kraemer, B. Poolman, T. van der Heide & L. T. Smith, (2001) Osmosensing and osmoregulatory compatible solute accumulation by bacteria. *Comp Biochem Physiol A Mol Integr Physiol* **130**: 437-460.

Zimmerman, S. B. & S. O. Trach, (1991) Estimation of macromolecule concentrations and excluded volume effects for the cytoplasm of Escherichia coli. *J Mol Biol* **222**: 599-620.

CHAPTER 6

TOWARDS IMAGING OF THE *E.COLI* ULTRASTRUCTURE WITH DUAL-COLOR SUPER-RESOLUTION PHOTO-ACTIVATED LOCALIZATION MICROSCOPY

Jacek T. Mika, Victor Krasnikov, Da Liu, Michiel Punter, Antoine van Oijen
& Bert Polman

We have set up dual-color photo-activated localization microscopy (PALM) to image bacteria at super-resolution. We have tested PA-GFP, Dronpa, mEos2 and eYFP as photo-activatable fluorophores and conclude that mEos2 and eYFP are most suitable for PALM. By expressing mEos2 and eYFP, either alone or fused to another protein, we obtain PALM reconstructions with up to 10 nm localization accuracy of the *E.coli* cytoplasm in paraformaldehyde fixed and osmotically-stressed cells. Imaging FtsZ-PA-GFP with our PALM set-up revealed features of the cytoskeleton that are well below the diffraction limit. We also present dual-color PALM of the bacterial cytoplasm and the nucleoid.

Introduction

The size of bacterial cells (typically in the orders of micrometers) renders them difficult to study with conventional light microscopy. Due to the diffraction limit of visible light (~ 250 nm) only limited detail of the cellular substructure is revealed. In the last ten years, several new approaches have been developed that aim at increasing the resolution of fluorescence light microscopy of living organisms (Huang *et al.*, 2009). They are often referred to as super-resolution microscopy techniques and can be divided in two categories. The first one is based on the non-linear optical response of fluorophores: Stimulated Emission Depletion Microscopy (STED) (Klar *et al.*, 2000). The second one is based on precise localization of single fluorescent molecules and examples are Stochastic Optical Reconstruction Microscopy (STORM, (Rust *et al.*, 2006)) and Photo-Activated Localization Microscopy (PALM, (Betzig *et al.*, 2006, Hess *et al.*, 2006)). Both STORM and PALM rely on the ability to localize with high (nanometer) precision the position of single emitting fluorophore molecules by fitting its image to a function (e.g. point spread function of the diffraction limited spot). Typically a large sequence of frames of well-separated, independent single molecules of fluorophores is acquired. The images are subsequently analyzed to obtain the positions of individual molecules and eventually a super-resolution image is reconstructed. To be able to record individual molecules in a densely labeled sample, photoswitchable fluorophores are required that reside most of the time in a dark state and can be brought to a bright state. In STORM usually organic dyes (*e.g.*, Cy5) are used and a single fluorophore can undergo several rounds of photoswitching. PALM, on the other hand, employs photoswitchable proteins (e.g. mEos) and these typically are photoactivated and then (irreversibly) bleached, i.e. a single molecule is imaged only once.

Most bacteria have a cell wall and, in Gram-negative bacteria, two membranes are present, which hinder the entry of fluorophores and prohibits the use of STORM in many instances. Genetically encoded fluorophores (fluorescent proteins) have the advantage that they can be produced inside the cell and targeted to desired locations by fusing them to other proteins. For example the

E.coli inner membrane or the nucleoid can be visualized by creating fluorescent protein fusions with proteins that normally reside in these structures, e.g. LacY – in the inner membrane and StpA in the nucleoid. Because of limitations in the use of synthetic fluorophores in bacterial cells, we choose to setup PALM rather than STORM or STED for our analysis of the ultrastructure of *E. coli*.

Since the first publication in 2006 (Betzig *et al.*, 2006, Hess *et al.*, 2006), PALM has been successfully used by several groups to visualize bacteria with super-resolution. The most frequently used photoswitchable protein is Eos and its derivatives (Wiedenmann *et al.*, 2004, McKinney *et al.*, 2009). Single-color PALM of cells expressing mEos has been used to visualize the chemotactic protein network (Greenfield *et al.*, 2009), to unravel the spatial organization of five different *E.coli* nucleoid associated proteins (Wang *et al.*, 2011) and to reveal features of the cytoskeletal structures formed by FtsZ (Fu *et al.*, 2010). The Moerner group has used eYFP in *Caulobacter crescentus* to visualize with super-resolution a bacterial actin-like protein MreB (Biteen *et al.*, 2008) and the nucleoid-associated protein Hu (Lee *et al.*, 2011).

We exploited PALM with the aim to determine substructures in *E. coli* under conditions of osmotic stress shock. Upon severe osmotic upshift molecule diffusion slows down dramatically (Mika *et al.*, 2010), the plasma membrane invaginates and the nucleoid and cytoplasm may change structure. We are aiming at probing the changes in the outer and inner membrane, cytoskeleton, nucleoid and cytoplasm under conditions of osmotic stress. Moreover, PALM allows the localization of supramolecular complexes such as the replication, transcription and translation machineries under conditions that the cells are (osmotically) challenged (work in progress).

Dual-color PALM (Shroff *et al.*, 2007) allows the simultaneous visualization of two substructures with nanometer precision and relate their localization in one and the same cells. We describe a home–built PALM microscope and new PALM software. For PALM, the photoactivatable proteins should be bright, efficiently photoswitchable and the emission “on/off ratio” should be high. Although proof-of principle of dual-color PALM in eukaryotic cells has been reported previously (Shroff *et al.*, 2007), prokaryotic cells pose their own challenge in high-resolution microscopy. mEos2 is very suitable for PALM in *E.coli*. However, finding a green partner for dual–color PALM proved more difficult. In this chapter, we present our studies to find a suitable pair of fluoresencent proteins for dual-colour PALM in *E.coli*. We visualize the cytoplasm and the nucleoid of *E. coli* with super-resolution using mEos2 and eYFP.

Materials and methods

Optical set up

PALM imaging was carried out on a home-built set up based on an Olympus IX-71 inverted microscope as schematically shown in Figure 1. Solid state lasers are from Coherent (Santa Clara, CA, USA): 405 nm (Cube 404 100 mW), 488 nm (Sapphire 488-100 CW), 514 nm (Sapphire 514-100CW) and 561 nm (Sapphire 561-100 CW). Software controlled shutters (Fig.1: SH1 to SH3) were used to achieve sequential illumination where a pulse of activation light (e.g. from the 405 nm laser for imaging of mEos2) preceeds illumination with the imaging laser (e.g. 561 nm for mEos2). Neutral-density filter wheels were used to attenuate laser power (Fig. 1: ND1 to ND3). Laser beams were collimated with lenses (Fig.1: L1 to L6). The laser beams were combined using dichroic mirrors (Fig. 1: DM1 and DM2) and directed through an additional lens (Fig. 1 L7) and the objective (100X, oil immersion, 1.49 NA TIRF objective, Olympus, UApo) onto the sample. Imaging was performed either in TIRF or quasi-TIRF mode. Fluorescence was recorded by an EM-CCD camera (Fig. 1, Hamamatsu, Japan, model C9100-13).

Data acquisition

For mEos2, PA-GFP and Dronpa, single color PALM data acquisition involved a sequence of illumination initiated by a short pulse of activation light (405 nm), followed by illumination with the appropriate excitation laser (561 nm laser for mEos2 and 488 nm for Dronpa and PA-GFP). Exposure times were usually 50 ms per frame. Typically, a sequence involved one activation frame that was followed by 5 or 10 imaging frames. The 405 laser power was adjusted to activate only a small sub-set of molecules at a time (typically 1 to 3 per sequence) and depended on the fluorophore (e.g. mEos2 was activated at ~100 times lower 405 nm laser power than PA-GFP). eYFP was imaged using continuous 514 nm laser excitation and typically 34 ms exposure time per frame (maximum frame rate for the camera). In dual-color PALM, *E. coli* cells expressing mEos2 and eYFP were used. The sample was first imaged in the red channel (mEos2) and subsequently in the green channel (eYFP). For dual-color PALM 3000 frames in each channel were collected.

PALM software

To obtain PALM reconstructions, the collected data were processed by home-written PALM software. The software analyzed individual frames and identified the presence of single molecules. The images of the identified single molecules were fitted to a 2D Gaussian function, resulting in the determination of their position, localization accuracy, full width at half maximum (FWHM), and amplitudes (brightness) of the 2D Gaussian functions. In the reconstructed image, each molecule is presented as a Gaussian distribution with the amplitude determined from the fit and dispersion equal to its localization accuracy.

Strains, growth and expression of fluorescent proteins

PALM imaging was performed on *E. coli* MG1655 (Mika *et al.*, 2010). The cells harboring plasmids with genes encoding photoswitchable proteins (see Plasmids Section for details) were grown from single colonies in Luria Broth (10 g/L Bactro-peptone (Beckton Dickinson), 5 g/L yeast extract (Becton Dickinson) and 10g/L NaCl (Merck)) supplemented with 100 μg/mL ampicillin (Sigma) at 37^{o} C in Erlenmeyer flasks with vigorous shaking (200 rpm). When the culture reached an OD_{600}=0.3-0.4, protein expression was induced with 0.002% (w/v) L-arabinose (Sigma) for all pBAD-based constructs or with 100 μM IPTG (Fermentas) for the pRSET-based plasmids. Expression was carried out for 0.5 to 2 hours as specified in Table 1. Subsequently, the cells were harvested and 1 mL of the cells was washed with NaPGCl medium (NaPGCl = 95 mM sodium phosphate, pH 7.0, 50 mM glucose plus 125 mM sodium chloride), which has an osmolality equal to that of LB.

Preparation of sample for microscopy

The cells were either imaged in the NaPGCl medium or fixed with 4% paraformaldehyde for 15 to 30 minutes. The 4% paraformaldehyde was prepared as described previously (Greenfield *et al.*, 2009) with the exception that NaPGCl medium was used instead of PBS. For osmotic upshift experiments, the cells were resuspended in NaPGCl medium supplemented with 1 M NaCl. A small aliquot of cell suspension (50-100µL) was placed on cover slips coated with 0.1% (w/v) poly-L-lysine solution (Sigma). Coated coverslips could be stored for up to two weeks. Once the cells had settled on the coverslip, they were imaged for periods of 20 min on average (but never exceeding one hour).

Plasmids

Plasmids with genes encoding photoswitchable fluorescent proteins are listed in Table 1. With the exception of pRSETb—Dronpa, a kind gift of Johan Hofkens, Leuven University, all constructs were prepared in pBAD-based vectors. The arabinose promoter is less leaky than the IPTG-based system, it is independent of the T7 polymerase, and is compatible with the MG1655 strain. By implementing the in-house developed duet expression system p2BAD (Birkner,

Plasmid name	**Induction time [hrs]**
pBAD—mEos2	2
pRSETb—Dronpa	1
pBAD—PA-GFP	2
pBAD—eYFP	2
pBAD—FtsZ-PA-GFP	0.5
pBAD-FtsZ-mEos2	0.5
p2BAD—StpA-eYFP—mEos2	2
P2BAD—Stpa-mEos2—eYFP	2

Table 1. Plasmids encoding fluorescent proteins used in this study. The relevant induction times for optimal functional expression are indicated.

2011), we were able to co-express two genes from a single plasmid.

mEos2 and PA-GFP genes were cloned into pBAD (pBAD-myc-his), using the original pRSETa plasmids (McKinney *et al.*, 2009, Patterson & Lippincott-Schwartz, 2002) from addgene.com (Cambridge, MA). The genes for StpA and FtsZ were inserted in pBAD, using *E. coli* MG1655 genomic DNA extract as a template for PCR amplification of the corresponding genes. The gene encoding eYFP was cloned from pNZ-OpuAA-eYFP-OpuABC and inserted in pBAD. Since this version of eYFP had a Thr instead of Tyr at position 203, we made the Thr-203 to Tyr-203 substitution as reported by the Moerner group (Lee *et al.*, 2011).

Results and discussion

Visualization of mEos2 in the cytoplasm of E. coli

We have imaged mEos2 expressed in the cytoplasm of *E.coli*; Figure 2 shows typical images of the cells. Fig. 2A and 2F are examples of PALM reconstructions, while Fig. 2B and 2G present the sum of all frames acquired during PALM imaging (and these are equivalent to conventional fluorescence microscopy images). The single molecules identified and localized by the PALM software differ in brightness, the full width at half maximum (FWHM) of the fitted (Gaussian) function and the error in fitting of their position (localization accuracy). For any analyzed image, the PALM software calculates this information, which is represented as histograms of molecule brightness (Fig. 2C and H), FWHM (Fig. 2D and I) and localization accuracy (Fig. 2E and J).

First, we imaged non–fixed cells under normal osmotic conditions (Fig. 2A-E). Since the cells are not fixed and the exposure time is relatively long (100 ms), mEos2 molecules diffuse and don’t appear as sharp, diffraction limited spots in the image. The distribution of FWHM is quite broad and has a maximum at around 500 nm (Fig. 2D). In contrast, when cells are fixed with 4% paraformaldehyde, the diffusion of mEos2 molecules in the cytoplasm is hindered and we observe sharp features in the PALM reconstruction (Fig. 2F). Moreover, even though the exposure time was 200 ms, the distribution of FWHM is less broad than that of the non-fixed cells (Fig. 2I vs. 2D) and has a maximum around 300

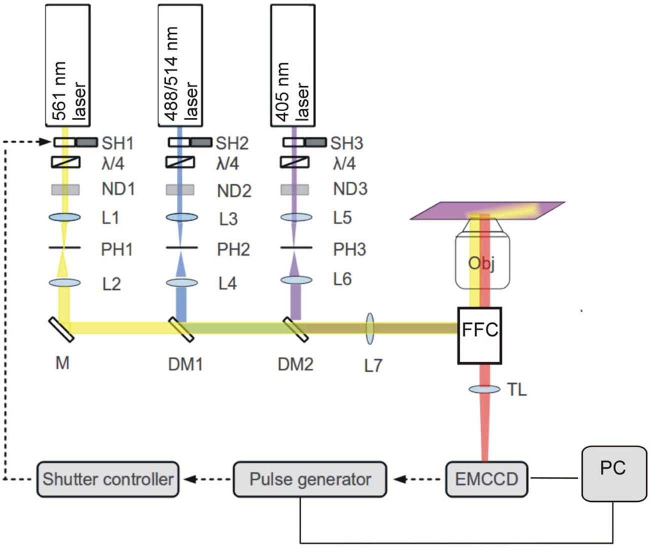

Figure 1. PALM microscope setup. Optical scheme of the microcope setup used for PALM imaging. SH1-SH3 – shutters; l/4- quarter waveplates; ND1-ND3 – neutral density filter wheels; L1-L7- lenses; PH1-PH3 – pinholes; M-mirror; DM1-2 – dichroic mirrors; FFC – fluorescence filter cubes; TL-tube lense; Obj-objective; EMCCD- the Electron Multiplying Charge Coupled Device camera, PC- computer.

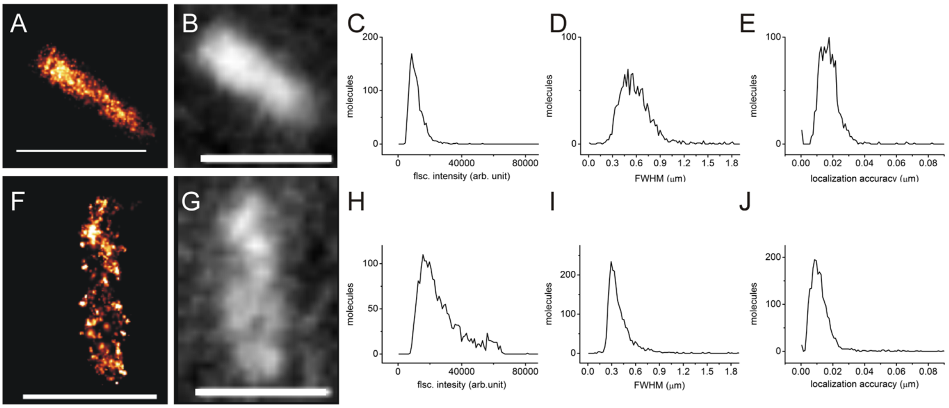

Figure 2. Escherichia coli expressing mEos2 in non-fixed and fixed cells. A-E: images and PALM statistics of a normal (not fixed) cell. F-J: images and PALM statistics of a paraformaldehyde-fixed cell. A: PALM reconstruction of nearly 1300 single molecules; B: the corresponding conventional fluorescence (diffraction-limited) image; exposure time 100 ms per frame. Similarly, F: PALM reconstruction of about 3000 molecules; and G: the corresponding conventional fluorescence image; exposure time 200 ms per frame. C and H: distributions of fluorescence intensities of the molecules; D and I: full width at half maximum (FWHM) for all localized molecules; E and J: localization accuracy of molecules. Scale bar 2 µm.

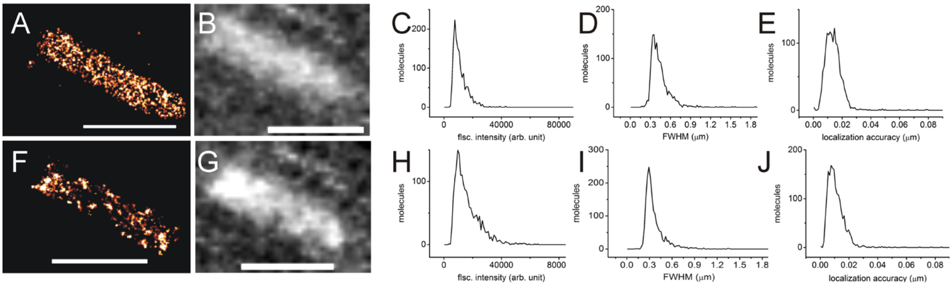

Figure 3. Escherichia coli expressing mEos2: the effects of osmotic upshift. A-E: images and PALM statistics of a (non-fixed) cell under normal osmotic conditions. F-J: images and PALM statistics of the same cell after exposure to osmotic upshift (1M NaCl). A: a PALM reconstruction of about 1100 mEos2 molecules; B: the corresponding conventional fluorescence image. F: a PALM reconstruction of about 1400 molecules; G: the corresponding conventional fluorescence image. C-E and H-J like in Fig.2. Scale bar 2 µm.

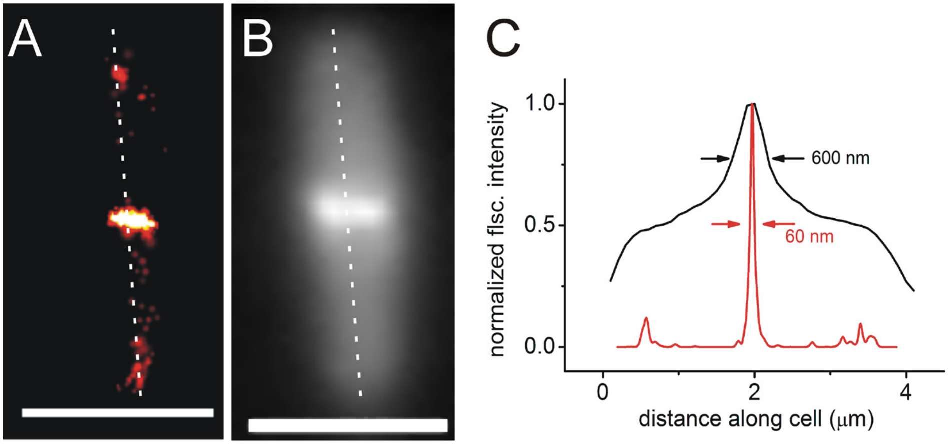

Figure 4. Escherichia coli expressing FtsZ-PA-GFP. A: PALM reconstruction of an *E. coli* cell expressing FtsZ-PA-GFP; about 700 molecules have been used for the image reconstruction. B: the corresponding conventional fluorescence image. Scale bar 2 µm. C: Fluorescence intensity distribution along the dashed line for the PALM reconstruction (red) and the wide-field image (black). The arrows indicate the width of the peaks (FWHM).

nm which is close to what is expected for a diffraction limited spot. As a result, the localization accuracy of the fixed cells is better (around 10 nm Fig. 2J) than in the case of non-fixed cells (around 20 nm Fig. 2E).

The PALM reconstructions of mEos2 in the cytoplasm of *E. coli* are similar to those reported by others (Fu *et al.*, 2010). We observe that the mEos2 molecules are evenly distributed throughout the cytoplasm, which is more apparent for the non-fixed than the fixed cells.

In fact, in the PALM reconstruction of the fixed cells (Fig. 2F,) the mEos2 molecules appear to be more clustered and are less abundant in some regions of the cytoplasm than in others. We cannot unequivocally state whether this apparent substructure is real, because the acquired PALM data is under-sampled (only 3000 molecules were localized) and the cells have been fixed with paraformaldehyde, both of which might lead to artifacts.

Paraformaldehyde treatment is a common procedure for sample preparation in PALM imaging (Betzig *et al.*, 2006, Biteen *et al.*, 2008, Fu *et al.*, 2010, Greenfield *et al.*, 2009). The fixation method yields sharper images of the individual molecules and enhances the localization precision (Fig. 2). However, there is a potential risk that artifactual substructures are generated. We therefore also determined the localization of mEos and other fluorophores in osmotically-stressed cells.

Figure 3 shows PALM reconstructions of an *E. coli* cell before and after exposure to severe osmotic upshift (addition of 1M NaCl to the basal medium). Upon exposure to high osmolality, the cell loses its typical rod-like shape. Due to water loss from cytoplasm, the (macro)molecule crowding of the cell increases and diffusion slows down. This is reflected in the FWHM distributions of localized molecules, *i.e.*, after exposure to increased salinity the maximum shifts towards 300 nm (Fig. 3 D vs 3I), which is indicative of loss of mobility of the molecules. Moreover, the localization accuracy increased (Fig. 3E vs 3J), similar to what was observed upon fixation with paraformaldehyde (Fig. 2). In the osmotically-stressed cells, the mEos2 molecules also do not seem evenly distributed throughout the cytoplasm (Fig. 3F).

Although the molecular basis of fixation and increase of macromolecule crowding as a result of osmotic upshift are different, they have a similar effect on their mobility in cells. They can be both used as means for limiting molecule diffusion to obtain better resolved PALM reconstructions.

PALM allows visualizing of structures that are below the diffraction limit of light microscopy

FtsZ is a bacterial, tubulin-like protein that is involved in cell division and forms a ring-like structure under the plasma membrane. The rings have structural elements of sizes that are below the diffraction limit of conventional light microscopy. By creating a FtsZ-mEos2 fusion, Fu and colleagues (Fu *et al.*, 2010) have visualized the rings with 35 nm resolution. According to their PALM study the thickness of the FtsZ rings is around 110 nm.

To validate our PALM set-up, we have visualized the FtsZ rings. We have created FtsZ-mEos2 and FtsZ-PA-GFP constructs (Table 1). Figure 4 shows a representative image of FtsZ-PA-GFP. The PALM reconstruction (Fig. 4A) shows a more defined structure than the corresponding diffraction limited image (Fig. 4B).

The Z-ring, located in the middle of the (dividing) *E. coli* cell, has a width of about 60 nm (Fig. 4C). The same structure appears 600 nm wide in the diffraction limited image. Clearly, our PALM set up is able to visualize cellular substructures well below the diffraction limit.

It should be noted that fusions of FtsZ with GFP are detrimental to the protein's function and can be lethal for the cell (Fu *et al.*, 2010). In order to visualize FtsZ fusions, a significant amount of wild type FtsZ needs to be present as well. In our experiments, the FtsZ-mEos2 and FtsZ-PA-GFP proteins were expressed from a high copy plasmid (pBAD, containing the pBR322_Ori) at relatively high concentrations of the inducer. Even though short induction times were used (30 minutes, see Table 1), the amount of fusion proteins was probably much higher than that of wildtype FtsZ. Accordingly, the experiments performed with FtsZ fused with either PA-GFP or mEos2 were not very reproducible. We were not able to acquire any images of cells with FtsZ-mEos2 with the protein localized at the mid-cell (not shown) as is expected (Fu *et al.*, 2010). Presumably, we were unable to precisely control the ratio of wildtype of FtsZ over FtsZ-mEos2 (or FtsZ–PA-GFP).

Experiments with green fluorescent photo-switchable proteins

Our goal was to establish dual-color PALM in *E. coli*. While mEos2 turned out to be an excellent fluorophore for PALM (efficient photoswitching and high molecular brightness), finding a suitable, spectrally distinguishable partner proved challenging. Our initial trials focused on Dronpa (Table 1). Upon 405 nm illumination, Dronpa converts from a dark to a bright state (emitting fluorescence upon 488 nm excitation); illumination at 488 nm drives the protein back to a dark state (Habuchi *et al.*, 2006). While we were able to observe 405 nm-induced photoswitching of the purified protein in solution at relatively high concentrations (not shown), the photophysical behavior of Dronpa in the cytoplasm of *E. coli* was hard to control. We were not able to control the photoswitching with the 405 nm and 488 nm lasers due to a very fast (likely thermally-activated) transition from the dark to a bright state. Since the lifetime of Dronpa in the dark state was too short, we were not able to adjust the fluorescence “on/off ratio“ to obtain frames with desired low density of single molecules, which is necessary to perform PALM.

We have also tested PA-GFP (Table 1). This photoswitchable protein is reported to initially reside in a dark state (Patterson & Lippincott-Schwartz, 2002), with very low fluorescence upon 488 nm excitation. Illumination with 405 nm increases the proteins fluorescence upon 488 nm excitation approximately 100-fold. In our experiments in *E. coli*, the fluorophore appeared to be in a bright state. In order to obtain frames with well-separated single molecules, we first had to photobleach a significant portion of fluorescent PA-GFP. As a result, relatively few PA-GFP molecules could be photo-switched to acquire sufficient datasets for PALM. We occasionally observed that when the cells were left dehydrated, the photoswitching propensity of PA-GFP suddenly increased. These non-physiological conditions allowed photoswitching of many molecules but the experiments were not pursued further. Clearly, the photophysics of PA-GFP is more complex in the crowed cytoplasm of *E. coli* than in dilute aqueous solutions.

eYFP is suitable for PALM

The Moerner group has reported super-resolution imaging with eYFP in *Caulobacter crescentus* (Biteen *et al.*, 2008, Lee *et al.*, 2011). Since eYFP can be spectrally distinguished from photoconverted mEos2, it provided an attractive alternative for dual-color PALM experiments. We expressed eYFP in the cytoplasm of *E. coli* (seeTable 1) and were able to acquire sufficient quality data sets to obtain PALM reconstructions (Fig. 5). In order to excite the fluorophore closer to its absorption maximum, eYFP was continuously exited with the 514 nm laser and fluorescence was collected between 530 and 560 nm, and the 405 nm laser was not used. The excitation and emission of eYFP are red shifted as compared to the other “green” photoswitchable proteins (Dronpa and PA-GFP). This red-shifted excitation and emission significantly reduces background signals originating from autofluorescence and improved the signal-to-noise ratio. Upon expression, eYFP is initially in a bright state and individual molecules were not distinguishable. Therefore, the sample was illuminated with relatively intense (1-2 kW/cm^2) 514 nm laser light and eYFP was driven into a dark state until well separated molecules were observable. Starting from this low fluorescence level, the majority of eYFP molecules remained in a dark state/photobleached state and only a few molecules per frame were converted into a bright state. Long acquisition up to 3000 frames without completely depleting the pool of bright eYFP was possible. Under such conditions, we were able to obtain PALM reconstructions of about 1000 molecules in a cell with satisfactory localization precision below 20 nm (Fig. 5). As expected, eYFP appeared mostly homogenously distributed throughout the cytoplasm (Fig. 5A). The apparent higher abundance in the middle of the cell (along the long axis of the cell; Fig. 5A) is likely an artifact of undersampling. Although eYFP is not as good a fluorophore for PALM as mEos2 (lower signal-to-noise ratio and less control over photoswitching), it is still feasible to acquire sufficient data for PALM reconstruction.

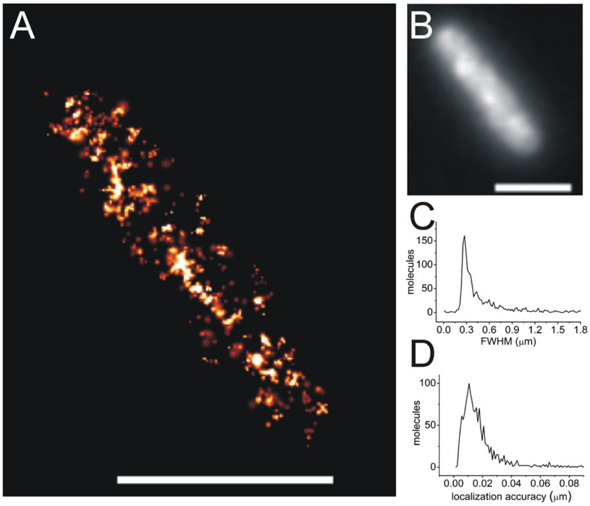

Figure 5. Escherichia coli expressing eYFP. *E. coli* cells fixed with paraformaldehyde and expressing eYFP. A: PALM reconstruction of nearly 1000 eYFP molecules; B: the corresponding conventional fluorescence image. Scale bar 2 μm. C: Distribution of FWHM of the localized molecules; D: localization accuracy of the molecules.

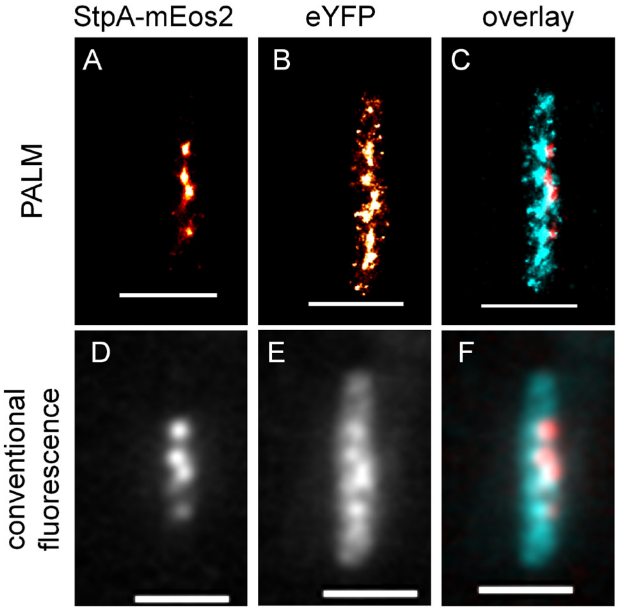

Figure 6. Dual-color PALM reconstructions of Escherichia coli expressing StpA-mEos2 and eYFP in paraformaldehyde-fixed cells. PALM reconstruction of about 5700 StpA-mEos2 molecules (A) and about 2400 eYFP molecules (B). C: Overlay of PALM reconstructions; D,E: the corresponding conventional fluorescence images. F: overlay of conventional fluorescence images. StpA-mEos false-colored red; eYFP false-colored cyan. Scale bar 2 μm.

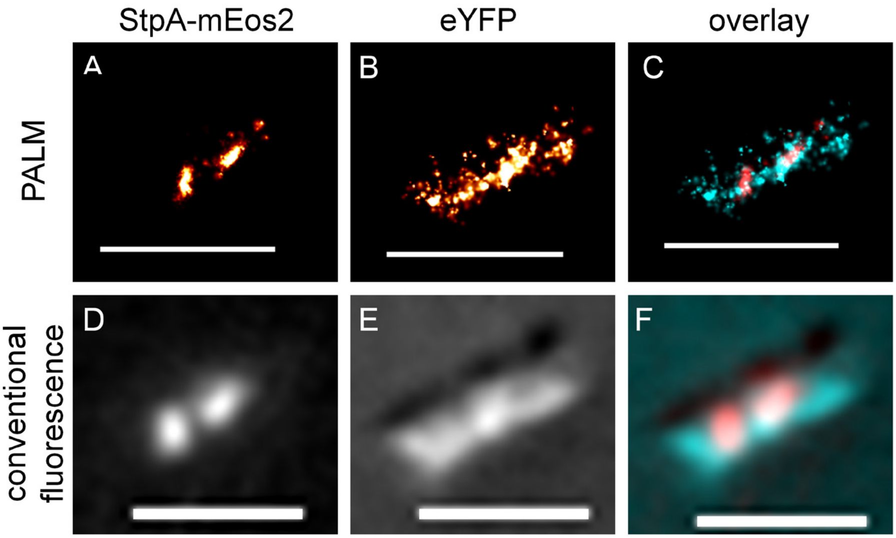

Figure 7. Dual-color PALM reconstructions of Escherichia coli expressing StpA-mEos2 and eYFP in paraformaldehyde-fixed cells. PALM reconstruction of about 2700 StpA-mEos2 molecules (A) and about 1800 eYFP molecules (B). Panels labeled like in Figure 6. Scale bar 2 µm.

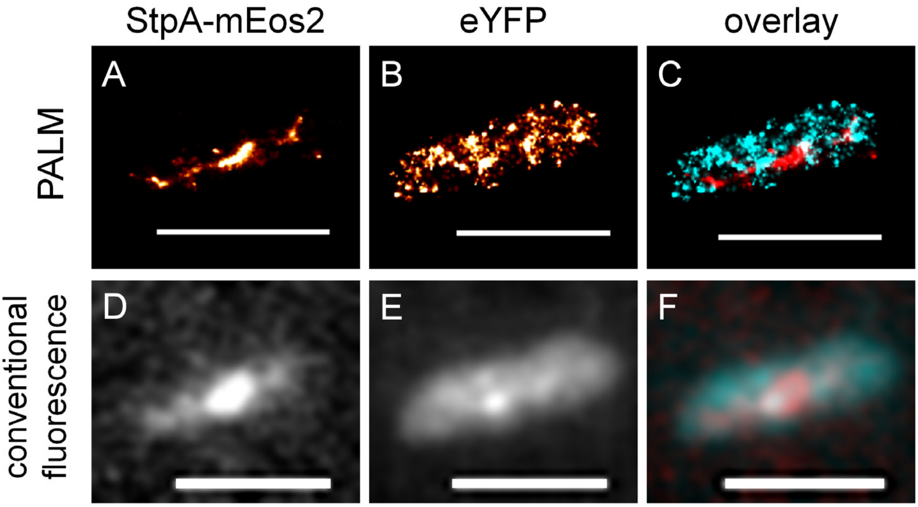

Figure 8. Dual-color PALM reconstructions of Escherichia coli expressing StpA-mEos2 and eYFP in osmotically-stressed cells. PALM reconstruction of about 700 StpA-mEos2 molecules (A) and about 300 eYFP molecules (B). Panels labeled like in Figure 6. Scale bar 2 µm.

Dual color PALM in E. coli

Having found satisfactory and spectrally distinguishable fluorophores that allow single-color PALM in *E. coli*, we performed dual-color PALM. While dual-color PALM was demonstrated previously in eukaryotic cells (Shroff *et al.*, 2007), until recently (Wang *et al.*, 2011) there were no studies implementing dual-color super-resolution microscopy in bacteria. For dual-color PALM, we have used a duet expression system (p2BAD) that allows the expression of two separate genes from one plasmid (see Materials and Methods section). We have expressed one fluorophore in the cytoplasm and the other as a fusion protein with a *E. coli* nucleoid associated protein (NAP) StpA. Both combinations were created, with StpA fused to mEos2 and eYFP alone and *vice-versa* (Table 1).

We were able to obtain dual color PALM reconstructions (Fig.6-12). In general mEos2 gave better reconstructions than eYFP. Since we did not align the images by implementing fiducials such as gold nano-particles (Greenfield *et al.*, 2009), our overlaid images are most likely somewhat misaligned (see Fig. 8).

Upon exposure of the cells to osmotic upshift, a loss of rod-like shape of the cytoplasm was observed, which is consistent with our single-color PALM reconstructions (Fig. 3). The cytoplasmically expressed protein in shocked cells is not as homogenously distributed throughout the cytoplasm as was the case in non-stressed cells (Fig. 6-12). We observe different morphologies of the localization of the StpA protein. This protein appears concentrated in the middle of the cell where it forms from one (Fig. 6A, 12B) up to three (Fig. 7A) large clusters. In one case, StpA was more evenly distributed throughout the cell (Fig. 11B) with higher abundance at cell poles. The structures formed by the nucleoid in the cytoplasm are dynamic and change with the cell cycle (Robinow & Kellenberger, 1994); the different morphologies we see might thus reflect different stages of the cell cycle.

Our PALM reconstructions resemble to a great extent those reported for StpA by the Zhuang group (Wang *et al.*, 2011) and for another nucleoid as-

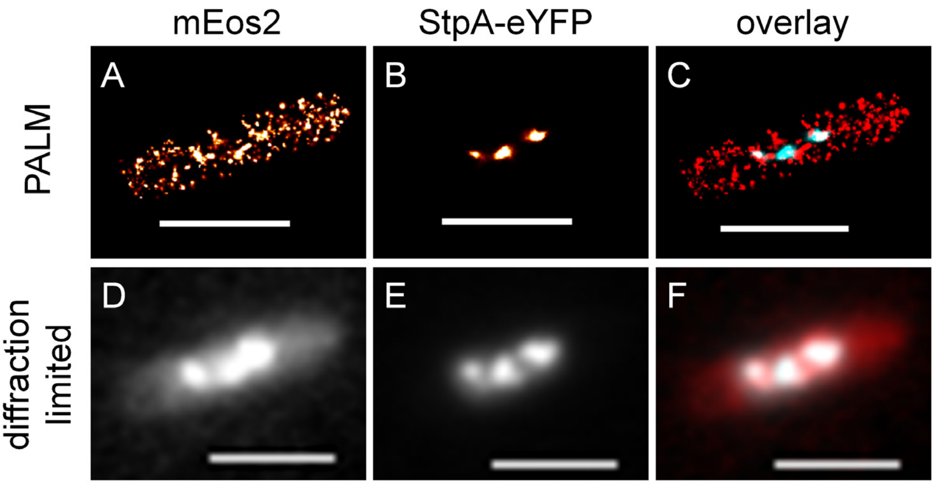

Figure 9. Dual-color PALM reconstructions of Escherichia coli expressing mEos2 and StpA-eYFP in paraformaldehyde-fixed cells. PALM reconstruction of ~1450 mEos2 molecules (A) and of ~2800 StpA-eYFP molecules (B). C: Overlay of PALM reconstructions; D, E: the corresponding conventional fluorescence images. F: Overlay of wide-field images. mEos2 false-colored red, StpA-eYFP false-colored cyan. Scale bar 2 µm.

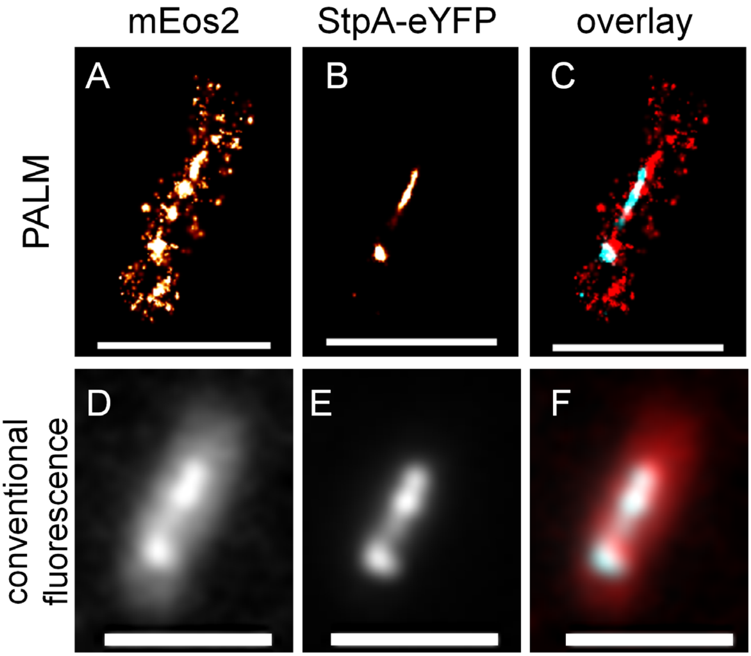

Figure 10. Dual-color PALM reconstructions of Escherichia coli expressing mEos2 and StpA-eYFP in paraformaldehyde-fixed cells. PALM reconstruction of ~1300 mEos2 molecules (A) and of ~1500 StpA-eYFP molecules (B). Panels labeled like in Figure 9. Scale bar 2 µm.

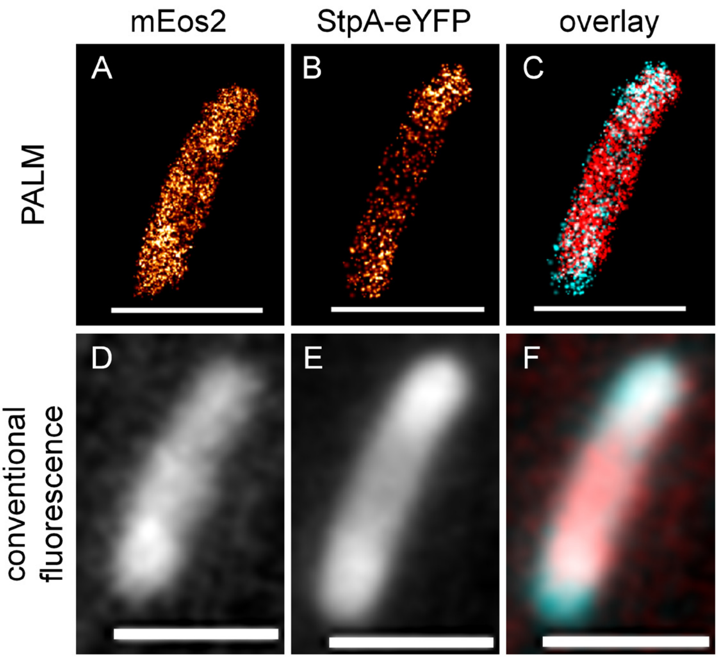

Figure 11. Dual-color PALM reconstructions of Escherichia coli expressing mEos2 and StpA-eYFP in osmotically-stressed cell. PALM reconstruction of ~3900 mEos2 molecules (A) and of 850 StpA-eYFP molecules (B). Panels labeled as in Figure 9. Scale bar 2 µm.

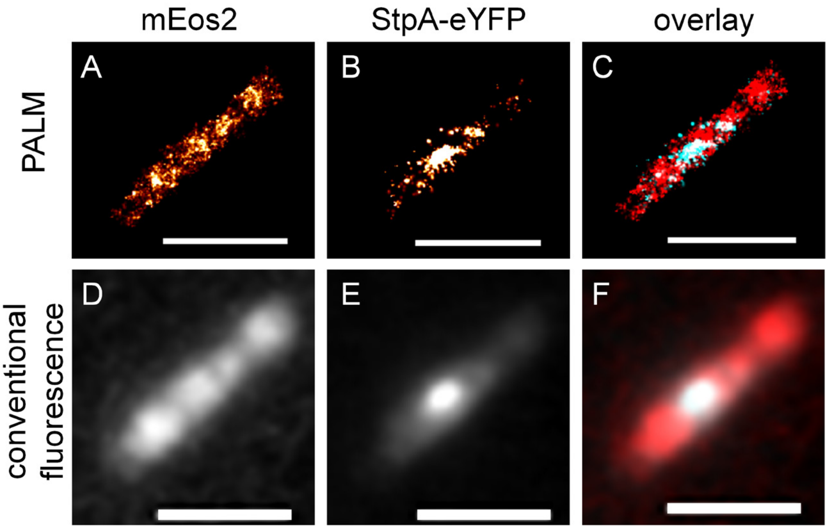

Figure 12. Dual-color PALM reconstructions of Escherichia coli expressing mEos2 and StpA-eYFP in an osmotically-stressed cell. PALM reconstruction of ~ 4500 mEos2 molecules (A) and of ~1600 StpA-eYFP molecules (B). Panels labeled like in Figure 9. Scale bar 2 µm.

sociated protein - HU in *C. crescentus* by the Moerner group (Lee *et al.*, 2011). These studies report a slightly more homogenous distribution of the nucleoid associated proteins throughout the nucleoid than we observe. It is possible that in our PALM reconstructions the single molecules of the data frames or not sufficiently separated, which is especially pronounced in the case for StpA-eYFP (Fig. 10B and 11B).

Limitations of PALM

To obtain good quality, meaningful PALM reconstructions, images of single, well-separated molecules are necessary in the frames that built up a data set. This requires careful tuning of the activation and fluorescence excitation, which can be difficult to achieve when structures are labeled very densely (e.g the nucleoid, StpA fusions with mEos2 or eYFP, Fig. 6-12) or when photoswitchable proteins are overexpressed. Another consideration is undersampling. Since PALM reconstructions are composed of images of single molecules, visualized object always appear granular. In the case of objects that have well defined shapes (like the polymer formed by the FtsZ protein), visualization of only a small subset of molecules can be sufficient to probe the structure.

However, structurally less well-defined objects, such as the cytoplasm or the nucleoid, can easily appear to have a well-defined structure due to insufficient imaging of molecules. This undersampling problem should be taken into account when imaging these structures. By analyzing multiple cells and/or by performing Monto Carlo-type simulations, one can get an estimate of whether or not undersampling has affected the reconstructions.

Conclusions

We have succeeded in performing dual-color PALM in *E.coli.* Of the different fluorophores tested, mEos2 and eYFP proved most suitable for dual-color PALM reconstruction of the cellular substructures. However, there is still a need for improvement of pairs of photoswitchable fluorophores.

References

Betzig, E., G. H. Patterson, R. Sougrat, O. W. Lindwasser, S. Olenych, J. S. Bonifacino, M. W. Davidson, J. Lippincott-Schwartz & H. F. Hess, (2006) Imaging intracellular fluorescent proteins at nanometer resolution. *Science* **313**: 1642-1645.

Birkner, J. P., Poolman B., Kocer A., (2011) Heterooligometization of a homooligomeric membrane protein *in vivo*. *submitted*.

Biteen, J. S., M. A. Thompson, N. K. Tselentis, G. R. Bowman, L. Shapiro & W. E. Moerner, (2008) Super-resolution imaging in live Caulobacter crescentus cells using photoswitchable EYFP. *Nat Methods* **5**: 947-949.

Fu, G., T. Huang, J. Buss, C. Coltharp, Z. Hensel & J. Xiao, (2010) *In vivo* structure of the *E. coli* FtsZ-ring revealed by photoactivated localization microscopy (PALM). *PLoS One* **5**: e12682.

Greenfield, D., A. L. McEvoy, H. Shroff, G. E. Crooks, N. S. Wingreen, E. Betzig & J. Liphardt, (2009) Self-organization of the Escherichia coli chemotaxis network imaged with super-resolution light microscopy. *PLoS Biol* **7**: e1000137.

Habuchi, S., P. Dedecker, J. Hotta, C. Flors, R. Ando, H. Mizuno, A. Miyawaki & J. Hofkens, (2006) Photo-induced protonation/deprotonation in the GFP-like fluorescent protein Dronpa: mechanism responsible for the reversible photoswitching. *Photochem Photobiol Sci* **5**: 567-576.

Hess, S. T., T. P. Girirajan & M. D. Mason, (2006) Ultra-high resolution imaging by fluorescence photoactivation localization microscopy. *Biophys J* **91**: 4258-4272.

Huang, B., M. Bates & X. Zhuang, (2009) Super-resolution fluorescence microscopy. *Annu Rev Biochem* **78**: 993-1016.

Klar, T. A., S. Jakobs, M. Dyba, A. Egner & S. W. Hell, (2000) Fluorescence microscopy with diffraction resolution barrier broken by stimulated emission. *Proc Natl Acad Sci U S A* **97**: 8206-8210.

Lee, S. F., M. A. Thompson, M. A. Schwartz, L. Shapiro & W. E. Moerner, (2011) Super-resolution imaging of the nucleoid-associated protein HU in Caulobacter crescentus. *Biophys J* **100**: L31-33.

McKinney, S. A., C. S. Murphy, K. L. Hazelwood, M. W. Davidson & L. L. Looger, (2009) A bright and photostable photoconvertible fluorescent protein. *Nat Methods* **6**: 131-133.

Mika, J. T., G. van den Bogaart, L. Veenhoff, V. Krasnikov & B. Poolman, (2010) Molecular sieving properties of the cytoplasm of Escherichia coli and consequences of osmotic stress. *Mol Microbiol* **77**: 200-207.

Patterson, G. H. & J. Lippincott-Schwartz, (2002) A photoactivatable GFP for selective photolabeling of proteins and cells. *Science* **297**: 1873-1877.

Robinow, C. & E. Kellenberger, (1994) The bacterial nucleoid revisited. *Microbiol Rev* **58**: 211-232.

Rust, M. J., M. Bates & X. Zhuang, (2006) Sub-diffraction-limit imaging by stochastic optical reconstruction microscopy (STORM). *Nat Methods* **3**: 793-795.

Shroff, H., C. G. Galbraith, J. A. Galbraith, H. White, J. Gillette, S. Olenych, M. W. Davidson & E. Betzig, (2007) Dual-color superresolution imaging of genetically expressed probes within individual adhesion complexes. *Proc Natl Acad Sci U S A* **104**: 20308-20313.

Wang, W., G. W. Li, C. Chen, X. S. Xie & X. Zhuang, (2011) Chromosome organization by a nucleoid-associated protein in live bacteria. *Science* **333**: 1445-1449.

Wiedenmann, J., S. Ivanchenko, F. Oswald, F. Schmitt, C. Rocker, A. Salih, K. D. Spindler & G. U. Nienhaus, (2004) EosFP, a fluorescent marker protein with UV-inducible green-to-red fluorescence conversion. *Proc Natl Acad Sci U S A* **101**: 15905-15910.

CHAPTER 7

STRUCTURAL BASIS FOR THE ENHANCED ACTIVITY OF CYCLIC ANTIMICROBIAL PEPTIDES: THE CASE OF BPC194

Jacek T. Mika*, Gemma Moiset*, Anna D. Cirac, Lidia Feliu, Eduard Bardají, Marta Planas,
Durba Sengupta, Siewert J. Marrink & Bert Poolman

Biochimica et Biophysica Acta: Biomembranes 2011, **1808**: 2197-2205

* These authors contributed equally

We report the molecular basis for the differences in activity of cyclic and linear antimicrobial peptides. We iteratively performed atomistic molecular dynamics simulations and biophysical measurements to probe the interaction of a cyclic antimicrobial peptide and its inactive linear analogue with model membranes. We establish that, relative to the linear peptide, the cyclic one binds stronger to negatively-charged membranes. We show that only the cyclic peptide folds at the membrane interface and adopts a beta-sheet structure characterized by two turns. Subsequently, the cyclic peptide penetrates deeper into the bilayer while the linear peptide remains essentially at the surface. Finally, based on our comparative study, we propose a model characterizing the mode of action of cyclic antimicrobial peptides. The results provide a chemical rationale for enhanced activity in certain cyclic antimicrobial peptides and can be used as a guideline for design of novel antimicrobial peptides.

Introduction

Antimicrobial peptides (AMPs) are currently in the spotlight as potential candidates to overcome bacterial resistance to conventional antibiotics. These peptides are natural weapons produced by a variety of organisms, including insects, animals and plants (Brogden *et al.*, 2003, Lehrer & Ganz, 1999). While displaying a wide spread in primary structures, most antimicrobial peptides exhibit common basic features (Dathe *et al.*, 2004, Jenssen *et al.*, 2006, Zasloff, 2002). The linear α-helical peptides have been shown to be unstructured in water and adopt a secondary structure upon association with the membrane (Huang, 2000, van den Bogaart *et al.*, 2008). Though acquiring structure upon membrane binding is an important feature of these AMPs, short peptides lacking a well-defined secondary structure are also active (Houston *et al.*, 1998). Cyclic AMPs are amongst the most effective antimicrobial agents (Davies, 2003, Epand & Vogel, 1999) and some members of the family have been shown to adopt a structure even in water (Ganz, 2003). One of the best studied examples is gramicidin S, whose structure in aqueous media, an anti-parallel β-sheet characterized by two turns, is important for its activity (Kato & Izumiya, 1977). Comparative studies between related peptides with differing activities, though not yet been undertaken, would help us rationalize the essential structural properties vital for function and will help us design more potent antimicrobial peptides.

Besides acquiring structure at the membrane interface, the partitioning behavior of the peptides, i.e. the membrane-aqueous medium partition coefficient and the membrane penetration depth also contribute to their efficacy and action and selectivity (Toke, 2005). In fact, the local concentrations of AMPs in the membrane can be up to 10,000 times higher than in the aqueous phase (Melo *et al.*, 2009), therefore the understanding of partitioning behaviour is of importance to unravel mechanisms of action of these peptides. Again, undertaking comparative studies would help us distinguish between essential and non-essential differences in partitioning and help to extract only the critical features.

The focus of our work is a cyclic peptide, BPC194 [c(KKLKKFKKLQ)], which, from a library of *de novo* designed cyclic decapeptides, proved most active against plant pathogens such as *Erwinia amylovora, Pseudomonas syringae* and *Xanthomonas vesicatoria* (Monroc *et al.*, 2006a, Monroc *et al.*, 2006b); its linear analogue is poorly active. Here, we present a combined MD and biophysical study of the cyclic peptide interacting with anionic lipid bilayers to understand its mechanism of action. The linear analogue, BPC193 has been studied to contrast the behavior of the two related peptides and extract the molecular basis for antimicrobial activity. We show how the cyclic and linear peptides differ both in their partitioning behavior and their folding state upon interaction with membranes. We speculate that these differences are related to differences in pore forming activity.

Materials and methods

Biophysical Characterization

Materials

The 4-(2-hydroxyethyl)piperazine-1-ethanesulfonic acid (HEPES) and 2-amino-2-(hydroxymethyl)-1,3-propanediol (Tris-HCl) were from Roche Diagnostics GmbH (Germany), sodium chloride, sodium fluoride and Triton-X100 were from Merck (Germany). Phospholipids 1,2-dioleoyl-sn-glycero-3-phosphatidylcholine (DOPC), 1,2-dioleoyl-sn-glycero-3-phosphatidylglycerol (DOPG) and 1,2-dioleoyl-sn-glycero-3-phosphatidyl-ethanolamine (DOPE) were from Avanti Polar Lipids.

Peptide synthesis

Decapeptides investigated in this study (Table 1) varied in the type of aromatic aminoacid at position 6 and included cyclic analogues: BPC194, BPC294 and BPC418, together with their linear counterparts: BPC193, BPC293 and BPC417. All of them were synthesized by solid phase peptide synthesis as described in Supplementary Data (Mika *et al.,* 2011).

Liposome preparation

Liposomes for calcein dequenching

Liposomes were prepared as described previously (Koçer *et al.*, 2005). Briefly, liposomes at a final concentration of 1mM of lipid molecules were prepared by rehydration of a dried lipid film with 100 mM calcein-NaOH in 10 mM HEPES, pH 7.0. The vesicles were then subjected to five cycles of flash freezing in liquid nitrogen and rapid thawing at 50°C. Subsequently, the liposomes were sonicated (5 × 10 sec. pulses at 75% amplitude with a Sonics Vibra Cell VCX 130 sonicator) to obtain unilamellar vesicles. Liposomes were separated from the non-encapsulated dye by size exclusion chromatography (Sephadex G-75, GE Healthcare). The column was equilibrated and eluted with 10 mM HEPES, pH 7.0, plus 150 mM NaCl, henceforth refered as buffer A.

Liposomes for Circular Dichroism (CD)

Liposomes were prepared similarly as described for the calcein dequenching experiments except that the dried lipid film was rehydrated with 10 mM sodium phosphate, pH 7.0, plus 150 mM NaF to a final concentration of 25 mM lipids. Sodium chloride was replaced by sodium fluoride to reduce the noise levels at wavelengths < 200 nm, which is caused by chloride ions. Furthermore, liposomes were extruded through a 30 nm polycarbonate filter (Whatman International Ltd, UK), instead of sonication, to obtain a more homogenous sample.

Liposomes for binding and tryptophan environment assays

Liposomes were prepared by rehydration of DOPG phospholipid films in buffer A to a final concentration of 25 mM and subsequently extruded through a 200 nm polycarbonate filter.

Calcein dequenching

The calcein dequenching assay was performed as reported previously (Koçer *et al.*, 2005). A 20 µl sample of liposomes (1mM of lipid), obtained as described in section 2.1.3.1 of Materials and Methods, was placed in 3 ml of buffer A, which yielded a final concentration of 6.7 µM of lipid in the cuvette. The membrane permeabilizing activity of the peptide was followed by measuring the increase in fluorescence (calcein dequenching), resulting from vesicle leakage after peptide addition addition (0-52 µM). Fluorescence emission was monitored at 520 ± 5 nm (excitation at 485 ± 2 nm) in a Cary Eclipse Fluorescence Spectrophotometer (Varian Inc.). The release of the calcein was calculated as a percentage of the total amount present in the liposomes:

$$\%\,Release = (I - I_0)/(I_{100} - I_0) \times 100,$$

where I is the measured fluorescence intensity at a given time, I_0 is the initial background fluorescence intensity and I_{100} is the fluorescence intensity upon complete lysis of the liposomes, which was elicited by adding Triton X-100 (0.06% final concentration).

Circular dichroism

Far-UV circular dichroism spectra were recorded on a Jasco J-815 CD spectrometer (Jasco, UK) between 190 and 250 nm at room temperature and scanning every 1 nm, using a quartz cell of 1 mm path length. The peptide at 0.15 mM was titrated with small aliquots (1 to 10 µL) of DOPG liposomes at a concentration of 25 mM. 2,2,2-Trifluoroethanol (TFE, Janssen Chimica) was used as a secondary structure inducer. The spectra were corrected for the absorption of buffer and vesicles.

Peptide environment probed with tryptophan fluorescence

The tryptophan analogues (BPC417 and BPC418) were placed in a quartz cuvette in buffer A at 2 µM and their fluorescence was monitored with a Fluorlog-3 (Jobin Yvon) spectrofluorimeter at an excitation wavelength of 285 ± 5 nm and emission scanning from 295 to 400 nm. Different amounts of DOPG vesicles were introduced into the cuvette (at final lipid concentrations of 2.28, 28 and 275 µM, corresponding to P:L ratios of 0.88, 0.071 and 0.0073, respectively). Subsequently, NaCl was titrated into the cuvette to a final concentration of 350 mM. The emission spectra were corrected with the corresponding buffer spectra (including DOPG and salt) and fitted to a skewed Gaussian curve (Clark *et al.*, 2003) to obtain the fluorescence emission maximum, λ_{max}.

Peptide binding by ultracentrifugation

Increasing amounts of DOPG liposomes (0-753 µM) were added to 0.5 ml of 6 µM peptide in buffer A up to a P:L ratio of 1:114 and incubated for 20 min at room temperature. The samples were spun down by ultracentrifugation (1 h at 270,000 × g) and supernatants were separated from the pellets. A control experiment with an encapsulated dye in the same vesicles was carried out and under those conditions the vesicles were quantitatively spun down. To correct for the differences in quantum yield of the tryptophan fluorescence in different environments (hydrophilic buffer A vs. hydrophobic membrane environment), 2% (w/v) of sodium dodecyl sulfate (SDS) was added to the supernatant fraction and the fluorescence was measured. A correction was made for the background signal using a reference solution of buffer A, liposomes and SDS without the peptide. The percentage of binding was calculated using the equation:

$$\%\ Binding = 100 - (I_0/I \times 100),$$

where, I_0 is the fluorescence intensity of the supernatant sample with peptide without liposomes and I is the fluorescence intensity of the samples with liposomes. The obtained data were fitted to a general binding equation to obtain the dissociation constant (K_d):

$$\%\ Binding = (B_{max} \times C_{lipid})/(K_d + C_{lipid}),$$

where, C_{lipid} is the concentration of lipid and B_{max} is the maximum value for binding. For this purpose a simple binding equilibrium was assumed where peptide interacts [P] with the membrane [M] to form a peptide-membrane complex [PM]. This approach is equivalent to what was described by Matos and coworkers (Matos *et al.*, 2004). The affinity of peptide membrane interaction can also be expressed as partitioning coefficients (Melo & Castanho, 2007). The relationship between the two models is discussed in the work of Matos et al (Matos *et al.*, 2004).

Molecular Dynamics Simulations

System set-up

Simulations were performed with BPC194 [c(KKLKKFKKLQ)], and the linear analogue BPC193 [H-KKLKKFKKLQ-OH]. For the cyclic peptide, a peptide bond was created between the N-terminal lysine residue and the C-terminal glutamine residue. The initial structure of the peptides was modeled using the leap module of AMBER 9 (Case *et al.*, 2006).

Peptide in aqueous environment

A number of systems were prepared with either one cyclic or one linear peptide solvated by water. The cyclic peptide was initially unstructured in all simulations but different starting conformations of the linear analogue were tested: α-helix, bend and random-coil. An overview of all simulations performed is shown in Table 2 (Wa-Wk), and the details are presented in Table S1 (Mika *et al.,* 2011). All systems were simulated in a cubic box of length 4~5 nm and about 3000 water molecules. In a few simulations, counterions (Cl^-) were added to neutralize the system.

Peptide-membrane systems

A number of simulations were performed with peptides in a solvated DPPG (1,2-dipalmitoyl-sn-glycero-3-phosphatidylglycerol) membrane system. Simulations were performed with molar peptide: lipid (P:L) ratios of 1:128, 2:60, 4:128 and 9:128 (and 6000-8000 water molecules) for both BPC194 and BPC193 (see Table 2 for an overview and (Mika *et al.,* 2011) for details). Initially, the peptides were placed in the water phase close to the membrane surface, with distances between the peptide and membrane ranging from 1.5 to 2.3 nm. The cyclic peptide was initially unstructured and different conformations were tested for the linear peptide. Multiple simulations were run from different initial random velocity distributions for each of the P:L ratios. The simulations were carried out in the presence and absence of counter ions, and using different

Cyclic		Linear	
Code	Sequence	Code	Sequence
BPC194	c(KKLKK**F**KKLQ)	BPC193	H-KKLKK**F**KKLQ-OH
BPC294	c(KKLKK**Y**KKLQ)	BPC293	H-KKLKK**Y**KKLQ-OH
BPC418	c(KKLKK**W**KKLQ)	BPC417	H-KKLKK**W**KKLQ-OH

Table 1. Names and sequences of the peptides used in this study.

Peptide	P:L ratio	Code	Nr. of Sim.	%Non-Structured	%β-Structure	Peptide Depth [a]		Phe Depth [b]	
						Av.	Max	Av.	Max
Cyclic	Water	Wa-Wc	3	87 ± 5	13 ± 5	-	-	-	-
	1:128	1Ca-1Cg	7	79 ± 3	21 ± 3	-0.34 ± 0.38	-1.16	-0.52 ± 0.65	-1.75
	4:128	4Ca-4Cc	3	67 ± 4	33 ± 4	-0.08 ± 0.23	-0.99	-0.03 ± 0.29	-0.86
	9:128	9Ca-9Cj	10	68 ± 2	32 ± 2	-0.24 ± 0.25	-1.2	-0.57 ± 0.20	-1.4
Linear	Water	Wd-Wk	8	84 ± 4	16 ± 4	-	-	-	-
	1:128	1La-1Lb	2	100 ± 0	0 ± 0	-0.18 ± 0.25	-0.78	-0.10 ± 0.41	-0.85
	2:60	2La-2Lb	2	-	-	-	-	-	-
	4:128	4La-4Lb	2	100 ± 0	0 ± 0	-0.10 ± 0.18	-0.75	0.50 ± 0.23	-0.46
	9:128	9La-9Lg	7	99 ± 0	1 ± 0	0.41 ± 0.19	-0.62	0.52 ± 0.19	-1.37

Table 2. Overview of secondary structure and binding characteristics in all simulations performed on the cyclic (BPC194) and linear (BPC193) peptides. Results are averaged over all peptides present in the system, and over all independent simulations. The average binding depth as well as the maximum binding depth observed for a particular peptide is given. The standard errors reported are calculated from the standard deviation, between all peptides in all simulations.

[a] Center of mass of the peptide

[b] Center of mass of the phenyl ring of the phenylalanine residue

electrostatic schemes.

Simulations parameters

The GROMACS software package (van der Spoel *et al.*, 2005) was used to perform all MD simulations. The GROMOS force-field 43a2 (van Gunsteren *et al.*, 1996) was used to describe the peptide and peptide–solvent interactions. Simulations in water were also run using GROMOS force-field 53a6 (Oostenbrink *et al.*, 2005). The force-field for DPPG lipids was optimized from DPPC (Anézo *et al.*, 2003) and POPG (Zhao *et al.*, 2007) lipids, compatible with the GROMOS96 parameters. The choline head-groups were replaced by glycerol from the POPG force-field, and the tail parameters were taken from the DPPC force-field. The parameters were then optimized to achieve an area per lipid consistent with experiment (Pabst *et al.*, 2007). The equilibrated DPPG bilayer had a thickness of 3.54 ± 0.05 nm and an area per lipid of 0.69 ± 0.01 nm^2. All force-fields were parameterized for use with a group-based twin range cut-off scheme (using cutoffs of 1.0/1.4 nm and a pair-list update frequency of once per 10 steps), including a reaction field (Babakhani *et al.,* Tironi *et al.*, 1995) correction with a dielectric constant of 78 to account for the truncation of long-range electrostatic interactions. To test the effect of long-range electrostatic interactions, in some simulations the RF was replaced by the particle-mesh Ewald (PME) method. The water was modeled using the SPC model (Berendsen *et al.*, 1981). A time step of 2 fs was used. Bond lengths were constrained using the LINCS algorithm (Hess *et al.*, 1997). The simulations were performed in the NP_lP_ZT ensemble using periodic boundary conditions. The temperature was weakly coupled (coupling time 0.1 ps) to T = 320 K using the Berendsen thermostat (Berendsen *et al.*, 1984). The pressure was also weakly coupled (coupling time of 1.0 ps and compressibility of 4.5 × 10-5), using a semi isotropic coupling scheme in which the lateral (P_l) and perpendicular (P_Z) pressures were coupled independently at 1 bar, corresponding to a tension-free state of the membrane. The simulation setup is similar to that used in previous studies of peptide-membrane interactions (Leontiadou *et al.*, 2006, Sengupta *et al.*, 2008). For a general review on MD studies of peptide-membrane interactions see the work of Mátyus (Mátyus *et al.*, 2007).

Analysis

The secondary structure of the peptides was calculated with the DSSP code (Kabsch & Sander, 1983). For the cyclic peptide, the bonded N-terminus (K^1) and C-terminus (Q^{10}), present in the turn region, were neglected while calculating the secondary structure. The structural properties were then calculated from the average number of residues involved in each secondary structural feature along the simulation. The total "β-structure" is reported as the sum of β-sheet and β-bridge (one hydrogen bond less than β-sheet) and the "non-structured", as the sum of coil, bend and turn.

To analyze the alignment of the lysine residues, the distance between the planes formed by the C_α, C_γ and N_ζ atoms of the spatially-symmetric lysine residues K^1-K^8, K^2-K^7 and K^4-K^5 were calculated.

Results

The cyclic peptide permeabilizes the membrane and has a preference for anionic lipids

The cyclic peptide BPC194 has a high antimicrobial activity (MIC values ranged from 3.1-12 μM) and low hemolytic activity (not exceeding 17% at 375 μM) (Monroc *et al.*, 2006a). A calcein dequenching assay was performed to determine the membrane permeabilizing activity of the cyclic peptide, BPC194, two cyclic analogues (BPC294 with Tyr and BPC418 with Trp instead of Phe at position 6) and the corresponding linear analogues BPC193, BPC293, BPC417 (see Table 1 for peptide names and compositions). Figure 1 summarizes the results obtained for the cyclic analog BPC194 and shows that it caused the leakage of calcein from vesicles comprising of anionic lipids. The leakage reached 100% in DOPG membranes though it did not exceed 5% in DOPC, even at high P:L ratios (Fig. 1A). Experiments with liposomes composed of mixtures of DOPG, DOPC and/or DOPE confirmed that the cyclic peptide (BPC194) has a preference for anionic lipids since the leakage increases with the content of DOPG lipids in the vesicles (Fig. 1B). All three cyclic analogues caused the leakage of calcein for anionic membranes (Fig. 7), independent of the size of the vesicles (Fig. 7). These results are line with the *in vivo* data [15] and are consistent with the fact that bacterial membranes are generally more rich in negatively-charged lipids than the outer leaflet of the plasma membrane of higher eukaryotes, e.g. mammalian cells [14]. The calcein leakage from vesicles was negligible for the linear analogues, irrespective of the lipid composition. The low antimicrobial activity of the linear peptide is consistent with the lack of membrane permeation in model membrane systems. Below, we focus on the interaction of the cyclic and linear analogues with anionic lipids to understand the remarkable differences in their membrane permeabilizing properties.

Both the linear and cyclic peptides bind to PG membranes

To test whether the low activity of the linear peptides stems from their inability to bind to anionic membranes, we analyzed their membrane binding properties by MD simulations and fluorescence experiments. In the MD simulations, the peptides (BPC193 and BPC194) were placed in the water phase close to the surface of a DPPG bilayer at P:L ratios of 1:128, 4:128 and 9:128. Both peptides bound to the membrane rather fast and on similar (nanosecond) time scales (Figs. 2A and 2B). To validate the simulation data, the fluorescence of the tryptophan in BPC417 and BPC418 was used to monitor the interaction of the linear and cyclic peptides with the membranes. BPC417 and BPC418 bound to DOPG membranes albeit with different affinities (Fig. 2C). BPC418 bound to the membrane with a K_d, of 7 +/- 2 µM (under these conditions the overall P:L ratio = 0.84). BPC417 bound with a K_d for DOPG of 96 +/- 10 µM (P:L ratio = 0.0625). From the data presented in Fig. 2C, one can derive P:L ratios at which the amount of cyclic and linear peptide bound is equal and compare these conditions with those in Fig. 1A. Even at equal amounts of peptide interacting with the membrane, the cyclic peptide is orders of magnitude more effective in membrane permeabilization than the linear one. For instance, when the cyclic and the linear peptide are ~ 60% bound (P:L ratio of around 0.6 and 0.06, respectively) the cyclic peptide causes ~ 50% of dye leakage, while the linear analog is not active.

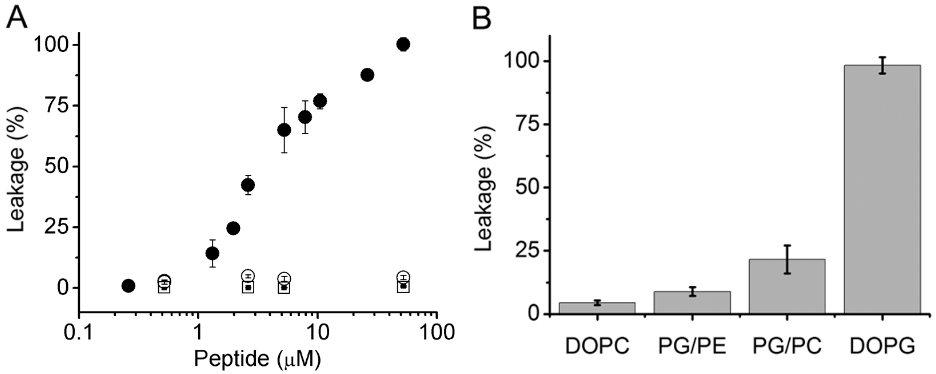

Figure 1. Vesicle permeabilizing properties of peptides. Leakage of calcein as a function of peptide concentration is shown. A. Circles: the action of BPC194 on DOPG and DOPC vesicles (filled and hollow symbols, respectively). Squares: data obtained with BPC193 with DOPG and DOPC vesicles (small filled and big hollow symbols, respectively). B. Calcein dequenching results for BPC194 using liposomes of different lipid composition: DOPC, DOPG/DOPE 1:1 (mol/mol) and DOPG/DOPC 1:1 (mol/mol) and DOPG. The end-points of leakage at a peptide concentration of 52 μM and a lipid concentration of 6.7 μM are shown. Error bars indicate deviation between individual experiments (n = 3).

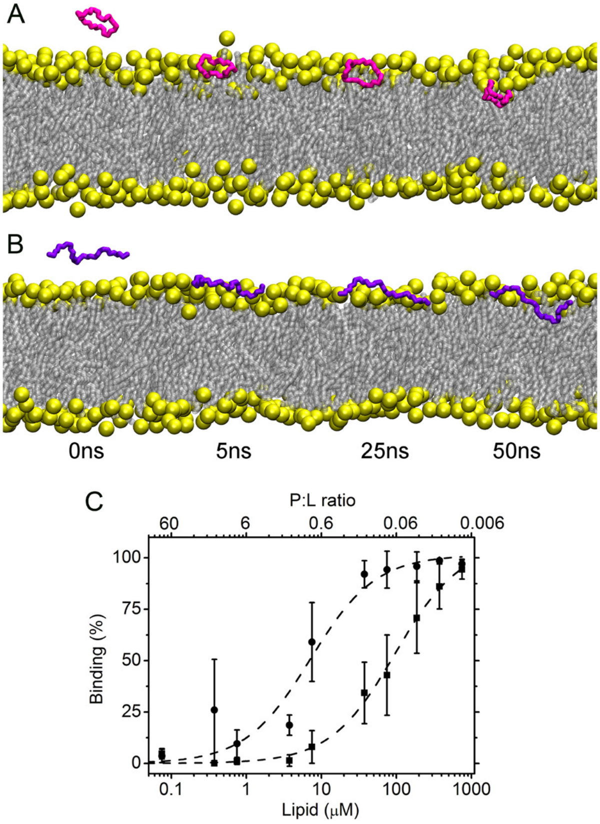

Figure 2. Binding of cyclic and linear peptides to PG membranes. A. Time course of the simulation 1Ca of BPC194 (pink) interacting with DPPG membranes. B. Time course of the simulation 1Lb of BPC193 (purple). In both A and B, the headgroup phosphorus atoms are shown in yellow, the lipid tails in grey and side-chains have been removed for clarity. C. Percentage binding of BPC418 (solid black circles) and BPC417 (solid black squares) at 6 μM concentration to DOPG membranes assessed by ultracentrifugation and employing the fluorescence of tryptophan. Error bars denote the deviation between individual experiments (n = 4); the top X-axis: P:L ratios corresponding to lipid concentrations indicated at the bottom axis. Dashed line: the fit of the data used to obtain the K_d.

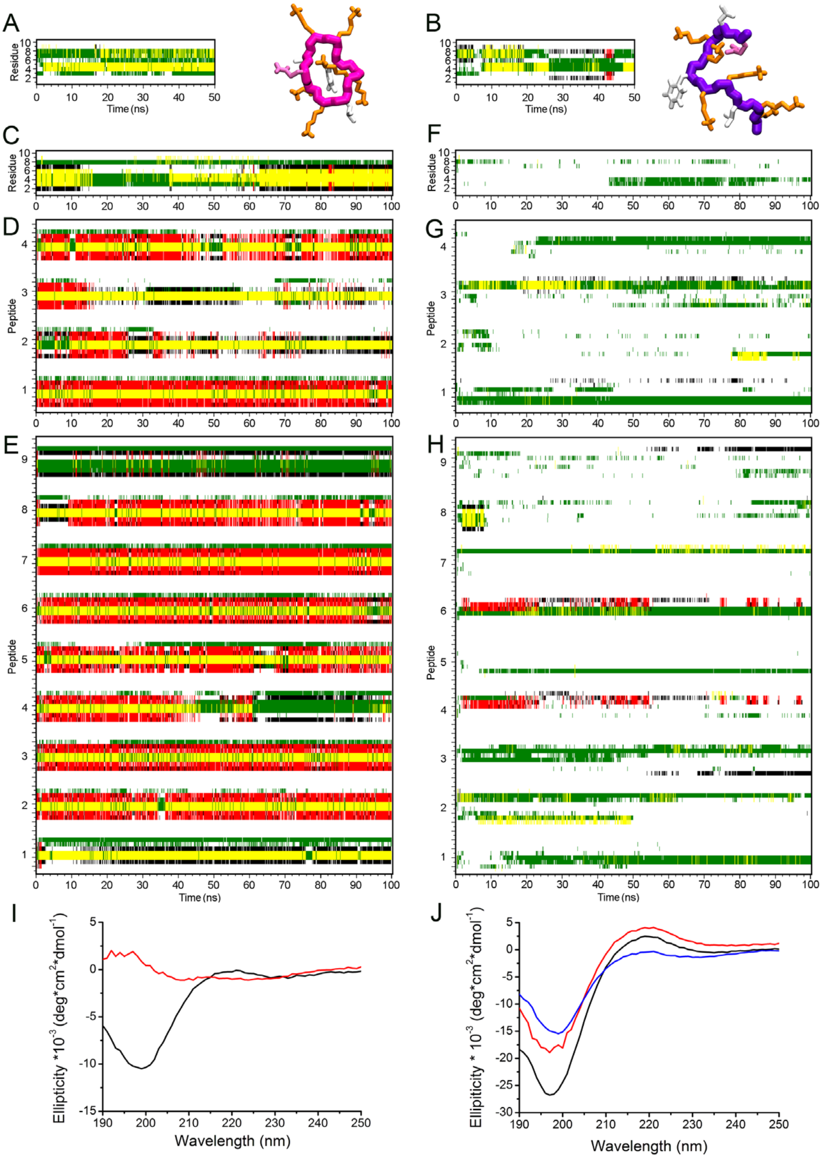

Figure 3. Structure of peptides in water and upon membrane binding. Secondary structure plot in water as determined by the DSSP code and representative snapshot of BPC194 (A) and BPC193 (B). The colors associated with the secondary structural elements are red (β-sheet), yellow (turn), green (bend), black (β-bridge) and white (coil). In both snapshots, Lys residues are shown in orange, Phe and Leu in white and Gln in light pink. C-E. Cyclic peptide DSSP plots of the simulations at P:L ratios of 1:128, 4:128 and 9:128, respectively. F-H. Linear peptide DSSP plot of representative simulations at P:L ratios 1:128, 4:128 and 9:128, respectively. I. CD spectra of the cyclic BPC194 in aqueous buffer (black line) and in the presence of DOPG vesicles (red line) at a P:L ratio of 0.38. J. CD spectra of the linear peptide BPC193 in buffer, in the presence of DOPG membranes (at P:L ratio 0.38) or a secondary structure inducer TFE (black, red and blue line, respectively). Peptides 0.15 mM, lipids 0.4 mM, TFE – 25% (vol/vol).

Both linear and cyclic peptides are structure-less in aqueous solution

To analyze the structure of the peptides in aqueous solution, atomistic MD simulations as well as CD measurements were performed. In the simulations, the cyclic and the linear peptide showed no defined secondary structure in aqueous solution and appeared mainly in a non-structured conformation (Figs. 3A and 3B). On average, only 13 and 16% β-structure was adopted by the cyclic and linear peptide, respectively (Table 2). Although we found that 50 ns of simulation were not sufficient for the peptides to completely sample their configurational space, the simulation data taken as a whole points to an unstructured conformation for both peptides in solution. The lack of secondary structure in the MD simulations was confirmed by CD measurements (Figs. 3I and 3J).

Cyclic peptide adopts β-structure upon binding to membranes

Upon interaction of BPC194 with the DPPG membrane surface, a secondary structure was induced within nanoseconds in the simulations (Fig. 3C-E). The average fraction of β-structure increased from 13% to 32% (Table 2). The increase in β-structure was most pronounced at the higher P:L ratios of 4:128 and 9:128. Visual inspection of the MD simulations of BPC194 showed that the β-structure formation gives rise to an amphipathic-like structure with a spatially-symmetric arrangement of two pairs of lysine residues: K^1-K^8 and K^2-K^7 on opposite strands. When the peptide adopted a β-structure, these lysine pairs aligned in a parallel manner and gave rise to a high charge density (Figs. 4A and 4B).

When the intra-strand hydrogen bonds were weakened and the β-structure was lost, the lysine residues could point away from each other (Fig. 4C). On average, the distances between the lysine pairs at the membrane interface were reduced from 1 nm (in aqueous medium) to about 0.7 nm. Upon addition of DOPG membranes, a substantial change in ellipticity of BPC194 was observed (Fig 3I); similar behavior was seen for the tryptophan (BPC418) and tyrosine containing (BPC294) cyclic peptides but not for the linear analogues (Fig.

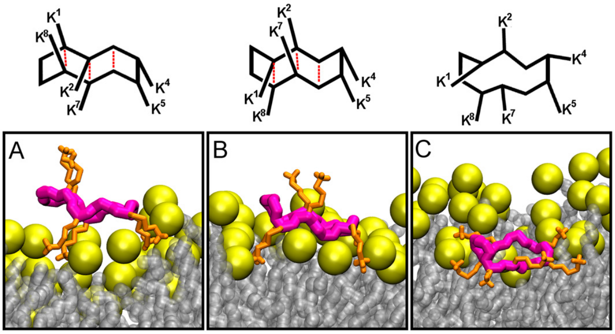

Figure 4. Different binding modes of the cyclic peptide. The lysine residues are depicted in orange, the head-group phosphorus atoms as yellow spheres and the acyl tails in grey. A-B. In certain binding modes during the simulation, the lysine residues aligned with inter-strand hydrogen bonds (depicted in red). C. In others, the lysines snorkelled out independently and the inter-strand distances increased.

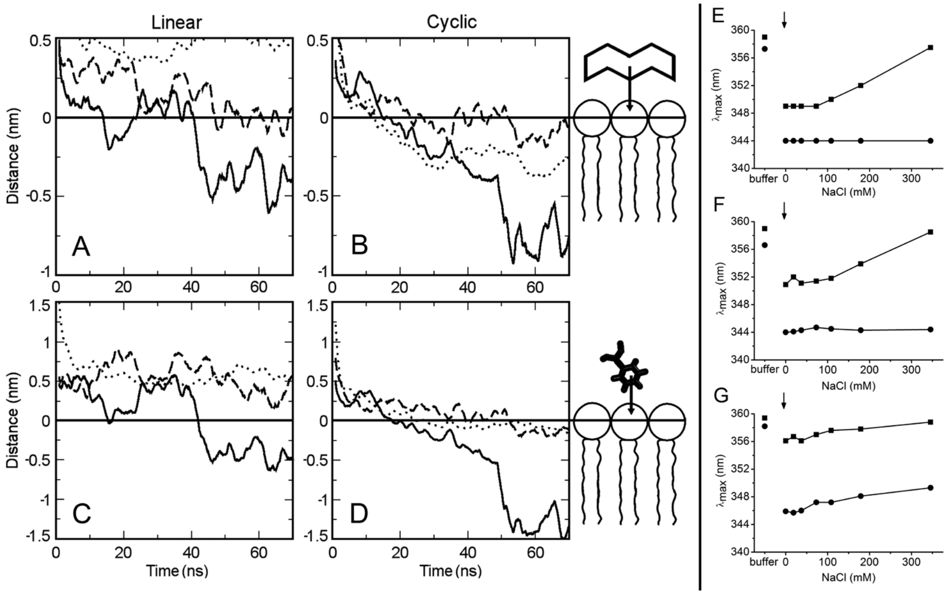

Figure 5. Depth of insertion of cyclic and linear peptides to PG membranes and peptide environment changes. A-D. MD simulations of peptides. Distance between the centre of mass of the peptides BPC193 (A) and BPC194 (B) and the phosphorus atoms of the DPPG bilayer at different P:L ratios: 1:128 (solid line), 4:128 (dashed line) and 9:128 (dotted line). At higher P:L ratios, the distances plotted are the averages of all peptides in the system. C-D. Distance between the phenylalanine residue and head-group phosphorus atoms. The zero value was taken as the interface boundary (horizontal solid line). E-G. Peptide environment assessed by Trp fluorescence. Wavelengths of tryptophan fluorescence emission maxima (λ_{max}) of BPC418 (circles, solid line) and BPC417 (squares, dashed line) in buffer (first data point), upon addition of DOPG membranes (arrow), and following titration with NaCl up to 350 mM. The peptide concentration was 2 μM; DOPG was added at different concentrations, yielding (E) P:L = 0.0073, (F) P:L = 0.071 and (G) P:L = 0.88.

9). The CD spectra of the cyclic peptides in the presence of DOPG are reminiscent of β-sheet and β-turn structures reported for other (cyclic) peptides (Wu & Hancock, 1999, Manning *et al.*, 1988, Bush *et al.*, 1978). However a quantitative deconvolution of the spectra is difficult as CD spectra simulators are designed for large proteins rather than cyclic small peptides. Unfortunately, it is not possible to perform solution-state NMR measurements on the membrane-associated states of the peptides, since the molecular mass of the vesicles to which the peptides are associated is so large that any NMR signal of the peptide would be broadened beyond detection.

The inactive linear peptide remains structure-less at the membrane surface

In contrast to the cyclic peptide, the linear analogue remained fully unstructured (Figs. 3F-H) with no intra-molecular hydrogen bonding at the DPPG membrane interface at P:L ratios of 1:128 and 4:128 (Table 2). At the highest P:L ratios (9:128) a few intermolecular interaction were observed, resulting in peptide clusters. This gave rise to some β-sheet characteristics on the interacting peptides, originating mainly from interactions of the peptide backbone and the glutamine side-chain. The CD measurements were entirely consistent with the MD simulations (Figs 3J).

The cyclic and linear peptides differ in membrane penetration

BPC194 was able to penetrate deeper into the phospholipid membrane than its linear counterpart. In the MD simulations, the distances between the phosphorus atoms of the outer leaflet and the centre of mass of the peptide were calculated and are plotted in Figs. 5A-D. The cyclic peptide BPC194 was able to insert below the level of the phosphorus atoms (see Table 2). Though a single peptide (P:L 1:128) appeared on average to bind deeper (-0.34nm)comparedtosystemswithP:Lratiosof4:128,9:128(-0.08nmand-0.24nm), the maximum insertion for individual peptides was at P:L ratio of 9:128 (-1.20 nm). Visual inspection of the trajectories showed that large values of insertion of the cyclic peptide were associated with high local perturbations, which led to poration of the membrane (Cirac *et al.*, 2011).The fluctuations in the outer leaflet, calculated as the deviation of the phosphorus atoms of the head-groups from their center of mass were ± 0.44 nm for the cyclic peptide. In contrast to the cyclic peptide, the linear analogue BPC193 did not embed very deep. The maximum insertion observed was -0.62 nm below the level of the phosphorus atoms and was not accompanied by large bilayer perturbations. Furthermore, low perturbations were seen in comparison to the cyclic peptide and the outer-leaflet fluctuations were ± 0.29 nm for the linear peptide.

Next, we examined the environment of the tryptophan from fluorescence emission spectra. The peptide that was initially in buffer was exposed to DOPG vesicles, which resulted in a blue-shift of the fluorescence emission peak (λ_{max}) of ~14 and ~10 nm for the cyclic and linear peptides, respectively (see Figs 5E and 5F; at these P:L ratios essentially all peptides are bound). The larger blue-shift for the cyclic peptide points to a more hydrophobic environment and thus to a deeper insertion into the membrane. Increasing the ionic strength resulted in a shift of the λ_{max} of the linear peptide back to what it was in the aqueous medium, which is indicative of reversible binding. The salt effect was not observed for the cyclic peptide, and even at the highest P:L ratio of 0.88 (where about 50% was bound (Fig. 2C) and the membranes were saturated with peptide), the backshift of λ_{max} was only marginal (Fig. 5G). Thus, the salt effects are also consistent with a deeper insertion of the cyclic peptide, BPC418, as compared to the linear one. It has been reported that certain peptides (*e.g* pep-1) (Henriques *et al.*, 2007) can translocate through the membrane without causing leakage/poration. We believe that the shallow and reversible membrane-embedding of BPC193 (incl. MD simulations and much less pronounced fluorescence blue-shift of the linear peptide as compared to the cyclic counterpart) argue against such possibility for the linear peptides.

Discussion

Molecular mechanism of pore formation

Based on our results, we propose here a molecular-detailed model outlining the differences in mode of action of the cyclic and linear peptides (schematically presented in Fig. 6). Both peptides when present in the aqueous phase are mainly unstructured and have a propensity to bind to (anionic) membrane surfaces. From this point on, the behavior of the two peptides diverges. The cyclic peptide has a larger tendency to fold, enabling it to insert deeper into the membrane interface. Through cooperative interactions, some of these membrane-embedded and folded cyclic peptides cause large perturbations in the bilayer. The linear peptide assumes a more extended conformation and is unable to perturb the membrane substantially. Finally, the cyclic peptide is able to porate the vesicles and cause dye leakage while the linear is unable to do so. The model highlights the structural and partitioning differences of two related peptides with the same sequence but varying antimicrobial activity and thereby point to the critical features required for high antimicrobial activity. The mechanistic model proposed here resembles the one described for gramicidin S in the sense that the cyclic peptide interacts with the membrane, adsorbs to the bilayer surface, folds and gets inserted into the hydrophobic core of the membrane (Jelokhani-Niaraki *et al.*, 2008). However, for BPC194 the poration has been confirmed experimentally and evaluated with molecular detail by MD simulations. The results of our study provide important clues for rational design of novel cyclic antimicrobial peptides (work in progress).

Folding and insertion of BPC194 at the membrane interface

The cyclization of the peptides that were studied is not linked to gain of structure in solution. However, upon membrane binding the cyclic peptide assumes a β-structure structure unlike the linear one. For BPC194, the β-structure gives rise to a spatially-symmetric arrangement of the lysine pairs, resulting in an amphipathic-like structure, a conformation that was seen also for gramicidin S (Kondejewski *et al.*, 1996). The linear peptide has larger conformational entropy, and folding of the backbone to a β-hairpin structure is less favorable than in the cyclic peptide. The structure formation and consequently a deeper insertion of the cyclic peptide was accompanied by local perturbations of the membrane-leaflet and could be linked to its higher charge density, compared to BPC193. The lower charge density of the linear peptide and the formation of peptide clusters may prevent the linear peptide from substantially perturbing or embedding into the membrane. A correlation between high charge density and poration has been previously seen for cyclic analogues of linear antimicrobial peptides (Shai, 2002).

Folding of BPC194 is reminiscent of folding in linear β-hairpin peptides

A very important aspect of this work is the prediction of the peptide folded states at the membrane interface by MD simulations and supported by CD studies. Predicting the correct folds and folding pathways of (poly)peptides, even short ones, remains a challenge. Folding of peptides into β-hairpins has been used as a paradigm for protein folding and a large number of pathways such as zip-in, zip-out and middle-out have been proposed (Chen & Xiao, 2008, Dinner *et al.*, 1999, Munoz *et al.*, 1998). Multiple, long simulations and enhanced sampling methods have often been used to probe the folding events. In contrast, in the simulations presented here, folding at the membrane surface is sampled within nanoseconds after the peptide binds to the membrane. While kinetics at membrane interfaces is usually slow, the ‘fast-folding’ observed here is due to the limited phase-space of the cyclic peptide. For BPC194, only three hydrogen bonds are present in the folded state and due to cyclization, the backbone atoms involved in these hydrogen bonds are close together even in the unfolded state. In water, the peptide is non-structured because the thermal fluctuations are enough to break these three backbone hydrogen bonds that are then compensated by the neighboring water molecules. However, at the membrane interface the backbone atoms (that are always spatially close) form the three hydrogen bonds because of lack of other hydrogen-bond partners and the lower polarity of the membrane leading to the peptide adopting the folded state very fast. The folding is reminiscent of the zip-in model described for linear β-hairpins, whereby the ends first approach each other and then the hydrogen bonds are formed.

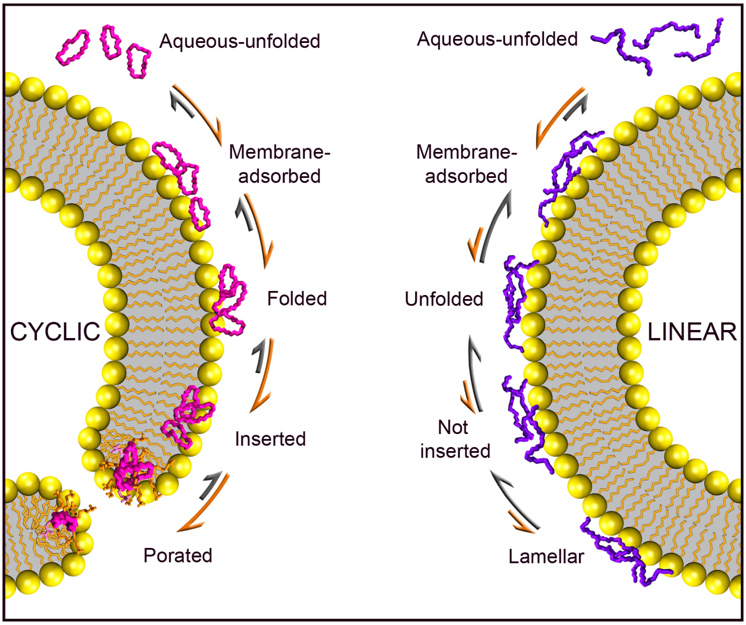

Figure 6. A schematic view of the mechanism of action. Left: The cyclic peptide BPC194 (pink); right: the linear analogue BPC193 (purple). The five possible thermodynamic states (stable or metastable) are: aqueous-unfolded, membrane-adsorbed, folded, inserted and porated. The equilibrium is shifted to the right for the cyclic peptide BPC194 and the porated state is the most favorable one. For the linear analogue BPC193, the membrane-adsorbed is the most favored state and the peptide remains unfolded at the surface of the membrane.

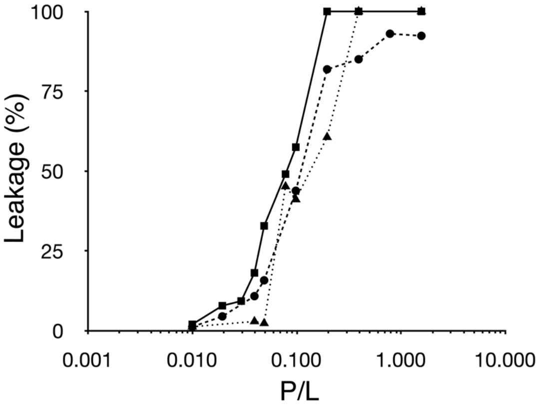

Figure 7. Vesicle permeabilizing properties of the cyclic analogues BPC194, BPC294 and BPC418. The percentage of leakage of calcein from DOPG liposomes is represented as a function of peptide concentration at a final lipid concentration of 10.6 µM. Triangles, dotted line represent data for BPC194; circles, dashed line: BPC294; and squares, solid line: BPC418. In all cases the cyclic peptides had similar membrane-permeabilizing properties.

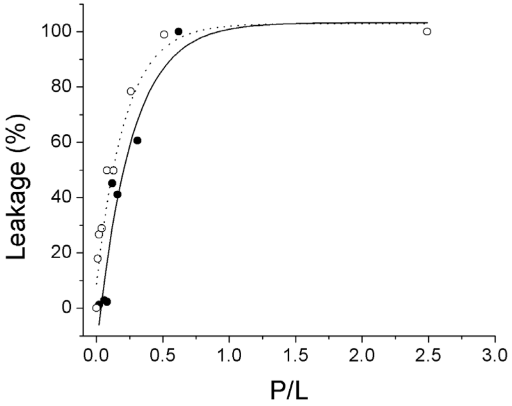

Figure 8. Vesicle permeabilizing propensity of BPC194 with SUVs and LUVs. The percentage of leakage of DOPG vesicles is represented as a function of P/L ratio (lipid concentration constant at 10.6 μM). BPC194 has similar poration propensity with small LUVs (80 nm in size; full circles) and 200 nm LUVs vesicles (open circles).

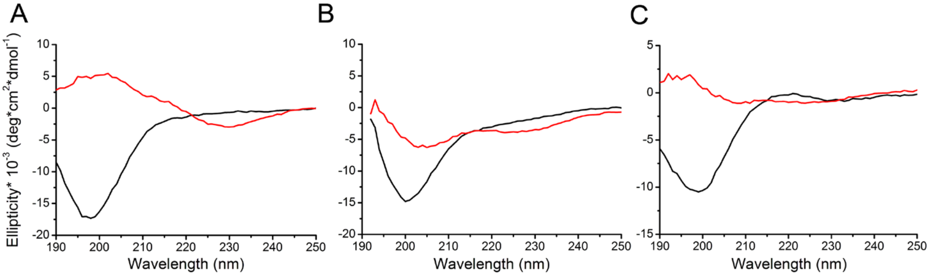

Figure 9. Secondary structure of cyclic peptide analogues. CD spectra of BPC294 (A), BPC418 (B) and BPC194 (C) in aqueous buffer (black line) and in the presence of DOPG liposomes (red line) at P:L ratios of 1.5, 0.3 and 0.3, respectively. The peptide concentration was 0.15 mM, the lipid concentration 0.1 mM (A) and 0.4 mM (B and C). The spectra of BPC418 suffered from high scattering due to fusing vesicles and were acquired at lower lipid concentrations. The CD spectra of small cyclic peptides are difficult to deconvolute because of the contributions of different turns and aromatic residues, and the lack of experimental structural data such as X-ray and NMR. On the basis of our MD simulations and the fact that the recorded spectra are reminiscent of β-sheet and β-turn, we conclude that the peptides upon interaction with DOPG vesicles undergo folding.

Conclusions

In conclusion, there is now compelling evidence that cyclization of certain sequences of membrane-active peptides enhances their antimicrobial performance. In this paper, we analyze the molecular basis for activity in a cyclic antimicrobial peptide, BPC194 by comparing the mechanism of action of the active and inactive analogues. We show that the molecular basis for the enhanced activity resides most likely in the restriction of the number of conformations in the cyclic peptide. We show that it can adopt a favorable orientation towards the membrane and acquire an ordered structure that allows a high charge density and amphipathic arrangement. The latter allows the cyclic peptide to locate itself deeper in the membrane as well as to perturb it more than its linear counterpart. Thus, the alignment of lysine residues on opposite strands leads to a high charge density and an amphipathic arrangement. We propose that these structural and partitioning behavior determined here are related to the difference in poration propensity and thus the antimicrobial activity.

Acknowledgemenst

We acknowledge financial support from the Spanish MICINN (MAT2008-04834 to ADC) and MEC (BES-2006-11671 doctoral fellowship to ADC), Netherlands NWO (DS, SJM), SysMo via the BBSRC-funded KosmoBac programme (BP), NWO (Top-subsidy grant 700.56.302 to BP), the Zernike Institute for Advanced Materials (to support the appointment and research of GMC and JTM). We would also like to thank Dr. Gert N. Moll and Dr. Renske W. Hesselink for helpful discussions and assistance.

References

Anézo, C., A. H. de Vries, H. D. Höltje, D. P. Tieleman & S. J. Marrink, (2003) Methodological issues in lipid bilayer simulations. *J. Phys. Chem. B* **107**: 9424-9433.

Babakhani, A., A. A. Gorfe, J. Gullingsrud, J. E. Kim & J. A. McCammon, (2007) Peptide insertion, positioning, and stabilization in a membrane: Insight from an all-atom molecular dynamics simulation. *Biopolymers* **85***:* 490-497.

Berendsen, H. J. C., J. P. M. Postma, W. F. van Gunsteren & J. Hermans, (1981) Interaction models for water in relation to protein hydration. *Intermolecular Forces*: 331-342.

Berendsen, H. J. C., J. P. M. Postma, W. F. van Gunsteren, A. D. Nola & J. R. Haak, (1984) Molecular dynamics with coupling to an external bath. *J. Chem. Phys.* **81**: 3684-3690.

Brogden, K. A., M. Ackermann, P. B. J. McCray & B. F. Tack, (2003) Antimicrobial peptides in animals and their role in host defences. *Int. J. Antimicrob. Agents* **22**: 465-478.

Bush, C. A., S. K. Sarkar & K. D. Kopple, (1978) Circular dichroism of beta turns in peptides and proteins. *Biochemistry* **17**: 4951-4954.

Case, D. A., T. A. Darden, T. E. Cheatham III, C. L. Simmerling, J. Wang, R. E. Duke, R. Luo, K. M. Merz, D. A. Pearlman, M. Crowley, R. C. Walker, W. Zhang, B. Wand, S. Hayik, A. Roitberg, G. Seabra, K. F. Wong, F. Paesani, X. Wu, S. Brozell, V. Tsui, H. Gohlke, L. Yang, C. Tan, J. Mongan, V. Hornak, G. Cui, P. Beroza, D. H. Mathews, C. Schafmeister, W. S. Ross & P. A. Kollman, (2006) AMBER 9. In. University of California, San Francisco, pp.

Chen, C. & Y. Xiao, (2008) Observation of multiple folding pathways of beta-hairpin trpzip2 from independent continuous folding trajectories. *Bioinformatics* **24**: 659-665.

Cirac, A. D., G. Moiset, J. T. Mika, A. Kocer, P. Salvador, B. Poolman, S. J. Marrink & D. Sengupta, (2011) The molecular basis for antimicrobial activity of pore-forming cyclic peptides. *Biophys. J* **100**: 2422-2431

Clark, E., J. East & A. Lee, (2003) The role of tryptophan residues in an integral membrane protein: Diacylglycerol kinase. *Biochemistry* **42**: 11065-11073.

Dathe, M., H. Nikolenko, J. Klose & M. Bienert, (2004) Cyclization increases the antimicrobial activity and selectivity of arginine- and tryptophan-containing hexapeptides. *Biochemistry* **43**: 9140-9150.

Davies, J. S., (2003) The cyclization of peptides and depsipeptides. *J. Pept. Sci.* **9**: 471-501.

Dinner, A. R., T. Lazaridis & M. Karplus, (1999) Understanding beta-hairpin formation. *Proc. Natl. Acad. Sci. U.S.A.* **96**: 9068-9073.

Epand, R. M. & H. Vogel, (1999) Diversity of antimicrobial peptides and their mechanism of action. *Biochim. Biophys. Acta* **1462**: 11-28.

Ganz, T., (2003) Defensins: Antimicrobial peptides of innate immunity. *Nat. Rev. Immunol.* **3**: 710-720.

Henriques, S. T., A. Quintas, L. A. Bagatolli, F. Homble & M. A. Castanho, (2007) Energy-independent translocation of cell-penetrating peptides occurs without formation of pores. A biophysical study with pep-1. *Mol Membr Biol* **24**: 282-293.

Hess, B., H. Bekker, H. J. C. Berendsen & J. G. E. M. Fraaije, (1997) LINCS: A linear constraint solver for molecular simulations. *J. Comput. Chem.* **18**: 1463-1471.

Houston, M. E. J., L. H. Kondejewski, D. N. Karunaratne, M. Gough, S. Fidai, R. S. Hodges & R. E. W. Hancock, (1998) Influence of performed alpha-helix and alpha-helix induction on the activity of cationic antimicrobial peptides. *J. Pept. Res.* **52**: 81-88.

Huang, H. W., (2000) Action of antimicrobial peptides: Two-state model. *Biochemistry* **39**: 8347-8352.

Jelokhani-Niaraki, M., R. S. Hodges, J. E. Meissner, U. E. Hassenstein & L. Wheaton, (2008) Interaction of gramicidin S and its aromatic amino-acid analog with phospholipid membranes. *Biophys. J.* **95**: 3306-3321.

Jenssen, H., P. Hamill & R. E. W. Hancock, (2006) Peptide Antimicrobial Agents. *Clin. Microbiol. Rev.* **19**: 491-511.

Kabsch, W. & C. Sander, (1983) Dictionary of protein secondary structure: Pattern recognition of hydrogen-bonded and geometrical features. *Biopolymers* **22**: 2577-2637.

Kato, T. & N. Izumiya, (1977) Conformations of di-N-methylleucine gramicidin S and N-methylleucine gramicidin S compatible with the sidedness hypothesis. *Biochim. Biophys. Acta* **493**.

Koçer, A., M. Walko, W. Meijberg & B. L. Feringa, (2005) A light-actuated nanovalve derived from a channel protein. *Science* **309**: 755-758.

Kondejewski, L. H., S. W. Farmer, D. S. Wishart, C. M. Kay, R. E. W. Hancock & R. S. Hodges, (1996) Modulation of structure and antibacterial and hemolytic activity by ring size in cyclic gramicidin S analogs. *J. Biol. Chem.* **271**: 25261-25268.

Lehrer, R. I. & T. Ganz, (1999) Antimicrobial peptides in mammalian and insect host defence. *Curr. Opin. Immunol.* **11**: 23-27.

Leontiadou, H., A. E. Mark & S. J. Marrink, (2006) Antimicrobial peptides in action. *J. Am. Chem. Soc.* **128**: 12156-12161.

Manning, M. C., M. Illangasekare & R. W. Woody, (1988) Circular dichroism studies of distorted alpha-helices, twisted beta-sheets, and beta turns. *Biophys Chem* **31**: 77-86.

Matos, C., J. L. Lima, S. Reis, A. Lopes & M. Bastos, (2004) Interaction of antiinflammatory drugs with EPC liposomes: calorimetric study in a broad concentration range. *Biophys J* **86**: 946-954.

Mátyus, E., C. Kandt & D. P. Tieleman, (2007) Computer simulations of antimicrobial peptides. *Curr. Med. Chem.* **14**: 2789-2798.

Mika, J.T., Moiset G., Cirac, A.D, Feliu, L., Bardaji, E., Planas, M., Sengupta, D., Marrink S.J. & B. Poolman, (2011) Structural basis for the enhanced activity of cyclic anitmicrobial peptides: The case of BPC194. *Biochim Biophys Acta* **1808**: 2197-2205.

Melo, M. N. & M. A. Castanho, (2007) Omiganan interaction with bacterial membranes and cell wall models. Assigning a biological role to saturation. *Biochim Biophys Acta* **1768**: 1277-1290.

Melo, M. N., R. Ferre & M. A. R. B. Castanho, (2009) Antimicrobial peptides: Linking partition, activity and high membrane-bound concentrations. *Nat. Rev. Microbiol.* **7**: 245-250.

Monroc, S., E. Badosa, E. Besalú, M. Planas, E. Bardají, E. Montesinos & L. Feliu, (2006a) Improvement of cyclic decapeptides against plant pathogenic bacteria using a combinatorial chemistry approach. *Peptides* **27**: 2575-2584.

Monroc, S., E. Badosa, L. Feliu, M. Planas, E. Montesinos & E. Bardají, (2006b) De novo designed cyclic cationic peptides as inhibitors of plant pathogenic bacteria. *Peptides* **27**: 2567-2574.

Munoz, V., E. R. Henry, J. Hofrichter & W. A. Eaton, (1998) A statistical mechanical model for beta-hairpin kinetics. *Proc. Natl. Acad. Sci. U.S.A.* **95**: 5872-5879.

Oostenbrink, C., T. A. Soares, N. F. van der Vegt & W. F. van Gunsteren, (2005) Validation of the 53A6 GROMOS force field. *Eur. Biophys. J.* **34**: 273-284.

Pabst, G., S. Danner, S. Karmakar, G. Deutsch & V. A. Raghunathan, (2007) On the propensity of phosphatidylglycerols to form interdigitated phases. *Biophys. J.* **93**: 513-525.

Sengupta, D., H. Leontiadou, A. E. Mark & S. J. Marrink, (2008) Toroidal pores formed by antimicrobial peptides show significant disorder. *Biochim. Biophys. Acta* **1778**: 2308-2317.

Shai, Y., (2002) Mode of action of membrane active antimicrobial peptides. *Biopolymers* **66**: 236-248.

Tironi, I. G., R. Sperb, P. E. Smith & W. F. van Gunsteren, (1995) A generalized reaction field method for molecular dynamics simulations. *J. Chem. Phys.* **102**: 5451-5459.

Toke, O., (2005) Antimicrobial peptides: New candidates in the fight against bacterial infections. *Biopolymers* **80**: 717-735.

van den Bogaart, G., J. V. Guzmán, J. T. Mika & B. Poolman, (2008) On the mechanism of pore formation by melittin. *J. Biol. Chem.* **283**: 33854-33857.

van der Spoel, D., E. Lindahl, B. Hess, G. Groenhof, A. E. Mark & H. J. C. Berendsen, (2005) GROMACS: Fast, flexible, and free. *J. Comput. Chem.* **26**: 1701-1718.

van Gunsteren, W. F., P. Krüger, S. R. Billeter, A. E. Mark, A. A. Eising, W. R. P. Scott, P. H. Hüneberger & I. G. Tironi, (1996) *Biomolecular Simulation: The GROMOS96 Manual and User Guide*.

Wu, M. & R. E. W. Hancock, (1999) Interaction of the cyclic antimicrobial cationic peptide bactenecin with the outer and cytoplasmatic membrane. *J. Biol. Chem.* **274**: 29-35.

Zasloff, M., (2002) Antimicrobial peptides of multicellular organisms. *Nature* **415**: 389-395.

Zhao, W., T. Róg, A. A. Gurtovenko, I. Vattulainen & M. Karttunen, (2007) Atomic-scale structure and electrostatics of anionic palmitoyloleoylphosphatidylglycerol lipid bilayers with Na+ counterions. *Biophys. J.* **92**: 1114-1124.

CHAPTER 8

THE MOLECULAR BASIS FOR ANTIMICROBIAL ACTIVITY OF PORE-FORMING CYCLIC PEPTIDES

Anna D. Cirac, Gemma Moiset, Jacek T. Mika, Armagan Koçer, Pedro Salvador, Siewert J. Marrink, Bert Poolman & Durba Sengupta

Biophysical Journal 2011, **100**: 2422-22431

The mechanism of action of antimicrobial peptides is still poorly understood. To probe the biophysical characteristics that confer activity, we present here a molecular-dynamics and biophysical study of a cyclic antimicrobial peptide and its inactive linear analogue. In the simulations, the cyclic peptide caused large perturbations in the bilayer and cooperatively opened a disordered toroidal pore, 1-2 nm in diameter. Electrophysiology measurements confirm discrete poration events of size 1-2 nm by the cyclic peptide. We also show that lysine residues aligning parallel to each other in the cyclic but not linear peptide are crucial for function. By employing Dual-Color Fluorescence Burst Analysis (DCFBA), we show that both peptides are able to fuse/aggregate liposomes but only the cyclic peptide is able to porate them. The results provide detailed insight on the molecular basis of activity of cyclic antimicrobial peptides.

Introduction

How antimicrobial peptides (AMPs) kill bacteria by interacting with the cell membrane is not fully understood. These peptides, often small and cationic, are secreted into the aqueous phase, usually in an unfolded state and bind quickly to the target membrane, where secondary structure may be induced (Brogden, 2005, Brogden *et al.*, 2003, Hancock & Rozek, 2001, Jenssen *et al.*, 2006, Seelig, 2004, Shai, 1999, White & Wimley, 1999, Zasloff, 2002). At a certain threshold concentration antimicrobial peptides permeabilize the membrane, either by forming a discrete pore or by disrupting the bilayer structure (Brogden *et al.*, 2003, Epand & Vogel, 1999, Ferre *et al.*, 2009, Hancock & Chapple, 1999, Huang, 2000, Huang, 2004, Huang, 2006, Jenssen *et al.*, 2006, Melo *et al.*, 2009, Shai, 1999, Shai, 2002, Tossi, 2000, van den Bogaart *et al.*, 2008a, Yang *et al.*, 2001). For linear α-helical peptides the barrel-stave and toroidal-shaped model have been proposed as pore structures (Brogden *et al.*, 2003, Hancock & Rozek, 2001, Ludtke *et al.*, 1996, Qian *et al.*, 2008, Shai, 2002, Subbalakshmi & Sitaram, 1998, Yeaman & Yount, 2003). In addition, a disordered toroidal pore has been proposed for linear antimicrobial peptides from molecular dynamics (MD) simulations (Jean-François *et al.*, 2008, Leontiadou *et al.*, 2006, Sengupta *et al.*, 2008).

Cyclic AMPs have emerged as good antimicrobial candidates due to their robust secondary structure and high activity (Jelokhani-Niaraki *et al.*, 2008, Jelokhani-Niaraki *et al.*, 2002, Matsuzaki, 2009). Gramicidin S, a cationic decapeptide, is one of the best studied cyclic AMPs (Gibbs *et al.*, 1998, Jelokhani-Niaraki *et al.*, 2008, Jelokhani-Niaraki *et al.*, 2002, Lee & Hodges, 2003, Prenner *et al.*, 1999) and has been shown to permeabilize bilayers but not to stabilize well-defined pores (Mak & Webb, 1995). MD simulations in DMSO solution (Mihailescu & Smith, 1999) and with DMPC bilayers (Mihailescu & Smith, 2000) have shown that gramicidin S has a relatively rigid backbone conformation, but no poration events were seen in the simulations. Arginine-rich cyclic peptides have been shown to assemble into nanotubes and extrude the bilayer in MD simulations (Khalfa & Tarek, 2010). In general, the molecular details of the action of cyclic AMPs, such as whether these short peptides can open and stabilize pores, as well as the molecular basis for their increased activity is still unclear.

The focus of our work is a cyclic antimicrobial peptide, BPC194 that was chosen as the best candidate from a library of *de novo* synthesized cyclic peptides (Monroc *et al.*, 2006a, Monroc *et al.*, 2006b). The cyclic peptide shows a high antimicrobial activity to different plant pathogenic bacteria (*Erwinia amylovora*, *Pseudomonas syringae* and *Xanthomonas vesicatoria*). Here, we present a combined MD and biophysical study of the cyclic peptide interacting with anionic lipid bilayers to understand its mechanism of action. The linear analogue BPC193, which is not active, has also been studied allowing us to reveal the functionally - important structural characteristics. We show that the only cyclic peptide is able to form pores in anionic membranes in line with its enhanced antimicrobial activity. The pore size was validated by three independent approaches - MD simulations, electrophysiology and DCFBA fluorescence imaging. We further extract the functionally - relevant structural properties and show the importance of charged residues in forming and stabilizing pores. Finally, an intermediate state was identified which is close to the real transition state during pore formation.

Materials and methods

Molecular Dynamics Simulations

System set-up. MD simulations were performed for systems containing 9 peptides (BPC194 c(KKLKKFKKLQ); BPC193 KKLKKFKKLQ) and a fully solvated DPPG (dipalmitoyl-phosphatidylglycerol; anionic lipid) bilayer. The simulations were carried out at a peptide:lipid (P:L) ratio of 9:128 for both cyclic and the linear analogues together with 6000~8000 water molecules and 128 K^+ as counter-ions for anionic lipids. The peptides were initially placed in the water phase at a distance of 1.5-2.3 nm from the membrane surface. The initial structure of the peptides was modeled using the leap module of AMBER 9 (Case *et al.*, 2006), as unstructured peptides with no intra-molecular hydrogen bonds. Multiple simulations were run from different initial random velocity distributions (Table S1 in Cirac *et al.* (2011)).

Set-up for transition state simulations.

A snapshot at 109 ns was taken from the simulation 9Ca (Cirac *et al.*, 2011), as an example of the transition state. From this system, ten simulations were performed with different initial velocity distributions. The transition state was also modified to substitute the cyclic peptide for the linear analogue. This substitution was made by cutting the peptide bond between N-terminal residue and the C-terminal residue, as well as adding the corresponding missing atoms. The system was simulated as a linear peptide but with the initial conformation of the cyclic peptide (so called hairpin conformation). Further, a harmonic potential was applied to the linear peptide to pull the N-terminal from C-terminal to obtain a random-coil conformation in the transition state. For the modified systems, a minimization was carried out followed by an equilibration with constraints on phosphorus atom and water molecules to keep the position of the transition state. Ten simulations were run for the hairpin conformation and two of the random-coil conformation by changing the starting random velocities.

Analysis.

The secondary structure of the peptides was calculated by using the DSSP code (Kabsch & Sander, 1983). For the cyclic peptide, the N-terminal residue K^1 and C-terminal residue Q^{10} that are present in the turn region, were neglected while calculating the secondary structure. The structural properties were then calculated from the average number of residues involved in each secondary structural feature along the simulation. The total b-structure is reported as the sum of b-sheet and b-bridge and the total non-structured as the sum of coil bend and turn. The persistence of structure over time was calculated as the percentage of time the β-structure was present.

Simulation parameters.

All MD simulations were performed with the GROMACS software package (van der Spoel *et al.*, 2005). The peptide and peptide–solvent interactions were described by the GROMOS force-field 43a2 (van Gunsteren *et al.*, 1996).

The force-field for DPPG lipids was optimized from DPPC (Anézo *et al.*, 2003) and POPG (Zhao *et al.*, 2007) lipids, compatible with the GROMOS96 parameters. The choline head-groups were replaced by glycerol from the POPG force-field, and the tail parameters were taken from the DPPC force-field. The parameters were then optimized to achieve an area per lipid consistent with experiment (Pabst *et al.*, 2007). The equilibrated DPPG bilayer had a thickness of 3.54 ± 0.05 nm and an area per lipid of 0.69 ± 0.01 nm^2. The force-fields have been parameterized for use with a group-based twin range cut-off scheme (using cutoffs of 1.0/1.4 nm and a pair-list update frequency of once per 10 steps), including a reaction field (RF (Tironi *et al.*, 1995)) correction with a dielectric constant of 78 to account for the truncation of long-range electrostatic interactions. The water was modeled using the SPC model (Berendsen *et al.*, 1981). The simulations were performed using periodic boundary conditions and a time step of 2 fs was used. The temperature was weakly coupled (coupling time 0.1 ps) to T = 320 K, using the Berendsen thermostat (Berendsen *et al.*, 1984). The pressure was weakly coupled (coupling time of 1.0 ps and compressibility of 4.5×10^{-5}), using a semi-isotropic coupling scheme in which the lateral (P_l) and perpendicular (P_Z) pressures are coupled independently at 1 bar, corresponding to a tension-free state of the membrane. The simulation setup is similar to that used in previous studies of peptide-membrane interactions (Leontiadou *et al.*, 2006, Sengupta *et al.*, 2008, Yesylevskyy *et al.*, 2009). For a general review on MD studies of peptide-membrane interactions see the work of Mátyus (Mátyus *et al.*, 2007).

Biophysical Characterization

Electrophysiology measurements.

A planar lipid bilayer setup was used as described below. The bilayer was formed by painting with 1 μl of a 20 mg/ml solution of DOPG lipid (1,2-dioleoyl-sn-glycero-3-phosphatidylglycerol, Avanti Polar Lipids) in n-decane (Aldrich) across the 250 μm opening of a Delrin cup that separates two solution-filled compartments, designated cis and trans (Mueller *et al.*, 1962a, Mueller *et al.*, 1962b, Mueller *et al.*, 1963). Both compartments were filled with a buffer solution consisting of 10 mM HEPES (2-(4-(2-hydroxyethyl)-1-piperazinyl)-ethanesulfonic acid, (Roche Diagnostics GmbH), pH 7.0, containing 150 mM NaCl (Merck), further referred to as buffer A. The planar bilayers were stable at the voltages applied during the experiment. The transmembrane current (I_m) under different applied potentials (V) was monitored, using an integrating Bilayer Clamp Amplifier BC-535 (Warner Instruments). Currents were filtered through an 8-pole low-pass Bessel Filter LPF-8 (Warner Instruments) and digitized using Clampex 10.2 software (Axon Molecular Devices). Membrane conductance (G_m) events were identified as $G_m = I_m/V$ and analyzed with the Clampfit software (Axon Molecular Devices) (Salay *et al.*, 2004). The peptides at 3 and 10 μM were added to the cis side of the planar lipid bilayer and stirred for 1 minute without applying voltage. In some cases a voltage of ± 40 mV was applied to pre-activate the peptide and decrease the time needed to observe activity. Subsequently, the conductance was recorded at different voltages ranging from 0 to ± 50 mV. A total of 10 traces were recorded each with freshly prepared DOPG membranes. The pore diameter was estimated by an extended version of the model proposed by Hille (Hille, 1968, Hille, 2001) given by (Cruickshank *et al.*, 1997):

$$d = \frac{\rho g}{\pi}\left(\frac{\pi}{2} + \sqrt{\frac{\pi^2}{4} + \frac{4\pi l}{\rho g}}\right), \qquad (1)$$

where d is the diameter of the pore, ρ is the resistivity of the buffer, g is the measured conductance and l is the length of the pore. The resistivity of the buffer A was assumed to be 80 Ωm (Hille, 2001). The length of the pore equals the membrane thickness and was assumed to be 3.5 nm.

Dual-color fluorescence burst analysis.

In the DCFBA experiment, liposomes were labeled with two, spectrally non-overlapping fluorescent probes (van den Bogaart *et al.*, 2007a). One probe was incorporated in the phospholipid bilayer, while the other filled the aqueous interior of the liposome. By using a dual-color laser-scanning microscope, we monitored membrane disrupting effects at the single liposome level.

The results are presented in the DCFBA profiles as the population-distribution histogram of liposomes with a given internal marker concentration*,* C_i, given by:

$$C_i = \frac{\int_{t_1}^{t_2} I_{SM}\,dt}{\left(\int_{t_1}^{t_2} I_L\,dt\right)^{\frac{3}{2}}}, \tag{2}$$

where I_L is the fluorescence of the lipid marker and I_{SM} is the fluorescence of the internal size marker in each fluorescence burst (van den Bogaart *et al.*, 2007b). The average fluorophore population, P_{av}^{fluor}, is given by:

$$P_{av}^{fluor} = \frac{\int_{t_1}^{t_2} \frac{I_{fluor}}{N_{peaks}}\,dt}{\int_{t_1}^{t_2} \frac{I_{fluor}^0}{N_{peaks}^0}\,dt}, \tag{3}$$

where I_{fluor} is the fluorescence intensity of each peak above a given threshold for every P:L ratio, I^0_{fluor} is I_{fluor} at P:L = 0, N_{peaks} is the number of peaks at every P:L ratio and N^0_{peaks} is N_{peaks} at P:L = 0. The relative population of the internal size marker, P_{rel}^{SM}, is given by:

$$P_{rel}^{SM} = \frac{P_{av}^{SM}}{P_{av}^{membr}}, \tag{4}$$

where P_{av}^{SM} is the average internal marker population and P_{av}^{membr} is the average membrane fluorophore population.

Liposomes were prepared as described by van den Bogaart (van den Bogaart *et al.*, 2007a). Briefly, DiD (1,1’-dioctadecyl-3,3,3’,3’-tetramethylindodicarbo-cyanine perchlorate; Invitrogen) labeled-liposomes were prepared by rehydration of a dried lipid film in the presence of glutathione (GSH)-labeled Alexa Fluor 488 (AF488, Invitrogen) as a aqueous phase marker in buffer A. The DiD/DOPG molar ratio was 1:12,000. Subsequently, the liposomes were extruded 11 times through a 200 nm polycarbonate filter (AVESTIN, Canada). The liposomes were separated from the non-encapsulated fluorophores by centrifugation (20 min, 270,000 × g, 20° C) and resuspended in buffer A to a final concentration of 5 mg/ml DOPG. Fluorescence burst analysis was carried out on a laser-scanning confocal microscope (Doeven *et al.*, 2005), as described by van den Bogaart (van den Bogaart *et al.*, 2008a, van den Bogaart *et al.*, 2007a, van den Bogaart *et al.*, 2008b). Different amounts of peptide were added to 64 µg/ml DOPG liposomal solutions, yielding final peptide-lipid ratios from 1/52 to 5/1. The samples were equilibrated for 10 minutes at room temperature after each addition of peptide. The fluorescence bursts were measured for 10 min. To estimate the size of the pore, a size marker was encapsulated inside the DiD-labeled vesicles, i.e., 10 kDa dextran labeled with fluorescein (Invitrogen).

Results

The cyclic peptide causes large perturbations in DPPG bilayers

To probe the poration propensity of BPC194, we performed simulations of the peptides interacting with a DPPG bilayer at a P:L ratio of 9:128. DPPG bilayers were chosen since the peptide is antimicrobial (characterized by anionic lipids) with low hemolytic activity (characterized by zwitterionic lipids). The time course of a particular simulation (Cirac *et al.,* 2011) is depicted in Figure 1A, but similar behavior was observed in the remaining simulations (Cirac *et al.,* 2011). The peptides were initially placed in the water layer close to the bilayer (0 ns) and subsequently bound fast (~5 ns) to the membrane interface. During the simulation, most of the peptides remained bound at the interface though, a few peptides were able to cooperatively perturb the outer leaflet and consequently insert deeper (Figure 1A, 16-60 ns). In the perturbed state, the positively-charged residues of the peptides interacted with the closest headgroup moieties and pulled them, together with some water molecules, into the core of the membrane. The peptide-free inner leaflet was also affected by the action of the cyclic peptide bound on the outer leaflet. This behavior was seen repetitively during the simulation and was usually followed by a relaxation of both leaflets. Occasionally, a much larger perturbation occurred (109 ns), characterized by a decrease in the local lipid-chain order (Cirac *et al.,* 2011). At this point, the perturbation was caused by a cooperative effect of three peptides, one of which adopted a transmembrane-orientation with its glutamine residue close to the centre of the hydrophobic core. In this position, the glutamine residue interacted with some head-group atoms of the inner leaflet. During this perturbation, a few water molecules were able to cross the membrane. However, the inner leaflet relaxed again and the orientation of the glutamine residue reverted back to the interface (Figure 1A, 115 ns). Only smaller perturbations of the membrane were observed in the remainder of the simulation.

The cyclic peptide can form a disordered toroidal pore.

In our previous simulations of AMP action (Leontiadou *et al.*, 2006, Sengupta *et al.*, 2008), the first event during pore formation was the bridging of the two leaflets by a peptide. Although such an orientation of the peptides was seen in simulation 9Ca (Figure 1A, 109 ns), it did not lead to a porated state. Nevertheless, we expect this highly perturbed state to be an intermediate, mimicking the transition state toward pore formation. To sample the conformational space around this so-called “transition state”, ten simulations were set up; the velocities in the system were varied to provide a different direction on the potential energy surface that may lead to pore formation. Indeed, a pore was formed in six out of ten simulations; for details see (Cirac *et al.,* 2011). The mechanism of the pore formation is depicted in Figure 1B, using C9 as a representative of all simulations. The first time point (0 ns) was taken as the transition state from which the simulation was started (cf. Figure 1A, 109 ns). Water molecules readily inserted into the bilayer and finally after 1~2 ns, some water molecules crossed the bilayer to open a water channel. Head-group atoms of both leaflets moved inside the membrane core to line the water channel. From then on, the pore remained open and the lipid head-groups of both leaflets rearranged to form a disordered toroidal-shaped pore around 25 ns. The size of the water channel fluctuated both in time as well as along the direction of the pore axis, ranging between ~1 and 2 nm (see Figures 1B, 65 ns and (Cirac *et al.,* 2011)). The pores formed in our simulations could be characterized as disordered toroidal pores with the peptides residing in different positions and orientations. In all cases, the pore was stabilized by three peptides; a dimer and a monomer, with the remain-

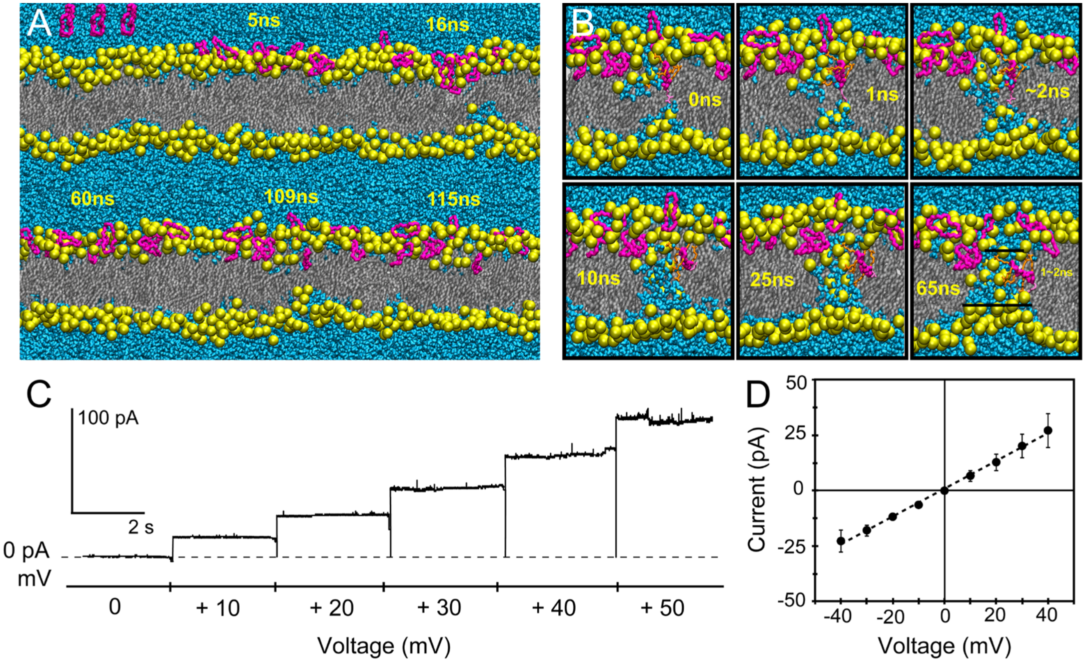

Figure 1. The cyclic peptides cause large fluctuations in the membrane upon binding and can form a disordered toroidal pore. A. Time course of the simulation 9Ca. At 0 ns all peptides were placed close to the bilayer and they bound within 5 ns. The first perturbation of the inner leaflet was seen at 16 ns, when some lipids were pulled into the bilayer due to the action of the cyclic peptide. The highest perturbation was at 109 ns and involved three peptides, one of which adopts a transmembrane orientation. The inner leaflet relaxed at 115 ns. B. The snapshot of the transition state (Fig. 1, 109ns) was taken as the starting structure (0 ns). An increase of the number of water molecules inserting into the bilayer was followed by the opening of a water channel (1-2 ns) and insertion of lipid head-groups further inside to form a toroidal-shaped pore (10-25 ns). A stable toroidal-shaped pore was seen at 65 ns. The head-groups are depicted in yellow spheres. The peptide backbone is shown in pink, lipid tails in grey and water molecules in cyan. To clarify the briding of the two leaflets from transition state and on, the lysine residues (orange) and the glutamine residue (light pink) are shown only for the peptide in a transmembrane orientation. C. Current traces recorded after the addition of BPC194 peptide to DOPG membranes. D. I-V curves plotted from seven independent current trace recordings of BPC194.

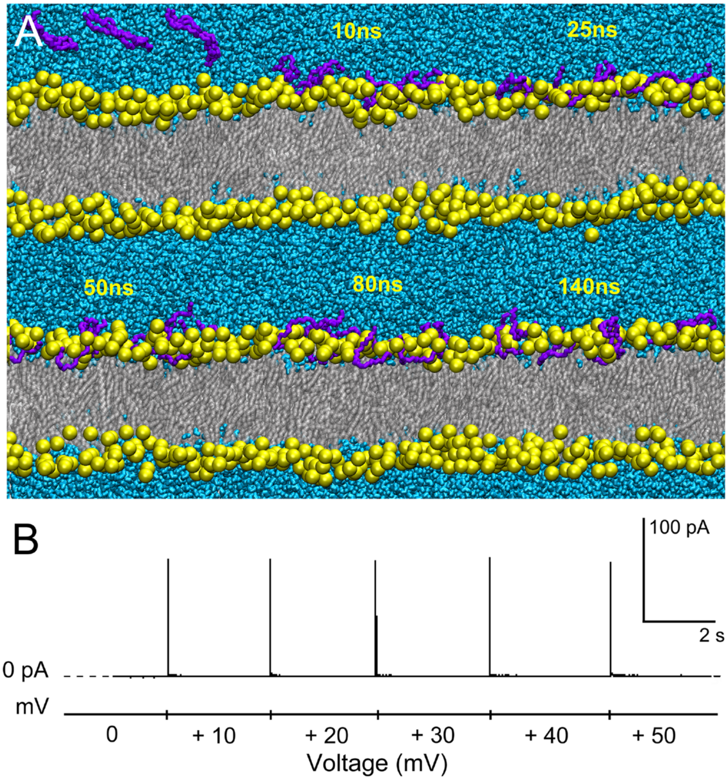

Figure 2. The linear peptides do not induce fluctuations in the membrane. A. Time course of the simulation L9a. Initially (0 ns), all linear peptides were placed close to the outer leaflet. Within 10 ns all peptides bound and remained at the membrane interface. No large perturbations were seen along the simulation (25-140 ns). The head-groups of DPPG are depicted in yellow spheres, the peptide backbone in violet and lipid tails in grey. B. Current traces recorded after the addition of BPC193 peptide to DOPG membranes

ing peptides lying close to the pore. No peptide translocation was seen in the nanosecond time regime of the simulations.

Electrophysiology revealed that pore formation is specific for cyclic peptides

To monitor the pore formation of BPC194 ion fluxes in a planar lipid bilayer setup were measured. An example of a current trace recorded upon addition of BPC194 to the *cis* compartment of the planar lipid bilayer setup is shown in Figure 1C. A voltage-dependent conductance was observed implying that a pore or channel was formed/opened. These conductance events were stable during the course of the recording, pointing towards the formation of discrete pores. The average I-V curve of all independent recordings is plotted in Figure 1D. The pore has an average unitary pore conductance of 0.61 ± 0.12 nS. Since the I-V curve is symmetric the pores formed by BPC194 are not ion selective. The diameter of the pore was estimated (see Eq. 1 from Materials and Methods) to range between 1.5-1.9 nm.

At higher peptide concentrations, we also observed higher overall conductance that was a multiple of the unitary conductance, reflecting the higher probability of pore formation. The same increase in probability of pore formation was observed on applying voltages higher than ± 50 mV. However, these extra poration events were transient with shorter dwell times.

The linear peptide does not perturb or porate DPPG bilayers substantially

Simulations of the linear analogue interacting with DPPG bilayers were performed under conditions identical to the cyclic peptide (Cirac *et al.,* 2011). A typical time course of the simulation is depicted in Figure 2A. Upon binding, the linear peptides somewhat perturb the membrane, albeit much less than the cyclic ones. Larger perturbations leading to a transition state were not seen in any of the simulations with the linear peptide. Though the average thickness of the bilayer is similar for the two peptides (3.7 ± 0.1 nm for the linear and 3.6 ± 0.1 nm for the cyclic peptide), the perturbations in the outer leaflet are substantially higher when the cyclic peptide is attached. The fluctuations in the outer leaflet, calculated as the deviation of the phosphorus atoms of the head-groups from their center of mass are ± 0.44 nm for the cyclic peptide in comparison to ± 0.29 nm for the linear peptide. These results were supported by the electrophysiology measurements, in which the linear analogue did not show pore formation or ion flux through the membrane at the same voltage regime in which the cyclic peptide formed pores (Figure 2B).

Structure-Function relationship of the cyclic peptide.

To investigate the relation between secondary structure and the ability of the peptides to stabilize a pore, we clustered the peptides depending on how far they lie from the pore and the role they play in stabilizing it (Figures 3A and 3B). Three classes of peptides were distinguished: those within the rim of the pore (distance 0.3 nm from the center of the pore, region 1), those lying at the mouth of the pore (within 0.3-1.5 nm, region 2) and those not involved in the pore (further away than 1.5 nm, region 3) (Table 1). Peptides in region 1 adopt a stable secondary structure (40% b-structure) in all simulations where a pore is formed (six simulations). Although the number of residues involved in secondary structure varied between the three peptides, all three showed the longest persistence of β-structure over time (97%). The peptides belonging to region 2 also exhibited a high b-structure (39% for peptides of this region), but the percentage fluctuated over time and the persistence of b-structure was 89%. Finally, the peptides in region 3 exhibited multiple folds and adopted different conformations showing only 18% b-structure for the individual peptides.

The apparent importance of the b-structure for stabilization of the pore can be rationalized by considering the relative orientation of the lysine residues. As illustrated in Figure 3C, the b-structure gives rise to a parallel arrangement of the lysine pairs (K^1-K^8 and K^2-K^7) on the two strands that, presumably, facilitates the interaction of the lysines with the lipid head-groups in the curved geometry of the pore (Figure 3D). The distances between the lysine pairs K^1-K^8 and K^2-K^7 (plotted as a sum of the two values) for the three regions of the peptides is shown in Figure 3E. When the peptides are bound to the membrane (0-109 ns, till grey

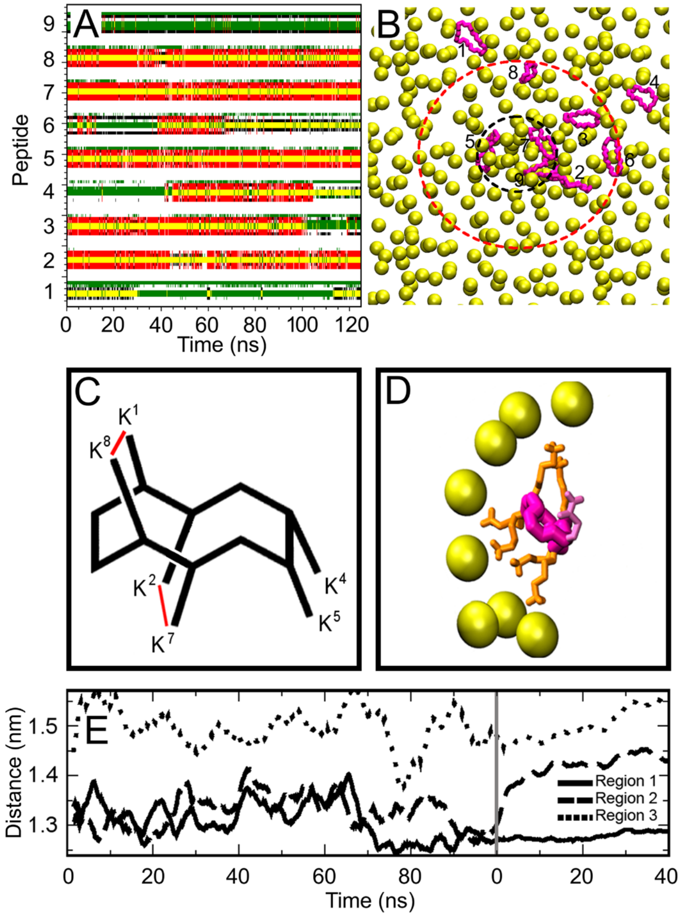

Figure 3. Secondary structure related to the distance at the rim of the pore and its function. A: DSSP plot of the secondary structure of all peptides for simulation C9, taking the transition state as the 0 ns time point. B: Top view of the pore showing the positions of the nine peptides. The phosphorus atoms of the outer leaflet are depicted as yellow spheres and the backbone is colored in pink. Region 1 peptides are those involved in the pore (within dashed black line). The peptides that remain at the rim of the pore (region 2) are delimited by the red dashed line. The peptides furthest from the pore (region 3) are outside the circles. C: Parallel arrangement of lysine residues in the β-structure D: An example of the aligned lysine residues stabilizing the lipid curvature in the porated state (side-view of the pore). E: The average distance between lysine residues K1-K8 and K2- K7 (plotted as a sum) for peptides in regions 1, 2 and 3. The time scale to the left of the grey line refers to simulation 9Ca (before transition state formation 0-109 ns). The time frame to the right is an average for all simulations (C1-10) where a pore was formed with the starting time 0 ns being the putative transition state.

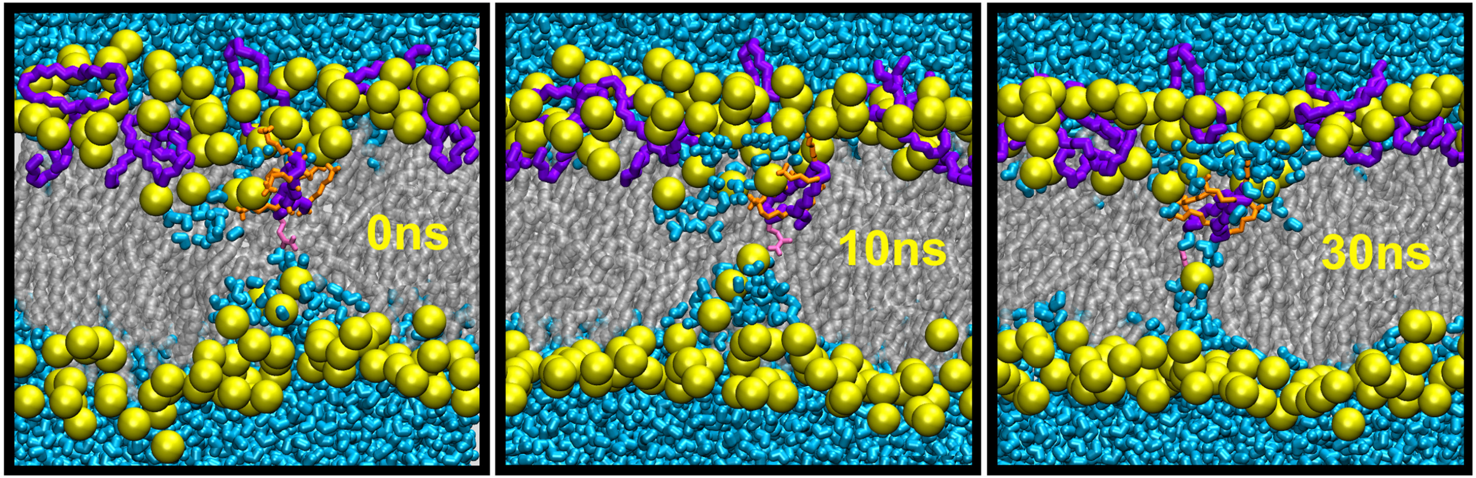

Figure 4. The linear peptides cause large perturbations from the in-silico modified transition state. Time course of a transient pore formed by a linear peptide (simulation L7). The time point 0 ns corresponds to the transition state taken from the simulation with the cyclic peptide. After 10-30 ns, large perturbations were seen and a few water molecules crossed the bilayer. Please note that in most simulations the bilayer relaxes and such large perturbations are not seen.

Region	Peptide	Distance (nm)	% Coil	% β-structure	% Bend	% Turn	% Time of β-structure
1	5	0.09 ± 0	20.7	45.7	10.3	23.4	94.8
	7	0.09 ± 0	19.6	47.9	8.4	24.1	98.4
	9	0.09 ± 0	25.2	26.2	45.4	3.4	97.7
	Average	0.09 ± 0	22 ± 1	40 ± 6	31 ± 11	17 ± 6	97 ± 1
2	2	0.30 ± 0.05	29.9	43.8	2.8	23.6	92
	3	0.78 ± 0.15	24.8	42.8	12.0	20.4	92.6
	6	1.10 ± 0.15	36.0	32.2	14.2	16.5	91.7
	8	1.50 ± 0.23	30.0	39.1	10.9	20.0	78.1
	Average	0.9 ± 0.2	30 ± 2	39 ± 2	10 ± 2	20 ± 1	89 ± 3
3	4	1.59 ± 0.30	38.5	28.1	15.3	18.2	62.5
	1	2.07 ± 0.25	45.4	8.6	30.9	15.1	33.6
	Average	1.8 ± 0.2	42 ± 2	18 ± 7	23 ± 6	17 ± 1	48 ± 10

Table 1. Secondary structure and distance from the centre of the pore for the peptides belonging to the three regions. The values reported are an average calculated from all simulations where a pore was formed. The time of persistence of β-structure (see Materials and Methods) is also reported. The standard errors reported are calculated from the standard deviation, between all peptides in all simulations.

Pore features	Cyclic peptide	Linear peptide
Pore propensity	High	Low
Pore diameter	1-2 nm	< 1 nm
Number of peptides inside	3	1
% β-structure	34 %	21 %
Outer leaflet deviation	± 0.55	± 0.48
Number of porated states	6/10	3/10
Number of lipid head-groups	8-11	6-10
Number of water molecules	100-123	76-84
Formation time	1-4 ns	3-30 ns

Table 2. Summary of pore features created by the cyclic peptide and the linear peptide.

line), the value fluctuates for all three clusters of peptides. However, once the transition state is reached and later when a pore is opened (beyond grey line), the distance between the lysine pairs in the peptides in region 1 remained low, consistent with their high persistence of secondary structure. The value for the peptides in region 2 was also low at the transition state but increases as the pore relaxes. The peptides in region 3, which were not involved in the pore, showed the largest distance between the lysine pairs along the simulations.

Transition state alchemy: Why the linear peptide cannot stabilize pores.

To test whether the b-strand conformation is indeed linked to activity, we repeated the simulations from the transition state with the linear peptide by in-silico alchemy, i.e. removing the peptide bond between the first and last residue. The results of these simulations are summarized in (Cirac *et al.,* 2011). In seven of the ten simulations, the bilayer relaxed and the linear peptide moved back to the interface. In the remaining three simulations, a water channel eventually opened. The time course of one of the poration events (L7) is depicted in Figure 4. Although we observed that the linear peptide is also able to stabilize a water pore (starting from the perturbations caused by the cyclic peptide), the pore differs from the pore formed in the presence of the cyclic peptides: i) Only one of the three peptides involved in the transition state remained embedded near the central pore region; and ii) The lipid head-groups did not line the pore as clearly as in the case of the cyclic peptide.

In most of the simulations, the average percentage of β-structure dropped to a value around 20%, compared to > 30% for the cyclic peptide (Cirac *et al.,* 2011). In the simulations in which a pore was formed, the peptide in closest vicinity of the pore preserved a somewhat higher percentage of b-structure (~28%). Two additional unbiased transition state simulations of the linear peptide in its native random-coil conformation were performed. We found that, in the extended conformation, the peptide could not stabilize even those head-groups that were already inserted into the membrane, and the bilayer recovered immediately from the large perturbations induced by the cyclic peptide. An overview of the poration features of the cyclic and linear peptide is presented in Table 2.

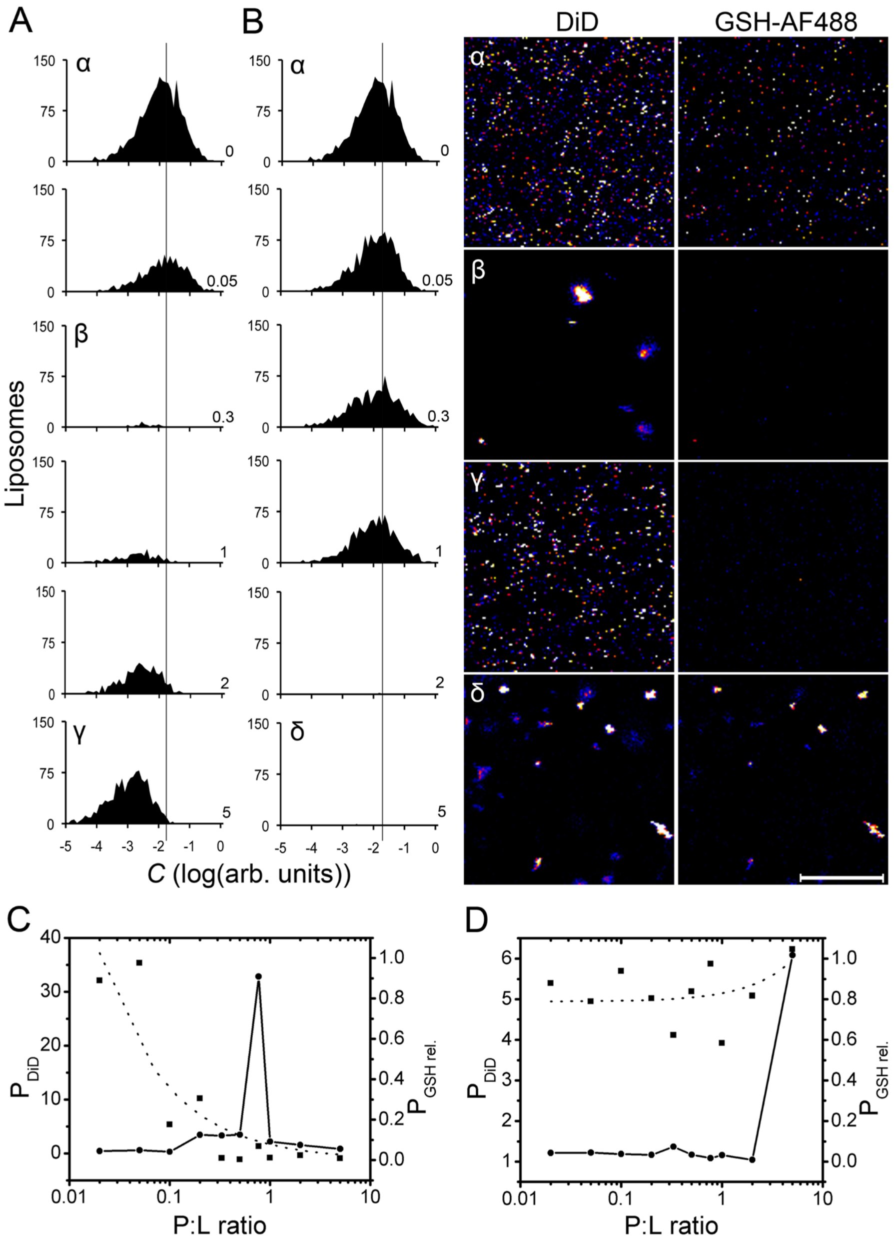

***Figure 5. Mechanism of action of peptides studied by DCFBA**.* A-B. DCFBA population histograms of BPC194 and BPC193, respectively. The numbers in the bottom right of the graphs refer to P:L ratios. The y-axis corresponds to the number of liposomes, the x-axis to the arbitrary marker concentration inside the liposomes. Top right panels: Confocal images of vesicles probed in the experiments shown in (A) and (B), indicated by Greek symbols (α-δ); left panels: membrane probe, DiD; right panels: internal marker probe, GSH-AF488. The scale bar is 20 μm. C-D. Average DiD population (circles, solid line) and relative GSH population (squares, dotted line) for the cyclic and the linear peptide, respectively.

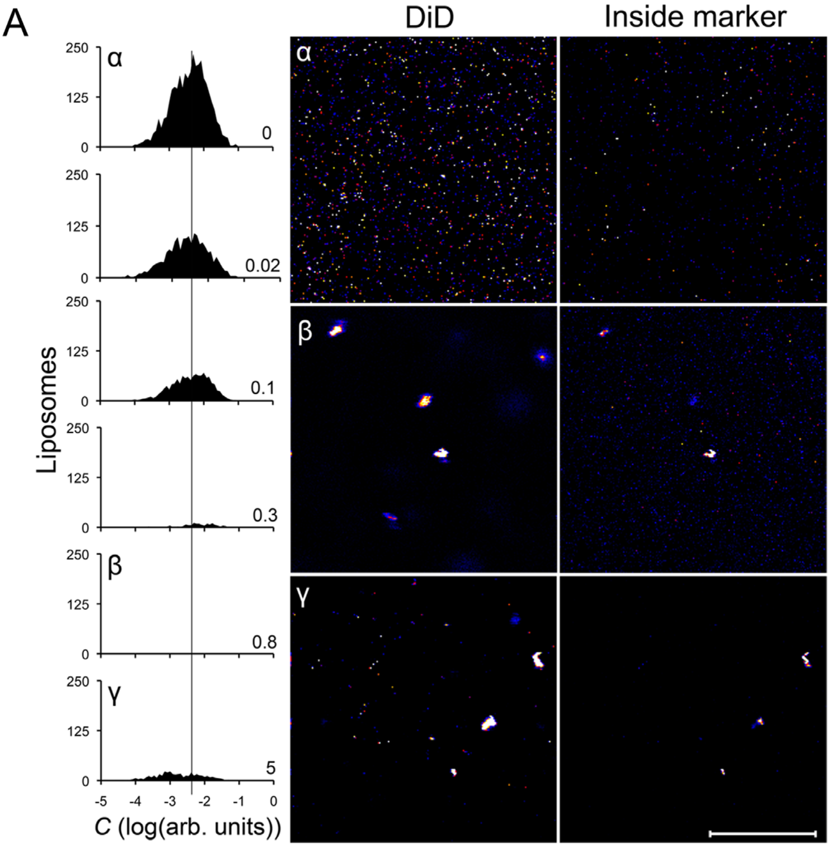

B

Molecule	Mw (Da)	Calculated Diameter[1] (nm)	Diameter measured by FCS[2] (nm)	Other estimated Dimension
GSH–AF488	1027	1.35	1.67 +/- 0.25	n.d.
10 kDa Dextran-Fluorescein	~ 10 000	2.86	5.35 +/- 0.8	2.12 x 8.48[3]

Figure 6. 10 kDa Dextran does not leak through the pore formed by BPC194. A. DCFBA experiment of the peptide BPC194 with DiD-labeled vesicles and 10 kDa Dextran-Fluorescein as internal marker. Left: BPC194 induces liposome fusion/aggregation without leakage. Right: Confocal images of vesicles probed in the DCFBA experiments. Panel α represents the intact vesicles, panel β shows a P:L ratio where the peptide caused fusion/aggregation without leakage, and panel γ shows a P:L ratio where little fusion/aggregation was observed and the vesicles did not leak. The scale bar is 20 μm. B. Dimensions of internal size marker molecules.

[1] Calculated on the basis of molecular weight (see Chapter 4).

[2] The diffusion coefficient was determined in water at 20°C by fluorescence correlation spectroscopy (FCS), as described previously (Veldhuis et. al., 2006). The Stokes radius was calculated from the *D* values, using the Einstein-Stokes relationship (see Chapter 4).

[3] The dextran is assumed to be a prolate elipsoid with an axial ratio of 4 (Bohrer et. al., 1979; for a 9.5 kDa Dextran). The semi-minor axis (α) and semi-major axis (β) are calculated using the r_s, measured in this work by FCS, from the dependence:

$$r = \left(\alpha\beta^2\right)^{1/3}$$

The dimensions of the dextran molecules should be taken with caution since they are not spherical and may lose their water shell while passing through the pore.

DCFBA reveals the mechanism of action on liposomes.

Figure 5 shows the result of DCFBA experiments carried out with BPC194 and BPC193 in the presence of DiD-labeled DOPG vesicles filled with the internal marker, GSH-AF488. In such an experiment, poration of liposomes reduces the internal marker concentration and the DCFBA population histogram shifts to lower concentration values. In contrast, membrane fusion or aggregation results in a decrease in the number of detected liposomes, which is observed as a decrease in the area of the population histogram. For the cyclic analogue, at low P:L ratios (≤ 1), the number of liposomes decreased, which is indicative of fusion or aggregation (Figure 5A). The membrane fusion/aggregation activity was confirmed by confocal imaging of the liposomes and was accompanied by leakage of the internal marker (Figure 5A, panel b, P:L ratio of 0.3). Intriguingly, adding an excess of peptide (P:L ratios of 1-5) such that the vesicles are completely shielded by peptide preventing aggregation/fusion, the number of detected liposomes was restored and the concentration of molecules inside the liposomes dropped (Figure 5A, panel g), which is indicative of pore formation. The linear peptide, BPC193 also caused membrane fusion or aggregation but at higher P:L ratios than its cyclic counterpart (Figure 5B). This was confirmed by confocal imaging at the highest concentration of the linear peptide (P:L ratio of 5) where large membrane aggregates were formed without loss of the internal marker, indicative of the lack of pore formation (Fig. 5A, panel d).

To present the overall data comprehensively, the average membrane fluorescence per liposome and the relative concentration of the internal marker are plotted in Figures 5C and 5D (see Materials and Methods for more details).

For BPC194, the average membrane fluorescence peaked at a P:L ratio of 0.5-1, while the relative concentration of the internal marker already dropped to zero at a P:L of 0.3. This behavior confirms the leaky fusion/aggregation action of the cyclic peptide. On the other hand, for BPC193, an increase in the membrane population and constant relative internal marker population was seen, thereby corroborating its non-leaky fusion/aggregation propensity.

Using the DCFBA technique and encapsulating bigger internal markers we could estimate the size of the pore. The smallest molecule that did not leak out was the 10 kDa Dextran-Fluorescein (Fig. 6) with a dimension of 2.1 nm (shortest axis measured assuming is a prolate ellipsoid), while GSH-AF488 leaked out with a diameter of ~1.7 nm (Fig. 6B, measured by FCS). We conclude that the size of the pore is between 1.7 and 2.1 nm.

Discusssion

Nature of the transition state.

The simulations presented here elucidate the nature of the transition state of the poration process. One may assume that starting from a true transition state, the chance of arriving at either side of the transition state barrier is approximately equal (here the porated membrane versus the intact membrane). Although our statistics are necessarily limited, we observe 6 out of 11 simulations with the cyclic peptide to reach a porated state, starting from the state in which a large perturbation was observed in the original simulation (Cirac *et al.,* 2011). In the remaining 5 out of 11 simulations, counting also the original trajectory, the system relaxed back to the intact membrane state. This intermediate or transition state is characterized by a single peptide bridging the two leaflets (cf. Figure 1B, 0 ns). The results are in line with kinetic models that suggest that such a state is important in pore formation (Gregory *et al.*, 2008).

Disordered toroidal pore.

Using the transition state as seed for many independent trajectories, we were able to show that the deepest-embedded peptides may stabilize a toroidal-shaped pore of 1-2 nm diameter, which is in line with the electrophysiology and pore-sizing DCFBA experiments. Only two/three peptides actually lie in the pore while some of the remaining peptides line the mouth of the pore and stabilize the membrane curvature. The structure of the pore is reminiscent of pores seen in previous MD studies (Jean-François *et al.*, 2008, Leontiadou *et al.*, 2006, Rzepiela *et al.*, 2010, Sengupta *et al.*, 2008) and has been termed the disordered toroidal pore.

Structure-function relationship.

The simulations also highlight the importance of secondary structure in stabilizing the porated state. In the simulations, a constrained secondary structure rather than a high percentage of secondary structure was required to stabilize the pore. The importance of the secondary structure, induced on membrane binding and stabilized in the porated state, appears to be the alignment of the charged residues such that they fit the toroidal shape of the pore (cf. Figure 3D). This explains why the linear peptide is less active – for entropic reasons a folded structure is less favorable. This entropic penalty is 'prepaid' by the cyclic peptide. Thus, the linear peptide cannot open a pore but may stabilize it, if the starting structure is the transition state structure obtained with the cyclic peptide (cf. Figure 4).

Conductance, pore properties and fusion/aggregation.

BPC194 forms stable and non-selective ion pores in planar lipid bilayer experiments, with a unitary conductance of 0.61 ± 0.12 nS, corresponding to a pore diameter of 1.5-1.9 nm. This is in contrast to other cyclic peptides such as gramicidin S that do not form stable pores (Ashrafuzzaman *et al.*, 2008). Stable pores have however been seen for linear antimicrobial peptides such as alamethicin, magainins and defensins (Duclohier *et al.*, 1989). Both the cyclic and linear peptides are fusogenic or cause aggregation, as indicated by DCFBA measurements, but only the cyclic peptide caused leakage as well. Similar to melittin (van den Bogaart *et al.*, 2007b), BPC194 causes leakage at the same concentration regime at which it fuses or aggregates DOPG membranes. However, further studies in this intriguing fusion/aggregation action are in progress.

Conclusions

There is now compelling evidence that cyclization of certain sequences of membrane-active peptides enhances their antimicrobial performance. In this paper, we analyze the molecular basis for the differences in activity of analogous cyclic and linear antimicrobial peptides. We show that the molecular basis for the enhanced activity resides most likely in the restriction of the number of conformations in the cyclic peptide. We show that it can adopt a favorable orientation towards the membrane and acquire an ordered structure that allows a high charge density and amphipathic arrangement. The latter allows the cyclic peptide to perturb the membrane substantially and to form discrete pores. Cyclization of the linear sequence locks the peptide in a poration-ready state, allowing it to perturb the bilayer and stabilize the curvature of a toroidal transmembrane pore. Without cyclization, entropy destabilizes the formation of a folded structure and consequently its amphipathic-like character and hence the linear peptide has a much lower propensity to induce pores. The work presented here provides detailed insight into the mode of action of cyclic peptides and will aid rational design of new antimicrobial molecules.

Acknowledgements

We thank LIPPSO group (University of Girona), for help with the synthesis of the peptides. We acknowledge financial support from the Spanish MICINN (MAT2008-04834 to ADC and PS) and MEC (BES-2006-11671 doctoral fellowship to ADC), the Netherlands NWO (DS, SJM), SysMo via the BBSRC-funded KosmoBac programme (BP), NWO (Top-subsidy grant 700.56.302 to BP), NWO-Vidi (AK), ERC-Starting grant (AK) and the Zernike Institute for Advanced Materials to support the appointment and research of GMC and JTM.

References

Anézo, C., A. H. de Vries, H. D. Höltje, D. P. Tieleman & S. J. Marrink, (2003) Methodological issues in lipid bilayer simulations. *J. Phys. Chem. B* **107**: 9424-9433.

Ashrafuzzaman, M., O. S. Andersen & R. N. McElhaney, (2008) The antimicrobial peptide gramicidin S permeabilizes phospholipid bilayer membranes without forming discrete ion channels. *Biochim. Biophys. Acta* **1778**: 2814-1822.

Berendsen, H. J. C., J. P. M. Postma, W. F. van Gunsteren & J. Hermans, (1981) Interaction models for water in relation to protein hydration. *Intermolecular Forces*: 331-342.

Berendsen, H. J. C., J. P. M. Postma, W. F. van Gunsteren, A. D. Nola & J. R. Haak, (1984) Molecular dynamics with coupling to an external bath. *J. Chem. Phys.* **81**: 3684-3690.

Brogden, K. A., (2005) Antimicrobial peptides: Pore formers or metabolic inhibitors in bacteria? *Nat. Rev. Microbiol.* **3**: 238-250.

Brogden, K. A., M. Ackermann, P. B. J. McCray & B. F. Tack, (2003) Antimicrobial peptides in animals and their role in host defences. *Int. J. Antimicrob. Agents* **22**: 465-478.

Case, D. A., T. A. Darden, T. E. Cheatham III, C. L. Simmerling, J. Wang, R. E. Duke, R. Luo, K. M. Merz, D. A. Pearlman, M. Crowley, R. C. Walker, W. Zhang, B. Wand, S. Hayik, A. Roitberg, G. Seabra, K. F. Wong, F. Paesani, X. Wu, S. Brozell, V. Tsui, H. Gohlke, L. Yang, C. Tan, J. Mongan, V. Hornak, G. Cui, P. Beroza, D. H. Mathews, C. Schafmeister, W. S. Ross & P. A. Kollman, (2006) AMBER 9. In. University of California, San Francisco, pp.

Cirac, A.D., Moiset, G., Mika, J.T., Kocer, A., Salvador, P., Poolman, B., Marrink, S.J.and D. Sengupta, (2011) The molecular basis for antimicrobial activity of pore-forming cyclic peptides. *Biophys. J.* **100**: 2422-2431.

Cruickshank, C. C., R. F. Minchin, A. C. Le Dain & B. Martinac, (1997) Estimation of the pore size of the large-conductance mechanosensitive ion channel of *Escherichia coli*. *Biophys. J.* **73**: 1925-1931.

Doeven, M. K., J. H. Folgering, V. Krasnikov, E. R. Geertsma, G. van den Bogaart & B. Poolman, (2005) Distribution, lateral mobility and function of membrane proteins incorporated into giant unilamellar vesicles. *Biophys. J.* **88**: 1134-1142.

Duclohier, H., G. Molle & G. Spach, (1989) Antimicrobial peptide magainin I from *Xenopus* skin forms anion-permeable channels in planar lipid bilayers. *Biophys. J.* **56**: 1017-1021.

Epand, R. M. & H. Vogel, (1999) Diversity of antimicrobial peptides and their mechanism of action. *Biochim. Biophys. Acta* **1462**: 11-28.

Ferre, R., M. N. Melo, A. D. Correia, L. Feliu, E. Bardaji, M. Planas & M. A. R. B. Castanho, (2009) Synergistic effects of the membrane actions of cecropin-melittin antimicrobial hybrid peptide BP100. *Biophys. J.* **96**: 1815-1827.

Gibbs, A. C., L. H. Kondejewski, W. Gronwald, A. M. Nip, R. S. Hodges, B. D. Sykes & D. S. Wishart, (1998) Unusual beta-sheet periodicity in small cyclic peptides. *Nat. Struct.*

Biol. **5**: 284-288.

Gregory, S. M., A. Cavenaugh, V. Journigan, A. Pokorny & P. F. F. Almeida, (2008) A quantitative model for the all-or-non permeabilization of phospholipid vesicles by the antimicrobial peptide Cecropin A. *Biophys. J.* **94**: 1667-1680.

Hancock, R. E. W. & D. S. Chapple, (1999) Peptide Antibiotics. *Antimicrob. Agents Ch.* **43**: 1317-1323.

Hancock, R. E. W. & A. Rozek, (2001) Role of membranes in the activities of antimicrobial cationic peptides. *FEMS Microbiol. Lett.* **206**: 143-149.

Hille, B., (1968) Pharmacological modifications of hte sodium channels of frog nerve. *J. Gen. Physiol.* **51**: 199-219.

Hille, B., (2001) Ionic channels of excitable membranes. In: Ionic channels of excitable membranes. Sunderland: Sinauer Associates, Inc, pp.

Huang, H. W., (2000) Action of antimicrobial peptides: Two-state model. *Biochemistry* **39**: 8347-8352.

Huang, H. W., (2004) Molecular mechanism of peptide-induced pores in membranes. *Phys. Rev. Lett.* **92**: 1-4.

Huang, H. W., (2006) Molecular mechanism of antimicrobial peptides: The origin of cooperativity. *Biochim. Biophys. Acta* **1785**: 1292-1302.

Jean-François, F., J. Elezgaray, P. Berson, P. Vacher & E. Dufourc, (2008) Pore formation induced by antimicrobial peptide: Electroestatic effect. *Biophys. J.* **95**: 5748-5756.

Jelokhani-Niaraki, M., R. S. Hodges, J. E. Meissner, U. E. Hassenstein & L. Wheaton, (2008) Interaction of gramicidin S and its aromatic amino-acid analog with phospholipid membranes. *Biophys. J.* **95**: 3306-3321.

Jelokhani-Niaraki, M., E. J. Prenner, C. M. Kay, R. N. McElhaney & R. S. Hodges, (2002) Conformation and interaction of the cyclic cationic antimicrobial peptides in lipid bilayers. *J. Pept. Res.* **60**: 23-36.

Jenssen, H., P. Hamill & R. E. W. Hancock, (2006) Peptide Antimicrobial Agents. *Clin. Microbiol. Rev.* **19**: 491-511.

Kabsch, W. & C. Sander, (1983) Dictionary of protein secondary structure: Pattern recognition of hydrogen-bonded and geometrical features. *Biopolymers* **22**: 2577-2637.

Khalfa, A. & M. Tarek, (2010) On the antibacterial action of cyclic peptides: Insights from coarse-grained MD simulations. *J. Phys. Chem. B* **114**: 2676–2684.

Lee, D. L. & R. S. Hodges, (2003) Structure-activity relationship of de novo designed cyclic antimicrobial peptides based on gramicidin S. *Biopolymers* **71**: 28-48.

Leontiadou, H., A. E. Mark & S. J. Marrink, (2006) Antimicrobial peptides in action. *J. Am. Chem. Soc.* **128**: 12156-12161.

Ludtke, S. J., K. He, W. T. Heller, T. A. Harroun, L. Yang & H. W. Huang, (1996) Membrane pores induced by magainin. *Biochemistry* **35**: 13723-13728.

Mak, D. O. D. & W. W. Webb, (1995) Two classes of alamethicin transmembrane channels:

Molecular models from single-channel properties. *Biophys. J.* **69**: 2323-2336.

Matsuzaki, K., (2009) Control of cell selectivity af antimicrobial peptides. *Biochim. Biophys. Acta* **1788**: 1687-1692.

Mátyus, E., C. Kandt & D. P. Tieleman, (2007) Computer simulations of antimicrobial peptides. *Curr. Med. Chem.* **14**: 2789-2798.

Melo, M. N., R. Ferre & M. A. R. B. Castanho, (2009) Antimicrobial peptides: Linking partition, activity and high membrane-bound concentrations. *Nat. Rev. Microbiol.* **7**: 245-250.

Mihailescu, D. & J. C. Smith, (1999) Molecular dynamics simulation of the cyclic decapeptide antibiotic, gramicidin S, in dimethyl sulfoxide solution. *J. Phys. Chem. B* **103**: 1586-1594.

Mihailescu, D. & J. C. Smith, (2000) Atomic detail peptide-membrane interactions: Molecular dynamics simulation of gramicidin S in a DMPC Bilayer. *Biophys. J.* **79**: 1718-1730.

Monroc, S., E. Badosa, E. Besalú, M. Planas, E. Bardají, E. Montesinos & L. Feliu, (2006a) Improvement of cyclic decapeptides against plant pathogenic bacteria using a combinatorial chemistry approach. *Peptides* **27**: 2575-2584.

Monroc, S., E. Badosa, L. Feliu, M. Planas, E. Montesinos & E. Bardají, (2006b) De novo designed cyclic cationic peptides as inhibitors of plant pathogenic bacteria. *Peptides* **27**: 2567-2574.

Mueller, P., D. O. Rudin, H. T. Tien & W. C. Wescott, (1962a) Reconstitution of cell membrane structure *in vitro* and its transformation into an excitable system. *Nature* **194**: 979-980.

Mueller, P., D. O. Rudin, H. T. Tien & W. C. Wescott, (1962b) Reconstitution of excitable cell membrane structure *in vitro*. *Circulation* **26**: 1167-1171.

Mueller, P., D. O. Rudin, H. T. Tien & W. C. Wescott, (1963) Methods for the formation of single biomolecular lipid membranes in aqueous solution. *J. Phys. Chem.* **67**: 534-535.

Pabst, G., S. Danner, S. Karmakar, G. Deutsch & V. A. Raghunathan, (2007) On the propensity of phosphatidylglycerols to form interdigitated phases. *Biophys. J.* **93**: 513-525.

Prenner, J. E., R. N. A. H. Lewis & R. N. Mcelhaney, (1999) The interaction of the antimicrobial peptide gramicidin S with lipid bilayer model and biological membranes. *Biochim. Biophys. Acta* **1462**: 201-221.

Qian, S., W. Wang, L. Yang & H. W. Huang, (2008) Structure of the alamethicin pore reconstructed by X-ray diffraction analysis. *Biophys. J.* **94**: 3512-3522.

Rzepiela, A. J., D. Sengupta, N. Goga & S. J. Marrink, (2010) Membrane poration by antimicrobial peptides combining atomistic and coarse-grained descriptions. *Faraday discuss.* **144**: 431-443.

Salay, L. C., J. Procopio, E. Oliveira, C. R. Nakaie & S. Schreier, (2004) Ion channel-like activity of the antimicrobial peptide tritrpticin in planar lipid bilayers. *FEBS Lett.* **565**: 171-175.

Seelig, J., (2004) Thermodynamics of lipid-peptide interactions. *Biochim. Biophys. Acta* **1666**: 40-50.

Sengupta, D., H. Leontiadou, A. E. Mark & S. J. Marrink, (2008) Toroidal pores formed by antimicrobial peptides show significant disorder. *Biochim. Biophys. Acta* **1778**: 2308-2317.

Shai, Y., (1999) Mechanism of the binding, insertion and destabilization of phospholipid bilayer membranes by alpha-helical antimicrobial and cell non-selective membrane-lytic peptides. *Biochim. Biophys. Acta* **1465**: 55-70.

Shai, Y., (2002) Mode of action of membrane active antimicrobial peptides. *Biopolymers* **66**: 236-248.

Subbalakshmi, C. & N. Sitaram, (1998) Mechanism of antimicrobial action of indolicidin. *FEMS Microbiol. Lett.* **160**: 91-96.

Tironi, I. G., R. Sperb, P. E. Smith & W. F. van Gunsteren, (1995) A generalized reaction field method for molecular dynamics simulations. *J. Chem. Phys.* **102**: 5451-5459.

Tossi, A., Sandri, L., Giangaspero, A, (2000) Amphipathic, alpha-helical antimicrobial peptides. *Biopolymers* **55**: 4-30.

van den Bogaart, G., J. V. Guzmán, J. T. Mika & B. Poolman, (2008a) On the mechanism of pore formation by melittin. *J. Biol. Chem.* **283**: 33854-33857.

van den Bogaart, G., V. Krasnikov & B. Poolman, (2007a) Dual-color fluorescence-burst analysis to probe protein efflux through the mechanosensitive channel MscL. *Biophys. J.* **92**: 1233-1240.

van den Bogaart, G., I. Kusters, J. Velasquez, J. T. Mika, V. Krasnikov, A. J. Driessen & B. Poolman, (2008b) Dual-color fluorescence-burst analysis to study pore formation and protein-protein interactions. *Methods* **46**: 123-130.

van den Bogaart, G., J. T. Mika, V. Krasnikov & B. Poolman, (2007b) The lipid dependence of melittin action investigated by dual-color fluorescence-burst analysis. *Biophys. J.* **93**: 154-163.

van der Spoel, D., E. Lindahl, B. Hess, G. Groenhof, A. E. Mark & H. J. C. Berendsen, (2005) GROMACS: Fast, flexible, and free. *J. Comput. Chem.* **26**: 1701-1718.

van Gunsteren, W. F., P. Krüger, S. R. Billeter, A. E. Mark, A. A. Eising, W. R. P. Scott, P. H. Hüneberger & I. G. Tironi, (1996) *Biomolecular Simulation: The GROMOS96 Manual and User Guide.*

White, S. H. & W. C. Wimley, (1999) Membrane protein folding and stability: Physical principles. *Annu. Rev. Biophys. Biomol. Struct.* **28**: 319-365.

Yang, L., T. A. Harroun, T. M. Weiss, L. Ding & H. W. Huang, (2001) Barrel-stave model or toroidal model? A case study on melittin pores. *Biophys. J.* **81**: 1475-1485.

Yeaman, M. R. & N. Y. Yount, (2003) Mechanisms of antimicrobial peptide action and resistance. *Pharmacol. Rev.* **55**: 27-55.

Yesylevskyy, S., S. J. Marrink & A. E. Mark, (2009) Alternative mechanisms for the interaction of the cell-penetrating peptides penetratin and the TAT peptide with lipid bilayers. *Biophys. J.* **97**: 40-49.

Zasloff, M., (2002) Antimicrobial peptides of multicellular organisms. *Nature* **415**: 389-395.

Zhao, W., T. Róg, A. A. Gurtovenko, I. Vattulainen & M. Karttunen, (2007) Atomic-scale structure and electrostatics of anionic palmitoyloleoylphosphatidylglycerol lipid bilayers with Na+ counterions. *Biophys. J.* **92**: 1114-1124.

CHAPTER 9

CONCLUSIONS AND PERSPECTIVES

Jacek T. Mika

Is slow diffusion really slow?

Throughout this thesis diffusion coefficients of different molecules in the cytoplasm of *E. coli* have been determined under a variety of (osmotic) conditions. The general conclusion of this and other studies ((van den Bogaart *et al.*, 2007, Konopka *et al.*, 2006, Konopka, 2009)) is that the diffusion in the bacterial cytoplasm is slow. Significantly slower than in dilute aqueous solutions and slower than in the cytoplasm of eukaryotic cells (see Table 1 and Chapter 2 and 4). If we take the diffusion coefficients and calculate how long would it take for a molecule to traverse a cell, we obtain values of 30 ms for molecules of the size of metabolites and up to 75 s for the gigantinc, from the point of view of a cell, plasmid-protein comples. This is really fast! If one now takes into account that an *E.coli* cell has an average life-time of 30 minutes, this means that the "slowly" diffusing molecules can traverse the cell many times before it divides. From this point of view macromolecule diffusion in bacteria is not really slow. To put it in a more macroscopic perspective, let's translate the values for diffusion to the 'human' scale. Let's take GFP, which as an averaged sized protein measures 2 nm, and assume a human to be 2 m long (which is quite representative for the inhabitants of the Netherlands). On the 'human' scale, the 3 μm travel of GFP corresponds to 3000 m for the 2 m person, which is according to Google maps equivalent to the distance between the Chemistry and Physics building (Nijenborgh 4) and the Aula of the Academy Building of the Rijksuniversiteit Groningen. Following this analogy, it should take the person, even if he would get lost a couple of times (random walk), only 0.5 s. Even under conditions where the diffusion is extremely slow ($D_{GFP} = 0.01\ \mu m^2/s$ in severely stressed cells), it takes GFP no more than 2,5 min to travel the equivalent 'molecular' distance.

It is believed that the high macromolecule crowding of living organisms has a significant impact on reaction rates. On the one hand fast reactions, those that are limited by diffusion, are expected to be slower in the crowded milieu of the cytoplasm. On the other hand, the elevated crowding of the cytoplasm facilitates the association of molecules, which may speed up reaction rates. Since most reactions/interactions are characterized *in vitro* in highly diluted solutions, the next step would be to actually measure reaction rates inside bacterial cells under real crowding conditions.

Relationship between the size of the molecule and its mobility in the cytoplasm

Our understanding of biology is far less deep than that of chemistry or physics. This is in part due to the fact that biological systems are much more complex and heterogeneous. We aim at standardizing biology, finding general rules and principles. One of the main goals of this PhD thesis was to establish the relationship between the molecular weight of proteins and their diffusion coefficient in the cytoplasm of live *E.coli* cells. In chapter 4, we present experiments where the diffusion coefficients for molecules of different size have been determined. In chapter 2, we evaluate our data against *in vivo* measurements of protein diffusion reported in the literature known to date.

Previously, the milieu of the cytoplasm was considered to be relatively homogeneous and viscous and was experimentally mimicked by concentrated solutions of ficol (Dix & Verkman, 2008) or polyethylene-based crowding agents. In such an environment, the mobility of molecules (translational diffusion, *D*) dropped with the increase of their molecular weight (M_w) according to the Einstein- Stokes law, similarly as in dilute aqueous solutions, i.e. the relationship between the *D* and M_w had a cubic root dependence (Fig. 1B dotted line, exp=-0.33; see also chapter 2 and 4). When people have started to measure the mobility of molecules in living cells, it turned out that the cytoplasm is not viscous, but rather a dense, crowded solution where molecules push their way through the crowd in order to travel (Dix & Verkman, 2008). In such an environment, the translational diffusion drops with molecular weight, but the mobility of larger molecules is more restricted than that of smaller ones. The results presented in chapter 4 together with data published at the same time (Kumar *et al.*, 2010, Nenninger *et al.*, 2010) are an attempt to quantify this dependence *in vivo.*

In a computation study of the diffusion of proteins in the cytoplasm of *E.col* at a macromolecular crowding similar to that of real cells, McGuffe and Elcock (McGuffee & Elcock, 2010) have calculated the diffusion of some 50 pro-

Molecule name	Mw [kDa]	D $_{water}$ [μm^2/s]	D $_{cytoplasm\ of\ E.\ coli}$ [μm^2/s]	Time to traverse the bacterial cell [s]*
NBD-glucose	0.3	400	50	0.03
GFP	27	81	3	0.5
$(\beta$-gal-GFP$)_4$	588	10^{**}	0.8	2
Protein-plasmid complex	~25 000	n.d.	0.02	75

* assuming 3D diffusion and that the *E.coli* is 3 μm long

**guesstimate based on data for similarly sized dextrans

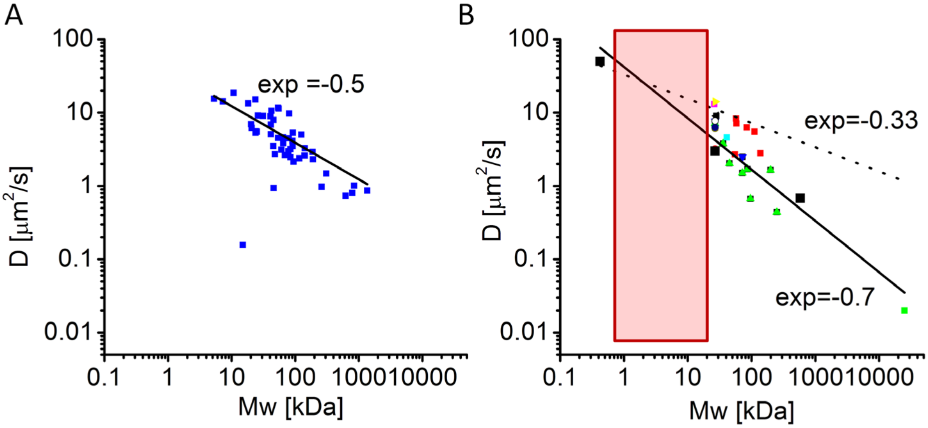

Figure 1. Dependence of diffusion coefficient on molecular weight of molecules in the cytoplasm of Escherichica coli. A: Data obtained from *in silico* experiments from the group of Adrian Elcock ((McGuffee & Elcock, 2010) with permission) B: Combined experimental data as in Chapter 2. Solid line: best fit; dashed line: fit according to the Einsiten-Stokes relationship. Red rectangle: a window between 0.6 and 27 kDa were no data is available.

teins ranging in their molecular weight from 5 to 1355 kDa (Fig. 1A). The computed values are quite similar to the data presented in chapter 2. Comparison of the *in silico* data with the combined *in vivo* experimental data (Fig. 1) demonstrates that the dependence of protein lateral diffusion on molecular weight is steeper than predicted by the Einstein- Stokes relationship. For now it seems that the D versus M_w has an exponent between -0.5 and -0.7 (see also Chapter 2 and 4).

However, it should be stressed that other authors find their data to be in good agreement with the Einsiten-Stokes law (Nenninger *et al.*, 2010) or, on the contrary, observe even steeper dependencies (Kumar *et al.*, 2010). At this moment, we are limited to fluorescence microscopy-based techniques to estimate diffusion coefficients *in vivo*, which may skew the data (e.g. because of limitations in the fluorescent labeling of proteins). Moreover, in the case of walled, bacterial cells it is not possible to probe the range between 0.6 and 27 kDa (Fig. 1B, red square). Such bacteria cannot permeate molecules larger than 600 Da (which hampers staining the cells with fluorescent dyes or labeled dextrans) and so one is usually restricted to making gene fusions with GFP, a protein of 27 kDa.

We need alternative fluorophores!

The discovery of GFP has opened a lot of possibilities for cell biology. It allows selectively tagging and visualization of proteins inside living cells. In recent years, more fluorescent proteins have been discovered/engineered (e.g., the mFruit series (Shaner *et al.*, 2004) that cover a substantial part of the visible light spectrum. This now enables to visualize, distinguish and co-localize several proteins in one and the same cell/organelle at the same time. In the last couple of years photoswitchable proteins have been introduced (such as Dendra or mEos ((Huang *et al.*, 2009)). This development allows to influence the photophysical properties of fluorescent proteins (e.g. change their emission spectrum) after the proteins have been expressed. This phenomentnon can be used for tracking protein traffic inside living cells or to selectively visualize a (small) subset of the expressed protein, which is exploited in super-resolution microscopy techniques such as PALM (Betzig *et al.*, 2006).

Despite fantastic developments in the engineering of fluorescent proteins, we still need new, better and alternative fluorophores. The main problem with existing fluorescent proteins is their relatively low photostability and low brightness. Moreover, it is not uncommon to observe that tagging of a protein with GFP (or derivative) perturbs its sub -cellular localization. In a study where yeast vacuolar proteins were tagged with GFP (Wiederhold, 2010), 3 out of 11 tested proteins yielded different subcellular localizations, depending on whether the protein was tagged at the N- or C-terminus. Another example of a pitfall has been observed in the bacterial cytoskeletal proteins (FtsZ and MreB). C-terminal GFP fusions to these proteins are lethal for the cells. If there had been an alternative approach to selectively label cytoskeletal proteins, e.g. with small molecule fluorophores, it would have been more straight-forward to probe the cytoskeletal structure.

For the available fluorescent proteins there is still room for improvement of their brightness and photostability, as they are still worse than fluorescent dyes. Super-resolution techniques require photoswitchable proteins with a high on/off ratio. In our experience, the best photoswitchable fluorescent protein to date is mEos2. For super-resolution microscopy, e.g. PALM , we need more spectrally distinguishable photoswitchable proteins to enable multi-color PALM.

Crowding: quality and not only quantity!

The diffusion of molecules in the cytoplasm of living organism is slower than in water. Furthermore, diffusion in the cytoplasm of *E .coli* is slower than in the cytoplasm of eukaryotic cells. This is rationalized by the macromolecule crowding, which is lowest in dilute aqueous solutions and highest in the cytoplasm of bacterial cells (see chapter 2 and 4). When bacterial cells are exposed to increased osmolality, the cytoplasm loses water, crowding increases and diffusion slows down (Chapter 2,3, 4 and 5).

In chapter 3, we compared two FRAP techniques in order to understand whether the observed differences in diffusion coefficients for GFP have technical or biological basis. We conclude that for cells grown and handled in the same way, the two FRAP techniques (conventional FRAP and pulsed-FRAP) yield comparable data. This implies that growth conditions can contribute to differences in the properties of the cytoplasm that influence molecule mobility. Additionally, as discussed in detail in chapter 3, cells grown in minimal media have higher GFP diffusion coefficients than those grown in rich media. It is known that bacterial cells cultivated in rich media, grow faster and have higher amounts of ribosomes and mRNAs. Ribosomes are bigger proteins and thus bulkier crowders. mRNA molecules form long, largely disordered chains and are much less stiff than proteins and might hinder the motion of molecules in the cytoplasm more than proteins do.

All together this suggests that it is not only the concentration of crowders but also the quality of the crowders that matter for lateral diffusion and thus the traffic in the cell. Experiments should be carried out where the amounts of ribosmoes and mRNAs in the cytoplasm are varied systematically, and it should be tested how this impacts molecule mobility. In chapter 4, we have investigated the role of the nucleoid in forming barriers for mobility in the cytoplasm of *E. coli*. It has been observed previously (van den Bogaart *et al.*, 2007) that in severely osmotically stressed cells, the diffusion in the cytoplasm is not homogenous and it has been suggested that the nucleoid forms a barrier for diffusion. In chapter 4, we show that it is not only the nucleoid that forms barriers for mobility but also the increased crowding of the cytoplasm. To obtain a better understanding of the role of the nucleoid in obstructing macromolecule mobility, diffusion measurements should be carried out in cells devoid of chromosomal DNA. Hatano and colleagues (Hatano *et al.*, 2007) have created a strain (*E. coli* HT790, derived from MC1061) that produces anucleate cells at a high frequency (nearly 20%).

References

Betzig, E., G. H. Patterson, R. Sougrat, O. W. Lindwasser, S. Olenych, J. S. Bonifacino, M. W. Davidson, J. Lippincott-Schwartz & H. F. Hess, (2006) Imaging intracellular fluorescent proteins at nanometer resolution. *Science* **313**: 1642-1645.

Dix, J. A. & A. S. Verkman, (2008) Crowding effects on diffusion in solutions and cells. *Annu Rev Biophys* **37**: 247-263.

Hatano, T., Y. Yamaichi & H. Niki, (2007) Oscillating focus of SopA associated with filamentous structure guides partitioning of F plasmid. *Mol Microbiol* **64**: 1198-1213.

Huang, B., M. Bates & X. Zhuang, (2009) Super-resolution fluorescence microscopy. *Annu Rev Biochem* **78**: 993-1016.

Konopka, M. C., I. A. Shkel, S. Cayley, M. T. Record & J. C. Weisshaar, (2006) Crowding and confinement effects on protein diffusion *in vivo*. *J Bacteriol* **188**: 6115-6123.

Konopka, M. C., Sochacki, K. A., Bratton, B. P., Shkel, I. A., Record, M. T., Weisshaar, J. C., (2009) Cytoplasmic protein mobility in osmotically stressed Escherichia coli. *J Bacteriol* **191**: 231-237.

Kumar, M., M. S. Mommer & V. Sourjik, (2010) Mobility of cytoplasmic, membrane, and DNA-binding proteins in Escherichia coli. *Biophys J* **98**: 552-559.

McGuffee, S. R. & A. H. Elcock, (2010) Diffusion, crowding & protein stability in a dynamic molecular model of the bacterial cytoplasm. *PLoS Comput Biol* **6**: e1000694.

Nenninger, A., G. Mastroianni & C. W. Mullineaux, (2010) Size dependence of protein diffusion in the cytoplasm of Escherichia coli. *J Bacteriol* **192**: 4535-4540.

Shaner, N. C., R. E. Campbell, P. A. Steinbach, B. N. Giepmans, A. E. Palmer & R. Y. Tsien, (2004) Improved monomeric red, orange and yellow fluorescent proteins derived from Discosoma sp. red fluorescent protein. *Nat Biotechnol* **22**: 1567-1572.

van den Bogaart, G., N. Hermans, V. Krasnikov & B. Poolman, (2007) Protein mobility and diffusive barriers in Escherichia coli: consequences of osmotic stress. *Mol Microbiol* **64**: 858-871.

Wiederhold, E., (2010) Quantitative proteomics of Saccharomyces cerevisiae vacuoles and stress response in Lactococcus lactis. In. Groningen: Rijksuniversiteit Groningen, pp. 49-57.

SUMMARY

This thesis presents the results of research I carried out in the last four years. Most of the experiments described here have been carried out, using fluorescence-based techniques, especially fluorescence microscopy. The book is divided in two parts.

In chapters 2-6 (part one), I studied *Escherichia coli*, a model of a prokaryotic (bacterial) organism. The interior of a cell is full of different kinds of (macro)molecules, the crowding of which resembles a shopping mall just a few days before Christmas. The aim of the work was to understand how fast molecules move in such an environment. In chapter 2, I summarize the most recent findings about (macro)molecule diffusion in bacteria. Fluorescence Recovery After Photobleaching (FRAP) is a widely-used fluorescence microscopy-based technique that allows quantification of the speed of movement (diffusion) of molecules. In chapter 3, I compare and evaluate two FRAP methods for the measurement of diffusion of molecules in bacteria. In chapter 4, I present measurements on the mobility of small, medium and large molecules in the cytoplasm of *E. coli*. As a tool of manipulating the crowding of cells, I exposed them to osmotic shifts. When the salt content of the external environment increases, bacterial cells, just like plant cells that have not been watered for a long time, lose water. This results in an increased crowding and a slowing down of the molecule mobility inside cells. An important outcome of the experiments presented in chapter 4 is that crowding and osmotic stress have more impact on macromolecules than on metabolites. In fact, severe osmotic stress ‘freezes’ proteins as they essentially become immobile. In chapter 5, using a special flow chamber, I followed the fate of single *E.coli* cells as they experience osmotic stress. The response of the cells to increased salt concentration was instantaneous (see book cover), but over time the cells adapted to this conditions and their shape and mobility of macromolecules were no longer as perturbed as just after the osmotic upshift. Due to their small size, bacterial cells are difficult to study with light (fluorescence) microscopy. In Chapter 6, I have implemented a new and exciting technique called PALM to perform microscopy of bacteria at increased resolution. This approach allows distinguishing details of structures inside cells that are as small as 10 nm, which is a great improvement as compared to the 250 nm that is the diffraction limit of conventional light microscopy.

In chapters 7 and 8 (part two), we determined the mechanism of action of a new class of antimicrobial peptides, using fluorescence-based techniques and computational methods (molecular dynamics simulations). As bacteria are becoming resistant towards antibiotics, there is a need to find alternative substances that can kill them. Antimicrobial peptides are promising candidates. The main goal of research in this area is to find peptides that selectively kill bacterial cells, without harming the human (host) cells. To find such candidate drugs among antimicrobial peptides or to be able to design them, we need to understand their mechanism of action on the molecular level. In this part of the thesis we studied two new peptides: a cyclic one and its linear counterpart. What is especially intriguing about this pair is that despite having the same amino-acid sequence, only the cyclic peptide is biologically active and able to kill bacteria. The experiments presented in chapters 7 and 8 demonstrate that the cyclic peptide, unlike the linear analog, folds (acquires secondary structure) when it comes in contact with a membranes and subsequently is able to form pores that are mostly lethal for the bacterial cell.

SAMENVATTING

Dit proefschrift is een samenvatting van alle experimenten die ik de afgelopen vier jaar heb uitgevoerd. Het grootste deel van deze experimenten is gebaseerd op fluorescentie technieken, voornamelijk fluorescentie microscopie. In de hoofdstukken 2-6 (deel één van mijn proefschrift) richt ik mij op *Echerichia coli*, een veel gebruikt modelsysteem voor een bacteriële cel. Cellen zijn gevuld met allerlei verschillende macromoleculen die dusdanig dicht op elkaar gepakt zitten dat het vergelijkbaar is met de drukke mensenmassa in een winkelcentrum vlak voor de kerstdagen. Mijn doel was om uit te zoeken hoe snel moleculen in een cel kunnen bewegen onder deze omstandigheden. In hoofdstuk 2 geef ik een samenvatting van de recente literatuur over diffusie van (macro)-moleculen in bacteriën.

Fluorescence Recovery After Photobleaching (FRAP) is een veelgebruikte fluorescentie-microscopie methode waarmee de diffusiesnelheid van moleculen bepaald kan worden. In hoofdstuk 3 vergelijk en beoordeel ik twee FRAP methodes voor het meten van de diffusiesnelheid van moleculen in bacteriën.
In hoofdstuk 4 beschrijf ik de mobiliteit van grote, middelgrote en kleine moleculen in het celplasma van *E. coli* onder verschillende omstandigheden. Door de cellen bloot te stellen aan een osmotische verhoging van het milieu was het mogelijk de opeenpakking van moleculen in het celplasma te vergroten. Wanneer bijvoorbeeld de zoutconcentratie in het externe milieu toeneemt, zullen de cellen water verliezen (net als planten die te lang geen water hebben gekregen). Het gevolg hiervan is dat de moleculen in het cytoplasma dichter opeengepakt worden wat resulteert in een afname van hun diffusiesnelheid. Een belangrijke waarneming die ik beschrijf in hoofdstuk 4 is dat de opeenpakking van macromoleculen in het celplasma een veel groter effect heeft op de diffusie van grote moleculen (eiwitten) dan op kleine moleculen (voedingsstoffen).

In hoofdstuk 5 gebruik ik een speciale flow-chamber, waardoor ik individuele *E. coli* cellen kon volgen terwijl ze een osmotische verandering ondergaan.

De cellen reageerden onmiddellijk op de verhoging van de zoutconcentratie (zie de voorkant van dit proefschrift), maar na verloop van tijd wisten ze zich aan te passen aan deze omstandigheden en waren er geen effecten meer waar te nemen op de vorm van de cellen en de diffusiesnelheid van macromoleculen in het celplasma.

Vanwege hun beperkte grootte is het erg moeilijk om bacteriële cellen te bestuderen met conventionele licht (en fluorescentie)-microscopie. In hoofdstuk 6 pas ik een opwindende nieuwe methode toe die PALM wordt genoemd, waarmee ik bacteriële cellen met verhoogde resolutie heb kunnen waarnemen. Op deze manier is het mogelijk om details in de interne celstructuur te onderscheiden met een grootte van slechts 10 nm. Dit is een enorme verbetering ten opzichte van conventionele licht microscopie waar de limiet voor het onderscheiden van moleculen ligt bij ongeveer 250 nm.

In de hoofstukken 7 en 8 (deel twee van dit proefschrift) heb ik het mechanisme van een nieuw klasse porie-vormende peptiden met antibacteriële activiteit bestudeerd met fluorescentie technieken en computersimulaties. Antibiotica-resistente bacteriën worden een steeds groter probleem en daarom is er grote behoefte aan alternatieve antibacteriële stoffen. Antibacteriële peptiden zijn hiervoor een veelbelovende klasse van moleculen. Het is belangrijk om peptiden te vinden die selectief bacteriën doden en niet schadelijk zijn voor menselijke (gastheer)cellen. Om de juiste peptiden te vinden -of te ontwerpen- hebben we kennis nodig over het mechanisme van hun antibacteriële activiteit op moleculair niveau. In dit deel van mijn proefschrift hebben we twee nieuwe peptiden bestudeerd: een cyclisch peptide en zijn lineaire tegenhanger. Fascinerend aan dit peptide-paar is dat, hoewel ze een identieke aminozuurvolgorde hebben, alleen het cyclische peptide biologisch actief is (in staat om bacteriën te doden). Met de experimenten die beschreven staan in de hoofdstukken 7 en 8 heb ik aangetoond dat het cyclische peptide in staat is te vouwen (secundaire structuur aan te nemen) en dieper te inserteren in de lipidenbilaag. Hierdoor kan het cyclische peptide een porie in het celmembraan vormen wat mijns inziens de oorzaak is voor het doden van de (bacteriële) cellen.

STRESZCZENIE

Książka ta zawiera wyniki badań, które prowadziłem w ciągu ostatnich czterech lat. Większość przedstawionych tu eksperymentów oparta jest o techniki fluorescencyjne, a w szczególności mikroskopię fluorescencyjną. Książka ta jest podzielona na dwie części.

W rodziałach 2-4 (część pierwsza) używałem *Escherichia coli* jako modelu komórki prokarjotycznej (bakteryjnej). Wnętrze komórki jest wypełnione wszelkiego rodzaju (makro) cząsteczkami, które są tak gęsto upakowane jak galeria handlowa tuż przed świętami Bożego Narodzenia. Celem tej pracy było zrozumiene jak szybko cząsteczki są w stanie poruszać się w takim środowisku.W rodziale 2 podsumowuję najnowsze odkrycia dotyczące dyfuzji (makro) cząsteczek w bakteriach. FRAP (z ang. „Fluorescence Recovery After Photobleaching”) to szeroko stosowana metoda umożliwiająca pomiar prędkości z jaką poruszają się cząsteczki (dyfuzji). W rozdziale 3 porównuję i oceniam dwie odmiany metody FRAP pod względem ich przydatności do pomiaru dyfuzji (cząsteczek) w bakteriach. W rodziale 4 przedstawiam pomiary ruchliwości małych, średnich i dużych cząsteczek w cytoplaźmie *E.coli.* Stres osmotyczny jest tutaj narzędziem służącym do zmiany gęstości upakownia cytoplazmy. Kiedy stężenie soli w środowisku zewnętrznym nagle wzrasta komórki bakteryjne, podobnie jak długo niepodlewane rośliny, tracą wodę. Konsekwencją tej utraty jest wzrost zagęszczenia cytoplazmy i spadek prędkości z jaką poruszają się cząsteczki. Ważnym wynikiem badań zebranych w rozdziale 4 jest to, że stres osmotyczny ma większy wpływ na ruchliwość dużych cząsteczek (makromolekuł), niż małych cząsteczek (np.: metabolitów). W najbardziej skrajnych warunkach duże cząsteczki „zastygają w miejscu”, gdyż ich ruchliwość drastycznie spada. W rodziale 5 za pomocą specjalnej komory przepływowej śledziłem los pojedyńczych komórek *E.coli* podczas ekspozycji na działanie stresu osmotycznego. Reakcja komórek na zwiększoną zawartość soli w środowisku zewnętrznym jest natychmiastowa. Jednak z czasem komórki przystosowują się do nowych warunków i ich kształt, a także ruchliwość makromolekuł, powracają do normy.

Ponieważ bakterie są małych rozmiarów, trudno je badać za pomocą mikroskopii świetlnej (fluorescencyjnej). W rodziale 6 zastosowałem nową i obiecującą technikę zwaną PALM (z ang. „Photo-Activated Localization Microscopy”) aby móc zajrzeć do komórek bakteryjnych ze zwiększoną rodzielczością. Za pomocą tej techniki można oglądać wnętrze omawianych komórek, a w nich szczegóły rzędu 10 nm, co stanowi znaczną poprawę w porównaniu do konwencjonalnej mikroskopii będącej w stanie odróżnić obiekty położone dopiero 250 nm od siebie.

W rozdziałach 7 i 8 (część druga) zbadałem mechanizm działania nowej klasy peptydów anymikrobowych, za pomocą technik opratych o fluorescencję i symulacji komputerowych. Ponieważ bakterie uzyskują odporność na coraz to nowe antybiotyki, potrzebne są alternatywne substancje będące w stanie je zabić. Peptydy antymikrobowe są tutaj potencjalnymi kandydatami. Główny wysiłek naukowców w tej dziedzinie zorientowany jest na znalezienie takich peptydów, które byłyby w stanie selektywnie zabijać komórki bakteryjne, nie szkodząc przy tym komórkom ludzkim (bądź innego gospodarza). Aby znaleźć odpowiednie cząsteczki pośród istniejących peptydów bądź zaprojektować nowe, takie które spełniają powyższe kryterium, trzeba zrozumieć ich mechanizm działania na poziomie molekularnym. W tej części mojej pracy badałem dwa nowe peptydy: cykliczny i liniowy. Mają one tą szczególną właściwość, że pomimo identycznej sekwencji aminokwasowej, tylko cykliczny wariant jest aktywny biologicznie i zdolny zabijać komórki bakteryjne. Eksperymenty zebrane w rodziałach 7 i 8 dowodzą, że w przeciwieństwie do liniowego peptydu, analog cykliczny, kiedy styka się z błoną biologiczną jest w stanie ulec fałdowaniu (uzyskuje strukturę drugorzędową), a następnie utworzyć por w błonie, co prowadzi do śmierci komórki bakteryjnej.

ACKNOWLEDGEMENTS

If you are reading this thesis there is a very high chance that you helped me out at some point in the research projects presented here and for that I want to thank you. In the time I have spent in the Membrane Enzymology group/Nijenborgh 4/Zernike Institute/RUG I have met a lot of friendly and capable people. Thank you for always having the time and being helpful!

There are four people in particular to whom I would like to show special gratitude.

Bert, you have been my direct supervisor and an excellent boss. You have given me a lot of freedom and so the time spent in your group was a fascinating intellectual adventure. You took me on a great tour starting from biological membranes, through peptide-lipid interactions, bacterial cells, osmotic stress, diffusion and ending up in the world of microscopy. I especially appreciate the help and effort you have made in correcting my manuscripts and quickly giving me my corrections. You almost made me like writing. I am grateful that you always valued my opinion even if we didn't agree (which is probably every second time we discussed anything).

Victor, my project couldn't have succeeded without you. Thank you for building all the microscopes I worked on, teaching me a lot about them and solving the microscope related problems. I enjoyed working with you. Thank you for always having the time to help me and discuss things over, for your relaxed approach and for a realistic, down-to-earth view on science.

Gemma and Paul. I was very lucky to supervise such capable and independent students as the two of you. The dedication and enthusiasm you showed during your projects was very motivating and it was a pleasure to work with you.

Groningen, 29 November 2011,

Jacek